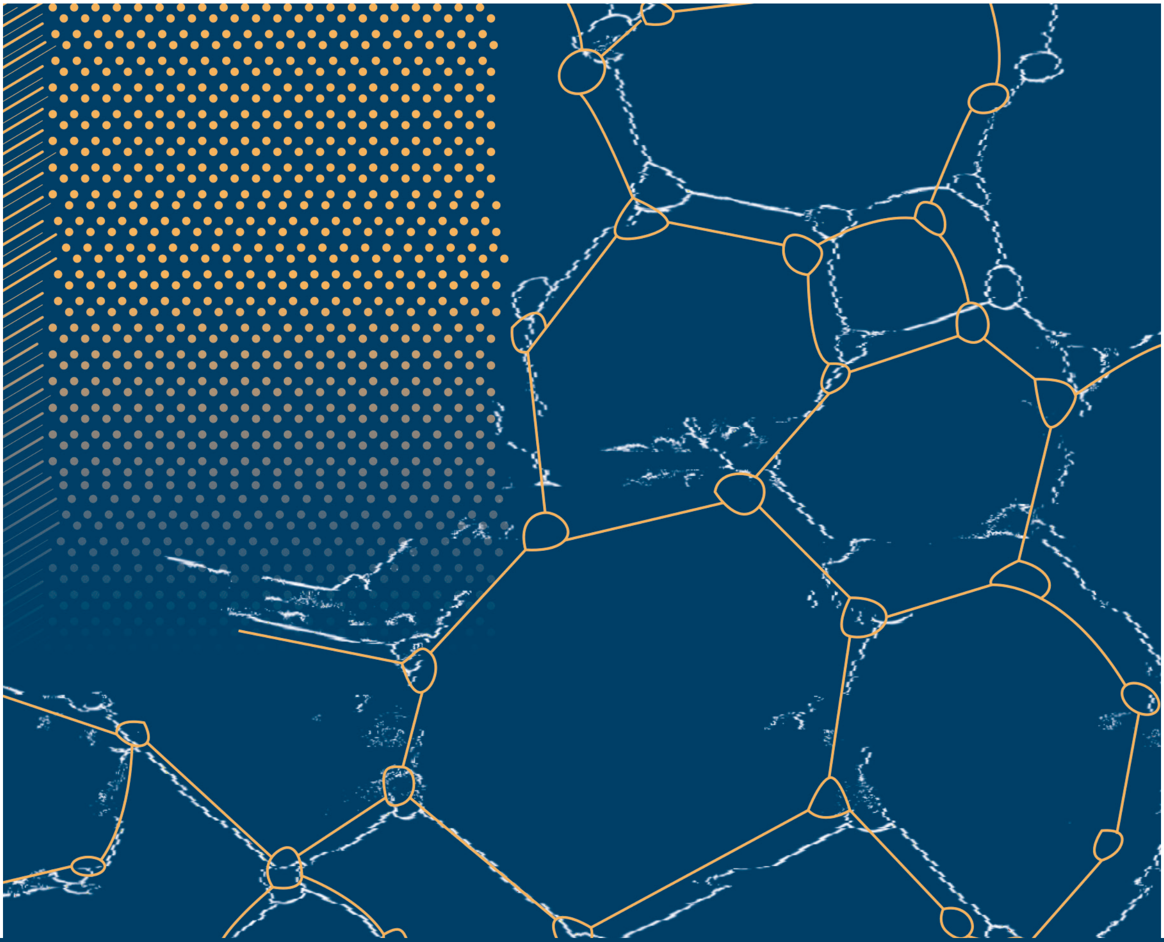

Field assisted sintering of yttria ceramics for plasma etching applications

Moritz Kindelmann

Energie & Umwelt / Energy & Environment
Band / Volume 553
ISBN 978-3-95806-579-6

Mitglied der Helmholtz-Gemeinschaft

JÜLICH
Forschungszentrum

Schriften des Forschungszentrums Jülich
Reihe Energie & Umwelt / Energy & Environment Band / Volume 553

Forschungszentrum Jülich GmbH
Institut für Energie- und Klimaforschung
Werkstoffsynthese und Herstellungsverfahren (IEK-1)

Field assisted sintering of yttria ceramics for plasma etching applications

Moritz Kindelmann

Schriften des Forschungszentrums Jülich
Reihe Energie & Umwelt / Energy & Environment Band / Volume 553

ISSN 1866-1793 ISBN 978-3-95806-579-6

Bibliografische Information der Deutschen Nationalbibliothek.
Die Deutsche Nationalbibliothek verzeichnet diese Publikation in der
Deutschen Nationalbibliografie; detaillierte Bibliografische Daten
sind im Internet über http://dnb.d-nb.de abrufbar.

Herausgeber und Vertrieb: Forschungszentrum Jülich GmbH
Zentralbibliothek, Verlag
52425 Jülich
Tel.: +49 2461 61-5368
Fax: +49 2461 61-6103
zb-publikation@fz-juelich.de
www.fz-juelich.de/zb

Umschlaggestaltung: Grafische Medien, Forschungszentrum Jülich GmbH

Druck: Grafische Medien, Forschungszentrum Jülich GmbH

Schriften des Forschungszentrums Jülich
Reihe Energie & Umwelt / Energy & Environment, Band / Volume 553

D 82 (Diss. RWTH Aachen University, 2021)

ISSN 1866-1793
ISBN 978-3-95806-579-6

Abstract

Advanced ceramics materials like yttrium oxide (Y_2O_3) are of high interest for critical manufacturing processes in the semiconductor industry due to their high chemical stability in contact with fluorine based etching plasmas. However, until now Y_2O_3 gets primarily applied as a functional coating deposited by thermal spray or aerosol deposition technique due to complications associated with the manufacturing of bulk ceramic components. Yttria exhibits a low sinterability when conventionally processed and fabricating large scale samples with high performance concerning chemical purity and relative density is a challenging task. Complex processing routes using conventional or vacuum sintering and an additional post-compaction step by hot isostatic pressing are necessary to achieve relative densities which are matching the requirements of the semiconductor industry. These major drawbacks have prevented the application of bulk Y_2O_3 components in state of the art semiconductor manufacturing devices.Therefore, in this work, field assisted sintering technique / spark plasma sintering (FAST/SPS) is investigated as a straightforward processing technique which enables to consolidate high performance, dense ceramic components in a single processing step.

In two separate parts, applied and fundamental research questions are going to be addressed. The first part of this work focuses on evaluating the direct processability of commercial powders, solving challenges during the upscaling of sample sizes, processing of complex shaped components as well as characterizing the impact of rare earth doping on sintering and grain growth. Upscaling of ceramic samples is generally hindered by the formation of thermal inhomogeneities in the tool setup. Therefore the application of carbon fibre reinforced carbon spacers and their optimal position in the FAST/SPS tool was investigated by coupling experiments and simulations. Furthermore, graphite powder bed assisted FAST/SPS was applied to study the possibilities of sintering multiple complex shaped Y_2O_3 samples in one step. Lastly, the influence of rare earth doping with La^{3+} and Gd^{3+} on sintering and grain growth of Y_2O_3 during FAST/SPS processing was studied thoroughly. The segregation of La^{3+} decelerated both sintering and grain boundary kinetics through a solute drag effect, effectively preventing pore detachment at high sintering temperatures and leading to enhanced densification in the final stage of sintering.

In the second part of the work, the plasma-material interaction of Y_2O_3 ceramics was extensively studied to identify critical sample defects, plasma parameters and intrinsic properties which control the material erosion. In general, erosion of oxide ceramic materials like Y_2O_3 occurs by a physicochemical mechanism controlled by the reactive fluorine species (CF_4) and the ionized plasma species (Ar). The main plasma processing parameters (CF_4/Ar ratio; bias voltage) were varied to develop a schematic operation map which contains the different erosion regimes. To understand the fundamental mechanism which controls the physicochemical erosion, a straightforward re-localization technique was developed to investigate the microstructural features and properties before the exposure and correlate their

impact on the degree of erosion and resulting surface morphology. Hereby, a grain orientation dependent erosion mechanism could be described for the first time which controls the surface fluorination as well as physical removal creating a plateau-like topography.

The combined study of sintering and plasma-material interaction conducted in this work is a solid basis for future applications of Y_2O_3 ceramic components in next generation of plasma etching devices and provides new insights regarding the active erosion mechanisms of oxide ceramics in reactive plasmas.

Zusammenfassung

Hochleistungskeramiken wie Yttriumoxid (Y_2O_3) sind aufgrund ihrer hohen chemischen Stabilität im Kontakt mit fluorbasierten Ätzplasmen von großem Interesse für kritische Fertigungsprozesse in der Halbleiterindustrie. Bislang wird Y_2O_3 jedoch hauptsächlich als funktionelle Beschichtung eingesetzt. Denn Y_2O_3 weist bei konventioneller Verarbeitung eine niedrige Sinterfähigkeit auf, sodass die Herstellung von dreidimensionalen, voll-keramischen Bauteilen mit einer komplexen Prozessierung verbunden ist. Um Komponenten von hoher Qualität hinsichtlich chemischer Reinheit und relativer Dichte im industriellen Maßstab herzustellen, ist neben konventionellem Sintern bei hohen Temperaturen eine zusätzliche Verdichtung durch heiß isostatisches Pressen nötig. In dieser Arbeit wird das feldunterstützte Sintern / Spark Plasma Sintering (FAST/SPS) von Y_2O_3 untersucht, welches in der Lage ist, hochwertige, dichte keramische Bauteile in einem einzigen Prozessschritt zu verarbeiten.

In einem ersten Teil der Arbeit, welche in zwei thematische Teile aufgeteilt ist, werden verschiedene anwendungsorientierte und grundlegende Fragestellungen hinsichtlich des Sinterprozesses behandelt. Hier wird im Detail untersucht, wie sich kommerzielle Pulver verarbeiten lassen, welche Herausforderungen das Upscaling von Probengrößen birgt, wie sich komplex geformte Bauteile prozessieren lassen, und welchen Einfluss eine Dotierung mit seltenen Erden auf den Sinterprozess und das Kornwachstum haben. Während der Skalierung der FAST/SPS Technologie für keramische Werkstoffe bilden sich häufig thermische Gradienten im Werkzeugaufbau, welche die Prozessierung erschweren. Hierzu wurden sowohl Experimente als auch Simulationen durchgeführt, um zu untersuchen, inwieweit kohlenstofffaserverstärkte Graphit-Abstandshalter diesem Problem entgegenwirken können. Um die Möglichkeiten zu erproben, mehrere komplex geformte Y_2O_3-Proben simultan in einem Schritt zu sintern, wurde FAST/SPS mit Unterstützung eines Graphitpulverbettes angewendet. Schließlich wurde der Einfluss der Dotierung mit seltenen Erden (La^{3+} und Gd^{3+}) auf die Verdichtung und das Kornwachstum von Y_2O_3 während des FAST/SPS-Sinterns untersucht. Die Segregation von La^{3+} an den Korngrenzen verlangsamte sowohl die Sinter- als auch die Korngrenzkinetik durch einen "Solute Drag" Effekt. Hierdurch wurde die Ablösung der Poren von der Korngrenze bei hohen Sintertemperaturen verhindert und so eine verbesserte Verdichtung in der Endphase des Sinterns erreicht.

In einem zweiten Teil wird die Plasma-Material-Wechselwirkung von Y_2O_3-Keramiken eingehend untersucht, um kritische Probendefekte, Plasmaparameter und intrinsische Eigenschaften zu identifizieren, die die Materialerosion kontrollieren. Oxidkeramische Materialien wie Y_2O_3 werden durch einen physikochemischen Mechanismus erodiert, welcher durch die Wechselwirkungen mit der reaktiven Fluorspezies (z.B. CF_4) und der ionisierten Plasmaspezies (Ar) dominiert wird. Die wichtigsten Plasmaprozessparameter (CF_4/Ar-Verhältnis; Bias-Spannung) wurden variiert, um eine schematische Prozesskarte zu entwickeln, die die verschiedenen Erosionsbereiche beschreibt. Um den grundlegenden Mechanismus zu klären, der die physikalisch-chemische Ero-

sion steuert, wurde eine Re-Lokalisierungstechnik entwickelt, die es ermöglicht, die mikrostrukturellen Eigenschaften vor der Erosion zu untersuchen und deren Einfluss auf die Ausprägung der Abtragung und die sich bildende Oberflächentopographie zu korrelieren. Hierdurch konnte erstmals ein von der Kornorientierung abhängiger Erosionsmechanismus beschrieben werden, der sowohl von der Oberflächenfluorierung als auch durch den physikalischen Abtrag kontrolliert wird und eine plateauartige Topographie erzeugt.

Die Untersuchungen zum FAST/SPS Sintern und zur Plasma-Material-Wechselwirkung von Y_2O_3, welche im Rahmen dieser Studie durchgeführt wurden, tragen dazu bei, den Grundstein für zukünftige Anwendungen von Y_2O_3-Komponenten in Halbleiteranwendungen zu legen und liefern einen tiefergehenden Einblick in die Erosionsmechanismen, welche zur Degradation von Oxidkeramiken in reaktiven Plasmen führen.

Contents

Abbreviations III

Variables V

1 Motivation and scientific objectives 1

2 Introduction and theoretical background 5
- 2.1 Y_2O_3 – Material properties and applications 5
- 2.2 Fundamentals of Sintering 7
  - 2.2.1 Driving force and stages of sintering 7
  - 2.2.2 Mechanisms controlling sintering 9
  - 2.2.3 Pressure assisted sintering 12
- 2.3 Grain growth and microstructure control 13
  - 2.3.1 Fundamentals of grain growth 14
  - 2.3.2 Mechanisms controlling grain boundary migration 17
  - 2.3.3 Microstructure control through doping of Y_2O_3 21
- 2.4 Field assisted sintering technology/spark plasma sintering (FAST/SPS) 23
  - 2.4.1 Fundamentals and working principle 24
  - 2.4.2 Mechanisms of densification 25
  - 2.4.3 Field assisted sintering of Y_2O_3 26
- 2.5 Plasma etching for semiconductor applications 28
  - 2.5.1 Fundamentals of reactive plasma etching 28
  - 2.5.2 Plasma erosion of polycrystalline ceramics 30

3 Experimental procedure and methodology 33
- 3.1 Powder characterization 33
- 3.2 Starting materials and powder processing 35
- 3.3 Sintering experiments 36
- 3.4 Plasma material interaction experiments 41
- 3.5 Microstructure and surface characterization techniques 44

4 FAST/SPS of Y_2O_3 51
- 4.1 Conventional sintering of Y_2O_3 51
  - 4.1.1 Powder characterization and material selection 51
  - 4.1.2 Influence of powder processing on conventional sintering . . . 54
- 4.2 FAST/SPS of commercial Y_2O_3 powders 58
  - 4.2.1 Control of microstructure evolution using commercial powders 58
  - 4.2.2 Characteristics and challenges of sample scale up 62
- 4.3 FAST/SPS of rare earth doped Y_2O_3 70
  - 4.3.1 Densification and grain growth behaviour 70
  - 4.3.2 Grain boundary structure and chemistry 74

4.3.3 Impact of segregation on sintering and grain growth 78

5 Erosion Behaviour of Y_2O_3 in reactive plasma environments 83
5.1 Influence of processing induced surface defects 83
5.2 Influence of plasma processing parameters 88
5.2.1 Influence of applied bias voltage 88
5.2.2 Influence of plasma composition 94
5.3 Influence of microstructure and crystalline orientation 99
5.3.1 Behaviour of pure Y_2O_3 99
5.3.2 Comparison of Y_2O_3 and YOF 105

6 Scientific and industrial implications and impact 113

7 Conclusions and Outlook 117

Acknowledgements 121

List of Figures V

List of Tables XIV

Literature XXX

Abbreviations

FAST/SPS	Field assisted sintering technique / spark plasma sintering
PB-SPS	Powder bed assisted spark plasma sintering
HP	Hot pressing
HIP	Hot isostatic pressing
AD	Aerosol deposition
APS	Atmospheric plasma spraying
OPS	Oxide polishing suspension
IBAD	Ion beam assisted deposition
ICP	Inductively coupled plasma
SEM	Scanning electron microscopy
BSE	Backscattered electron
SE	Secondary electron
EDS	Energy dispersive X-ray spectroscopy
EBSD	Electron backscatter diffraction
IPF	Inverse pole figure
FIB	Focused ion beam
TEM	Transmission electron microscopy
STEM	Scanning transmission electron microscopy
HRTEM	High resolution transmission electron microscopy
HAADF	High-angle annular dark field imaging
AFM	Atomic force microscopy
TOF-SIMS	Time of flight - secondary ion mass spectroscopy
XPS	X-ray photoelectron spectroscopy
PSD	Particle size distribution
SSA	Specific surface area
ICP-MS	Inductively coupled plasma - mass spectroscopy
XRD	X-ray diffraction
YAG	Yttrium aluminium garnet
CFC	Carbon fibre reinforced carbon

Variables

Sintering

A	Interfacial area
γ_{gb}	Grain boundary energy
γ_{sv}	Surface energy
ΔE	Difference in free energy
Ψ	Dihedral angle
p_e	Effective stress
p_a	Applied stress
Φ	Stress identification factor
K_p	Curvature of a pore
P	Amount of porosity
H	Constant in hot pressing equation
D	Diffusion coefficient
n	Pressure exponent
m	Grain size exponent
k	Boltzmann constant
T	Absolute temperature
G	Average grain size
δ	relative density

Grain growth

K	Constant for grain growth
v_b	Grain boundary velocity
M_b	Grain boundary mobility
F_b	Driving force acting on the grain boundary
α	Geometrical constant for grain shape
Ω	Atomic volume
δ_{gb}	Grain boundary width
f	Volume fraction of secondary inclusions
RF_d^{max}	Retarding force in Zener pinning
λ	Solute drag parameter
β	Solute drag parameter
C_∞	Concentration of dopant in the bulk
N_V	Number of host atoms per unit volume
Q	Degree of segregation
U	Interaction force dopant with grain boundary

Experimental procedure

θ	Scattering angle
D	Particle size
λ	Wave length
d	Lattice spacing
n	Order of diffraction

1 Motivation and scientific objectives

Since the development of the first integrated circuits in the late 1950ies and the following prediction of Moore's Law, which defined that the number of transistors on a microchip could double every two years, the semiconductor industry is striving to fulfil their ambitious roadmap (Fig. 1.1) [1]. Over 50 years of process and material development in the microelectronic manufacturing industry lead to the decrease of feature sizes below what was imaginable decades ago. The node width of a single logic element on a microchip is now below 7 nm and a further decrease is projected but the boundaries of the physically possible are inevitable [2, 3].

This continuous miniaturization is enabled by increasingly complex manufacturing methods which include three key steps: imaging, etching and deposition. As the size of all functional elements decreases, the requirements for purity and process stability in semiconductor manufacturing equipment are constantly rising. A further development according to the IEEE Roadmap white paper includes various novel strategies ranging from 3D integrated structures to a continued reduction of geometries and new material combinations [4]. Especially the diversification of the manufacturing route which combines logical structures at the edge of the physical possibilities and three dimensional architectures will lead to challenging increases in etching time, chemical abrasiveness and applied ion energy. These strategies will pose a massive challenge for process control and reliability of the processing equipment. Especially the advances of modern etching plasmas cause high requirements concerning the stability, purity and physical quality of components which are in direct contact to the abrasive interior.

For most of the critical processing steps during plasma etching the state of the art material is high purity, synthetic quartz glass. Thanks to decades of research and

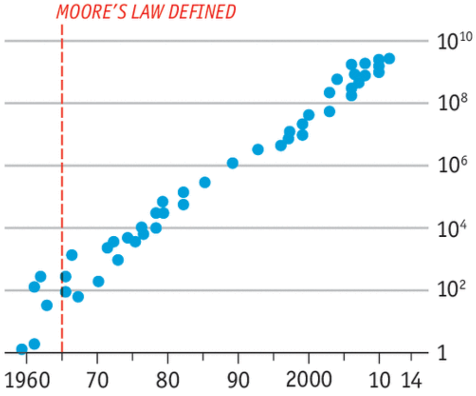

Fig. 1.1 Historical development of the number of transistors on a microchip which is in general referred to as Moore's law. Graph adapted from [5].

development, the purification and manufacturing technologies applied in the glass industry enable to produce components with residual impurities in the range of parts per billion (ppb). However, the major advantage that silica based components inherit is also one of its biggest drawbacks: In contact with etching plasmas SiO_2 components are chemically degrading via a reaction that is forming a volatile product (Eq. 1.1) [6].

$$SiO_2 + CF_4 \longrightarrow SiF_4 + CO_2 \tag{1.1}$$

The formation of tetrafluorsilan (SiF_4) during the chemical erosion of silica is of great advantage because it allows to remove the gaseous side products directly from the processing environment, and therefore reducing impurities and particle formation to an absolute minimum [7]. However, the formation of gaseous phases leads to a fast erosion of quartz glass components inside the processing chamber inducing inefficient manufacturing down times and can even limit the process window for critical parameters, preventing the application of new 3D architecture strategies.

Therefore, novel etch resistant components have to be developed to broaden the applicable process window during plasma etching. Among diverse advanced ceramic materials, which can be used in semiconductor industry, yttrium oxide (Y_2O_3) is one of the thermodynamically most stable materials in contact with fluorine based reactive plasmas and therefore one of the most promising material candidates for the next generation of plasma resistant components. Due to the formation of highly stable yttrium fluorides and yttrium oxyfluorides during the exposure to fluorine based plasmas, yttria exhibits etching rates which are orders of magnitude smaller compared to silica glass [8, 9]. However, only a basic understanding of the erosion behaviour of polycrystalline Y_2O_3 has been developed and major influencing factors have not been considered under different processing conditions. The general mechanism is assumed to be controlled by the deposition of fluorocarbons from the plasma gas which chemically interact with the surface forming a fluorine gradient [10, 11]. The degraded surface layer is prone to removal by Ar ion bombardment leading to a continuous erosion process [12].

Although the suggested mechanisms gives a good insight into the main driving forces which lead to chemical degradation and drive material removal, major influencing factors have not been addressed: (I) The influence of different processing conditions on the morphological damage and the chemical interaction at the surface. (II) The influence of microstructural features and properties like grain boundaries and grain orientations on the erosion mechanism (III) A comparison between the erosion mechanisms of pure oxides and oxyfluorides, which are predicted to have an increased chemical resistance [13, 14, 15, 16].

In addition to the lack of complete understanding of the erosion mechanisms, the application of bulk components made from yttria is still not marketable due to the low sinterability of Y_2O_3 leading to complex and cost intensive processing routes. In general, conventional sintering of yttria requires high sintering temperatures and long cycle times to achieve high relative densities. However, for achieving material qualities which can be applied in semiconductor manufacturing devices additional densifying steps like hot isostatic pressing have to be utilized [17]. These inefficient and expensive manufacturing routes prevent an industrial application of bulk Y_2O_3

components in the semiconductor industry so far.
Therefore, the application of field and pressure assisted sintering techniques could solve this problem and allow to establish bulk yttria components in the semiconductor industry. The field assisted sintering technique / spark plasma sintering (FAST/SPS) is a promising densification method that uses pulsed electric current and mechanical pressure to enhance the densification and therefore allows a decrease of total cycle time and maximum sintering temperature. This novel approach enables the rapid and single step densification of various material systems which are difficult to sinter including oxide ceramics, ultra high temperature carbides and borides as well as refractory metals [18]. The consolidation of Y_2O_3 powders producing lab-scale samples by FAST/SPS has been described in literature using varying sintering temperatures, applied pressures, heating rates and dwell times, always achieving high relative densities [19, 20, 21].
With respect to this brief introduction, the main objectives and research questions of this study are described as follows:

- How can FAST/SPS be applied to process commercial powders in a one step sintering process and which challenges can emerge when this technique is upscaled?
- Are there other processing and material optimization possibilities to control sintering and grain size development as well as final relative density which are applicable under the restrictive boundary conditions of the semiconductor industry?
- Do the processing conditions have a major influence on the morphological changes during the plasma exposure of yttria and what are the major processing parameters controlling the degree of the plasma attack?
- How do microstructural features and properties influence the erosion mechanism of polycrystalline yttria?
- Can the surface degradation through chemical fluorination be prevented by the application of fluorine containing compounds?

In sum, the major goal of this thesis is to gain a broad understanding of the field assisted sintering of yttria at different length scales as well as to increase the understanding of the erosion behaviour of yttria in fluorine based plasmas. This thesis focuses both on applied and fundamental questions gathered around yttrium oxide as a plasma resistant ceramic.

2 Introduction and theoretical background

In this chapter a compact overview of the fundamentals and the current state of knowledge concerning the investigated topics of this work will be given. The chapter introduces the investigated material Y_2O_3, its properties and applications as well as the fundamentals of solid state sintering and grain growth. Furthermore, a conclusive summary of the influence of doping on the sintering and grain coarsening behaviour of Y_2O_3 ceramics is given. Then, the technological aspects are discussed by introducing FAST/SPS and its working principle, mechanisms of densification and application to consolidate yttria ceramics. Finally, an overview on the plasma etching process is given and the application of polycrystalline Y_2O_3 in reactive plasmas and its specific erosion behaviour are discussed.

2.1 Y_2O_3 – Material properties and applications

Yttrium oxide (Y_2O_3) is a rare earth oxide ceramic with various technological applications due to its promising chemical, thermal and optical properties. Yttria crystallizes in a C-type cubic structure (bixbyite) with a lattice constant a = 1,0604 nm and the unit cell is composed of 80 atoms [22]. A three dimensional sketch of the crystal structure is given in Fig. 2.1, where oxygen anions are represented as red and yttrium cations as grey spheres. In the bixbyite structure the oxygen atoms are located at (48e) sites and yttrium atoms are unequally distributed at (8b) and (24d) sites resulting in a specific oxygen vacancy arrangement in the structure.
Furthermore, Y_2O_3 shows a good solubility for different alio- and isovalent cations of different sizes [23]. This makes it attractive for fundamental studies concerning

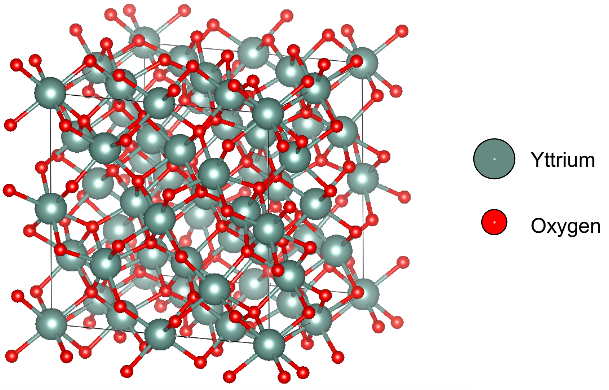

Fig. 2.1 Crystal structure of Y_2O_3.

sintering and grain growth as well as studies which use doping to functionalize the materials e.g. for laser or scintillator applications.

Pure Y_2O_3 has a high melting point (2410 °C) [24] and shows a good thermal conductivity of around 27 - 33 W/(m·K) at room temperature compared to other oxide ceramics [25]. Additionally it exhibits a intermediate thermal expansion coefficient of 6,5 - 9,3 $\cdot 10^{-6}$ 1/K over a broad range of temperatures [26].

Concerning optical properties, Y_2O_3 exhibits a broad spectral region of transparency ranging from 230 nm to 8 μm [27, 28], which makes it a very promising candidate for transparent ceramics.

However, the most important properties of pure yttria are its high resistance against chemical corrosion, erosion and its inertness against reaction with molten metals. This makes Y_2O_3 a highly promising material for different applications under extreme conditions concerning the thermal and chemical environment.

There is a broad application spectrum for yttria ceramics which includes crucibles and nozzles for the handling of molten metals or the production of metal powders [29, 30, 31]. The promising optical properties yielded a broad variety of applications for transparent yttria in the industrial and military sector. Hereby, especially the combination of transparency and high temperature resistance is exploited in windows of discharge lamps, high temperature lenses and heat resistant windows [32, 33, 34]. An additional major sector with increasing a number of applications of Y_2O_3 components and coatings is the field of semiconductor processing. Y_2O_3 gets mainly applied as a highly erosion resistant material in various reactive plasma etching environments. This makes Y_2O_3 one of the most promising materials for consumable components and functional coatings for plasma etching applications [8, 11, 35]. Fig. 2.2 summarizes the major application fields of Y_2O_3 ceramics.

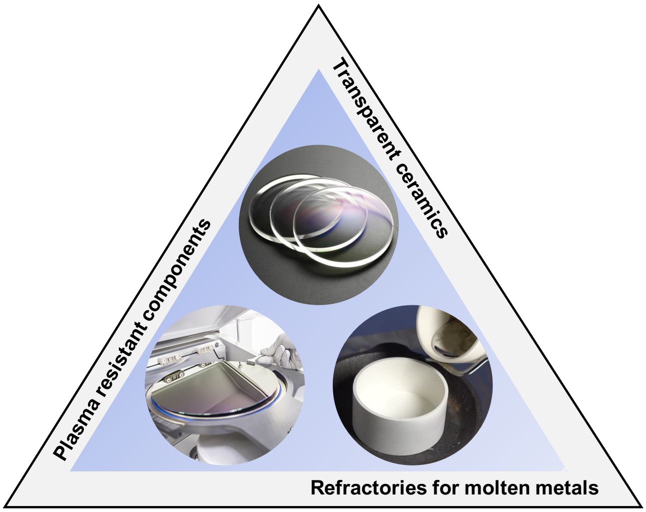

Fig. 2.2 Major applications of Y_2O_3 ceramics.

2.2 Fundamentals of Sintering

In the following two sections, the fundamentals of sintering and grain growth will be introduced and subsequently deepened by summarizing and discussing the major literature sources for controlled sintering of Y_2O_3 ceramics. The subchapters dealing with the fundamental relationships governing sintering and grain growth refer to the extensive textbooks by M. Rahaman and S.-J. Kang and follow their approach to introduce both fields [36, 37].
The basic relationships which are controlling the densification process will be introduced. Therefore, the driving forces for densification and the controlling mechanisms are presented. Additionally, pressure assisted sintering will be introduced as it is crucial to understand the change of driving forces influencing the processing parameters in case of sintering processes like hot pressing (HP) and FAST/SPS.

2.2.1 Driving force and stages of sintering

Sintering, which is sometimes also called firing, describes the fabrication step transforming a shaped powder compact into a consolidated solid body using a thermal treatment. The sintering process leads to a considerable amount of shrinkage and yields the desired material properties through pore removal and microstructure control. In general there are two types of sintering: (I) Solid state and (II) Liquid phase sintering. During solid state sintering the processing temperature never exceeds the liquidus temperature of any involved component and merely diffusion processes at high temperatures lead to densification. In contrast, liquid phase sintering uses an additional sintering aid or secondary phase which melts during the thermal treatment enhancing the densification of powder which are difficult to densify via solid state methods (e.g. liquid phase sintering of Si_3N_4 ceramics). In the course of this work liquid phase sintering will not be applied, hence the following subchapters will be

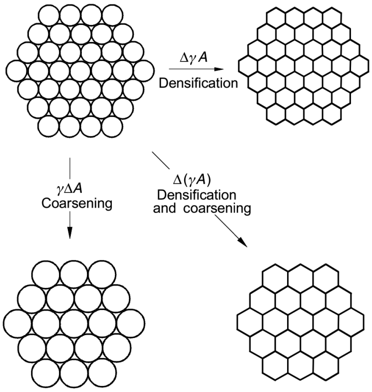

Fig. 2.3 Schematic visualization of coarsening and densification mechanisms which occur during sintering. Both processes are induced by the reduction of Gibbs free energy, which is the main driving force in solid state sintering. Adapted from [37]

focused exclusively on solid state sintering.

The general driving force during solid state sintering is the reduction of free energy in the system. Three different driving forces are available to reduce the total energy of the system: (I) The surface energy stored in the curvature of particles (II), additionally applied mechanical pressure and (III) chemical reactions. The influence of externally applied pressure will be discussed in section 2.2.3 in detail and chemical reactions as a driving force will not be considered further because reactive sintering is not relevant for the scope of this work.

In the case of a non-reactive, single phase ceramic powder compact, which is sintered freely in air, the main driving force is the stored surface energy. The interfacial energy stored in a ceramic powder can be described as $\gamma \cdot A$. Here, γ is the specific interface (for the case of powders, surface) energy and A is the surface area. A reduction of the free energy of the system can be described as:

$$\Delta(\gamma A) = \Delta\gamma A + \gamma\Delta A \tag{2.1}$$

where the difference in surface energy $\Delta\gamma$ is induced by densification and the difference in interfacial area ΔA is caused by particle coarsening. In general the reduction of surface energy can be understood by a replacement of solid-gas interfaces (surfaces) by solid-solid interfaces (grain boundaries). In a conventional sintering process both processes occur simultaneously described by the term $\Delta(\gamma A)$. The basic phenomena of sintering through the reduction of interfacial energy and simultaneous grain coarsening is schematically displayed in Fig. 2.3.

The sintering process can be divided into three overlapping stages. The development of relative density over time is displayed in Fig. 2.4 and highlights the different stages during a normal densification process. The sintering process is divided in: (I) The initial stage, (II) the intermediate stage and (III) the final stage. Additionally the starting condition can be considered as a distinct stage due to the large influence of the green body properties onto sintering. During the initial stage the sintering process is dominated by the formation of inter-particle necks. In general, neck formation has

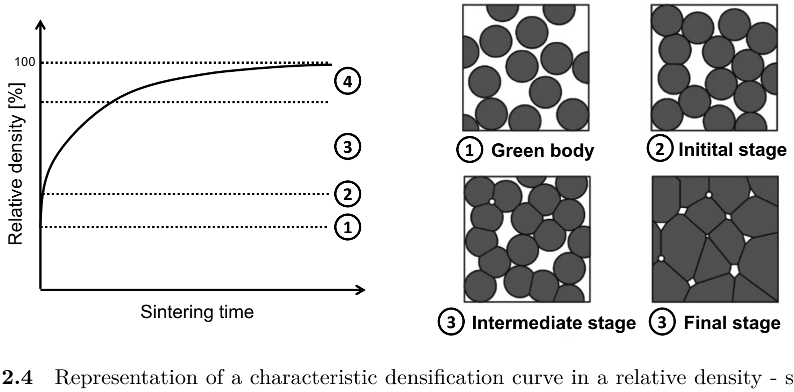

Fig. 2.4 Representation of a characteristic densification curve in a relative density - sintering time diagram and the associated stages of sintering. Adapted from [37] and [38]

Tab. 2.1 Parameters influencing the sintering process and the microstructure evolution. Adapted from [37].

Raw material (Morphological properties)	Shape, size, size distribution, agglomeration state mixedness
Raw material (Chemical properties)	Composition, impurities, non-stoichiometry, chemical homogeneity
Green body properties (Process variables)	Porosity, green density, pore size distribution, homogeneity
Sintering parameters (Process variables)	Temperature, time, pressure, oxygen partial pressure, heating and cooling rate

only a minor contribution to the overall densification. It is characterized by small total shrinkage values of around 2-3 %. The intermediate stage mainly contributes to the densification process by achieving up to around 93 % relative density and is characterized by an interconnected porosity. In the final stage of sintering isolated pores remain at the formed grain boundaries and final densification is dominated by pore removal. Due to the high complexity of the sintering process, all three stages are generally analysed with different models, which are optimized for describing the processes dominating the densification at their particular stage on a microscopic level.

In general, the sinterability of a certain material is dependent on a large number of parameters. These variables are summarized in Tab. 2.2 and can be divided into different influencing factors: (I) powder properties, (II) chemical composition and impurities, (III) green body properties and (IV) sintering parameters.

2.2.2 Mechanisms controlling sintering

The sintering process in polycrystalline materials is rather complex due to the presence and continuous change of interfaces between crystallites, which are called grain boundaries. The transport of matter, which leads to the decrease of the total free Gibbs energy as described in section 2.2.1, can occur by six different mechanisms. All of the mechanisms controlling sintering lead to neck growth between different powder particles but only three of them contribute to densification. The other three mechanisms predominantly contribute to neck formation and cause particle coarsening. During the various stages of sintering different mechanisms can be active at the same time inducing a complex interplay of overlapping mechanisms. In general, sintering of polycrystalline materials is controlled by diffusion processes and the microstructure of the powder compact dictates the diffusion pathways which are energetically favourable from a thermodynamic point of view. The six sintering mechanisms which can occur during the sintering of polycrystalline ceramics are displayed in Fig. 2.5. Hereby, three particles are forming necks with each other creating new solid-solid interfaces (grain boundaries) and an isolated intragranular

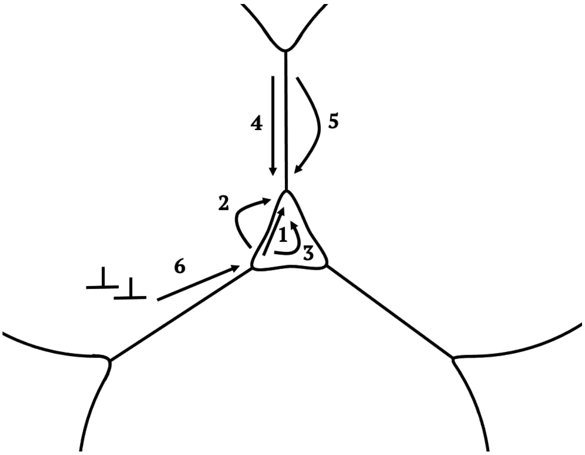

Fig. 2.5 Schematic sketch of the sintering mechanisms leading to neck formation and grain coarsening (1-3) and shrinkage (4-6) in the three particle model. (1) Surface diffusion (2) Lattice diffusion from the surface (3) Evaporation and re-condensation (4) Grain boundary diffusion (5) Lattice diffusion from the grain boundary (6) Plastic flow through dislocations. Adapted from [36].

pore in the centre. Mechanisms 4-6 are responsible for densification. Therefore, matter is diffusing from the grain boundary to the neck area leading to shrinkage of the powder compact. The so-called non-densifying mechanisms (1-3) induce a matter transport from the surface of the particle to the neck region leading to neck formation and particle coarsening without contributing to overall shrinkage. Nevertheless, these mechanisms lead to a reduction of the particle curvature, which reduces the main driving force of sintering and thus decreases the overall densification rate. Therefore an optimized process parameter selection is crucial in designing sintering cycles to reduce the influence of coarsening mechanisms. One critical microstructural feature which has major impact on the sintering behaviour of polycrystalline ceramics are the grain boundaries. During the densification process the particle surface area A_{sv} decreases significantly but a part of the stored energy is required to generate new solid-solid interfaces which have their own interfacial energy γ_{gb} and area A_{gb}. The appearing energy difference can be described by:

$$\Delta E = \gamma_{sv}\Delta A_{sv} + \gamma_{gb}\Delta A_{gb} \tag{2.2}$$

where ΔA_{sv} and ΔA_{gb} are the changes in surface and grain boundary area and γ_{sv} and γ_{gb} the corresponding interfacial energies. This means that the overall driving force for sintering is considerably lower as described in Eq. 2.1 due to the formation of new interfaces in the form of grain boundaries. This energetic considerations allows to consider processing conditions where the energy difference ΔE is positive

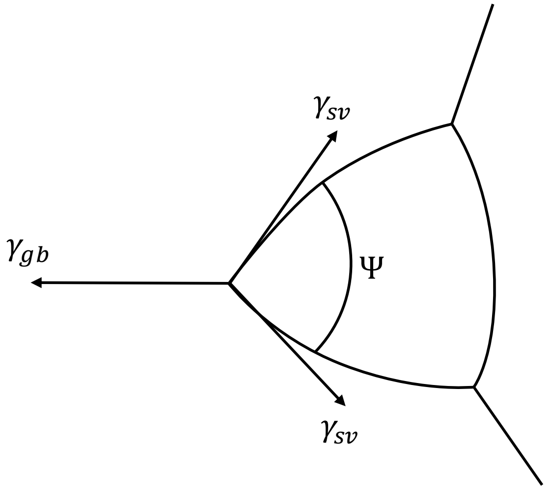

Fig. 2.6 Equilibrium shape of a pore at the triple boundary of three grains. The relationship between the interfacial forces of the grain boundary and the surface-vapour interface are represented through the dihedral angle Ψ. Adapted from [36].

implying that:

$$|\gamma_{gb}\Delta A_{gb}| > |\gamma_{sv}\Delta A_{sv}| \tag{2.3}$$

which suggests that the surface area has to increase during the thermal treatment, e.g. through the growth of pores. Additional to energetic considerations, grain boundaries also control the equilibrium shape and the interfacial forces acting at pores. The forces representing the stress at the interface must be balanced at the intersection of pore and grain boundary as displayed in Fig. 2.6. The surface forces at the pore are tangential to the interface while the grain boundary force lies in its plane. From this geometrical consideration the force balance equation can be written as:

$$\gamma_{gb} = 2\gamma_{sv}\cos(\Psi/2) \tag{2.4}$$

where Ψ is the dihedral angle. The most important process for microstructure evolution of polycrystalline materials, which originates from the existence of grain boundaries, is the possibility to reduce the overall energy in the system by decreasing the grain boundary area inside the powder compact. This process is called grain growth and will be introduced in detail in section 2.3. Despite being present during sintering, grain growth is normally investigated separately from densification processes due to the complicated interplay between both mechanisms and a lack of sufficient modelling approaches. The gained understanding of separate investigations on sintering and grain growth can afterwards be discussed together to draw conclusions on the interplay between both processes.

2.2.3 Pressure assisted sintering

One major problem often occurring during the sintering of ceramic and metallic powders is that the driving force related to the surface energy of the powder compact is not high enough to reach sufficient densification rates. Especially high temperature ceramics and refractory metals which exhibit high melting points tend to be difficult to sinter. For these materials, the use of externally applied pressure can imply an additional driving force which exceeds the intrinsic surface energy stored in the system. Different sintering processes have been developed which enable to apply pressure during sintering: Hot pressing (HP), hot isostatic pressing (HIP) and field assisted sintering (FAST/SPS) are the most common.

This section gives a short introduction of the additional mechanisms and models which have been proposed to describe the pressure assisted sintering process. Both models which are relevant for describing the sintering under external pressure were developed by Coble [39, 40]. The suggested models combine surface energy and applied stress as a driving force for sintering. The first model adapts the analytical sintering approach which was earlier developed by Coble himself and a second one uses a modification of creep equations developed by Herring [41]. Especially the modification of creep models, which generally describe the deformation of dense solids at elevated temperatures, is successful in describing the sintering process during hot pressing. The hot pressing model of Coble relates the densification rate to the applied stress modified by a compensation factor for porosity, yielding a stable model framework for this purpose.

For the description of hot pressing the driving force (DF) induced by the surface energy γ_{sv} gets linearly extended by the applied pressure:

$$DF = p_e + \gamma_{sv} K = p_a \Phi + \gamma_{sv} K \tag{2.5}$$

where p_e is the effective stress, K is the curvature of the pore, p_a the actual applied stress and Φ is the stress intensification factor. The curvature of the pore is depending on the stage of sintering (for intermediate stage $K = {}^{1}\!/_{r}$, for final stage $K = {}^{2}\!/_{r}$) and the stress intensification factor is defined by:

$$\Phi = \frac{1}{1-P} = \frac{1}{\rho} \tag{2.6}$$

here P is the amount of porosity in the material and ρ the relative density. The stress intensification factor is a multiplying factor which accounts to the presence of porosity in the powder compact leading to increased stresses at the powder particle contact area. The intrinsic driving force induced by the surface energy is small in comparison to the applied mechanical pressures in hot pressing and FAST/SPS, which are usually in the range of 10 - 200 MPa.

Using Eq. 2.5 additionally highlights that the applied pressure is now the main driving force of densification. However, applying an additional pressure to the powder compact does not accelerate the non-densifying mechanisms, which lowers their impact on the sintering process. In addition to the densifying mechanisms which are already active during conventional sintering (Fig. 2.5 mechanisms 4-6), additional

Tab. 2.2 Mechanisms of densification during hot pressing and corresponding exponents for the hot pressing model by Coble which is derived from creep equations. Adapted from [36]

Mechanism	Grain size Exponent (m)	Pressure Exponent (n)	Diffusion Coefficient
Lattice diffusion	2	1	D_l
Grain boundary diffusion	3	1	D_{gb}
Plastic deformation	0	>3	D_l
Viscous flow	0	1	—
Grain boundary sliding	1	1 or 2	D_l, D_{gb}

pressure induced mechanisms can be activated: (I) particle rearrangement (II) viscous flow and (III) grain boundary sliding. Particle rearrangement is especially active during the initial and intermediate stage of sintering increasing the green density and the rapid densification during the intermediate stage. Grain boundary sliding is recognized as the major mechanism that accommodates the grain shape differences induced by diffusion under applied pressure. If we assume that the applied pressure is dominating the densification during hot pressing, which means $p_a\Phi >> \gamma_{sv}K$, a general description of the densification rate derived from creep equations can be written as:

$$\frac{1}{\rho}\frac{d\rho}{dt} = \frac{HD\Phi^n}{G^m kT}p_a^n \tag{2.7}$$

where H is a constant, D is the diffusion coefficient of the active mechanism, G is the grain size, k is the Boltzmann constant, T is the absolute temperature and m and n are exponents which are dependent on the active densification mechanism. Therefore, Tab. 2.2 gives an overview of the densification mechanisms and their corresponding grain size and pressure exponents. This equation can be applied to indicate the active densification mechanisms for a given set of sintering conditions like applied pressure, grain size and temperature. A thorough analysis based on this equation was presented by Langer et al. comparing the sintering behaviour of nano-crystalline alumina [42] and zirconia [43] during hot pressing and FAST/SPS. In summary, the application of external mechanical pressure during sintering is an effective measure to increase the densification rates especially for materials which are difficult to sinter. Additionally, the modelling approach by Coble gives a straightforward analysis tool to indicate the sintering mechanisms during pressure assisted sintering, which can help to optimize the processing of ceramics via HP and FAST/SPS.

2.3 Grain growth and microstructure control

In this second section on fundamentals of ceramic processing, grain growth and microstructural evolution are introduced. Therefore, the fundamental mechanisms governing microstructure coarsening are established and possible mechanisms which control the migration of interfaces in solids are discussed. Here, two theories are presented which enable microstructure control: (I) The inclusion of secondary particles or pores leading to Zener pinning and (II) Doping of soluble phases which segregate on or in the vicinity of the grain boundary and induce solute drag. Finally, the application of doping to control the evolution of microstructures in Y_2O_3 will be discussed. A thorough overview on the current state of research will be given to discuss the experimental results obtained in this work.

2.3.1 Fundamentals of grain growth

One distinctive feature of polycrystalline solids is the existence of solid-solid interfaces formed between crystallites having a different orientation. These so-called grain boundaries are microscopic features representing a highly defective zone between the ordered structure of the neighbouring grains. In general, the width of a grain boundary is in the nm range depending on the disorientation angle and the amount of additional impurity or dopant atoms. As introduced earlier, grain boundaries allow an additional pathway to decrease the total Gibbs energy by reducing the total amount of interfacial areas ($\gamma_{gb}\Delta A_{gb}$). The reduction of interfacial area is enabled through the microstructural process of *grain growth.*

Grain growth describes the coarsening process of certain grains in the microstructure while others are simultaneously shrinking due to the conservation of matter. The sketch in Fig. 2.7 illustrates the process at the interface on an atomistic level. Single atoms at the grain boundary detach from their place in the host lattice and migrate to

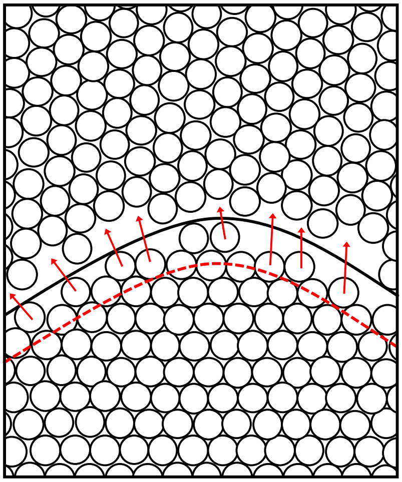

Fig. 2.7 General mechanism of grain growth. Atoms are migrating from their host lattice to a lower energy lattice position in the adjacent gain, moving the grain boundary in the opposite direction towards the curvature of the smaller grain. Graph adapted from [36].

the adjacent grain. The movement of atoms from one lattice to another is controlled by the curvature of the grain boundary in the area where the transport takes place. Due to the higher chemical potential of the convex side of a grain boundary, atoms reduce their thermodynamic potential by moving through the defective region. Vice versa, the grain boundary is moving in the opposite direction towards the centre of the curvature. This mechanism leads to growth of bigger grains and the shrinkage of smaller grains over time.

Grain growth during sintering and in the consolidated state is of major importance to control and optimize the processing and the final properties of the sintered component. Achieving high relative densities is crucial for attaining ceramics with excellent mechanical and functional properties. Therefore, reducing grain growth during sintering is necessary to reach high relative densities because the increase of grain sizes lowers the overall driving force for densification. For sintering processes, which are controlled by diffusion, the densification rate can be described as:

$$\frac{1}{\delta}\frac{d\delta}{dt} = \frac{K}{G^m} \tag{2.8}$$

where K is a constant at a certain temperature, G is the average grain size and m is a coefficient defined by the active diffusion mechanism ($m = 3$ for lattice diffusion, $m = 4$ for grain boundary diffusion). Through an increase of grain size by uncontrolled grain growth during the densification, diffusion paths are increased which lower the shrinkage rate. Furthermore, most of the properties of ceramic materials depend on the grain size, making the control of microstructure evolution a key to optimize material properties. Important examples are mechanical properties

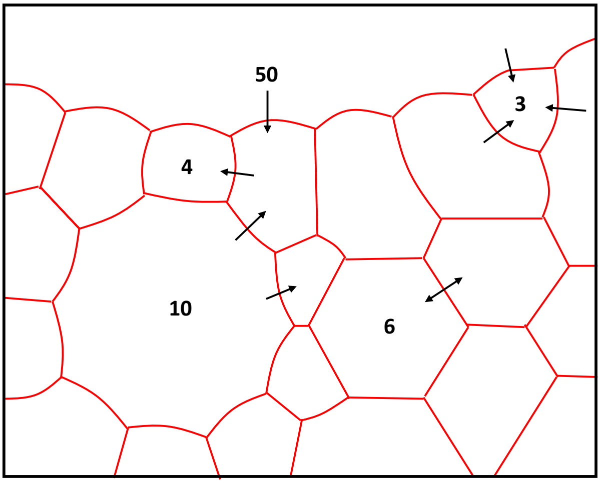

Fig. 2.8 Theoretical consideration of a two dimensional cross section through a theoretical dense microstructure with $\Psi = 120°$. The curvature of the grains is determined by the number of sides leading to convex (n<6) and concave grain boundaries (n>6), which determines the local direction of boundary migration. Graph adapted from [36].

like fracture strength, which is directly proportional to $1/\sqrt{G}$ for grain sizes larger than 1 μm [44, 45]. Other functional properties like the ionic conductivity of lithium and sodium conducting ceramics [46, 47], the dielectric constant of barium titanates [48] and various other examples exist where control of grain growth is essential to yield materials with optimized properties.

In a stable topological microstructure exhibiting isotropic grain boundary energies ($\gamma_{gb} = const.$), Eq. 2.4 shows that the dihedral angle of 3 intersecting interfaces has to be 120°. A two dimensional intersection through a dense microstructure following this assumption is shown in Fig. 2.8. Here, all dihedral angles Ψ are 120 ° which defines the curvature of all grains boundaries in this example. Crystallites with fewer than 6 sides show concave grain boundaries and for grains with more than 6 sides the curvature becomes convex. Due to thermodynamic reasons atoms migrate from the concave boundary to the convex one, forcing the interface in the opposite direction. These fundamental topological requirements induce grains with $n < 6$ to shrink while grains with $n > 6$ tend to grow in the course of microstructure evolution, especially at high temperatures and long dwell times.

The theoretical analysis of grain growth is rather complex for real microstructures due to complex grain shapes and the presence of porosity during the sintering process. Therefore, the analysis of grain growth in dense ceramic polycrystalline materials is a helpful simplification to understand the fundamental processes and to indicate the main influencing factors. The first theoretical approach proposed by Burke and Turnbull [49] is based on the transport process of atoms across the boundary driven by a chemical potential. They described the rate of grain growth as proportional to the changes of average grain size, yielding a global variable called grain boundary velocity v_b:

$$\frac{dG}{dt} \sim v_b \tag{2.9}$$

where G is the average grain size of the investigated microstructure. The boundary velocity can be described by the product of the grain boundary mobility M_b and the local driving force acting on the interface F_b:

$$v_b = M_b F_b \tag{2.10}$$

As mentioned earlier the driving force across the grain boundary is defined by the chemical potential, however this would require to include the atomic flux into the equations. Instead of this the driving force can also be interpreted as a pressure difference across the grain boundary $\alpha\gamma_{gb}/G$ which gives the velocity of grain growth as:

$$v_b \sim \frac{dG}{dt} = M_b \frac{\alpha\gamma_{gb}}{G} \tag{2.11}$$

The integration of equation 2.11 therefore gives:

$$G^2 - G_0^2 = 2\alpha M_b \gamma_{gb} t \tag{2.12}$$

where G_0 is the initial grain size, G is the grain size after the thermal treatment for the time t, α is a geometrical factor and the mobility M_b is defined by the diffusional flux of atoms across the boundary:

$$M_b = \frac{D_a \Omega}{kT\delta_{gb}} \tag{2.13}$$

where D_a is the diffusion coefficient across the grain boundary and Ω is the atomic volume. Equation 2.12 is called the parabolic grain growth law which defines the grain growth kinetics at a defined temperature T. This relationship can be used to derive the grain boundary mobility M_b by investigating the microstructural evolution after different times at a certain temperature. Several assumptions have to be made to allow this rather simple analytical analysis: The interfacial energy γ_{gb} as well as the grain boundary thickness δ_{gb} are assumed to be constant for all grain boundaries. However, combining the critical and hard to define parameters in the parabolic grain growth law to the grain growth constant K with $K = 2\alpha M_b \gamma_{gb}$ helps to analyse and compare different grain growth data sets and experiments.

2.3.2 Mechanisms controlling grain boundary migration

The parabolic grain growth law, which was introduced in the preceding section can be applied to describe the grain growth kinetics in a defect and secondary phase free polycrystalline material. However, in real microstructures defects like secondary phase particles and pores are usually present and have to be taken into account when investigating the grain boundary kinetics. Even if highly densified samples are investigated, different additional effects can significantly influence the intrinsic grain boundary mobility. Therefore, two theoretical concepts are introduced below to allow a thorough analysis and discussion of the grain growth experiments on pure and rare earth doped Y_2O_3 ceramics, which will be presented later. Firstly, the influence of secondary inclusions on the grain boundary mobility, which is in general referred to as Zener pinning will be presented. Secondly, the solute drag effect is introduced, which is used to describe the influence of segregated dopant species on grain boundary kinetics.

Zener pinning at pores and inclusions

In the following section the interaction between an immobile and non-solvable inclusion and a moving grain boundary will be discussed. For these considerations a polycrystalline material system is assumed which contains a homogeneously distributed secondary phase that has a grain size smaller than the average grain size of the matrix. The theoretical framework around Zener pinning was developed to describe the decelerating effects of secondary phases on grain boundary migration but can also be adapted for drag forces induced by pores located at the grain boundary. For the case that a migrating grain boundary is encountering a microstructural defect, which can be a secondary inclusion or a pore, the further movement of the interface is retarded. A sketch explaining the acting forces on the grain boundary is

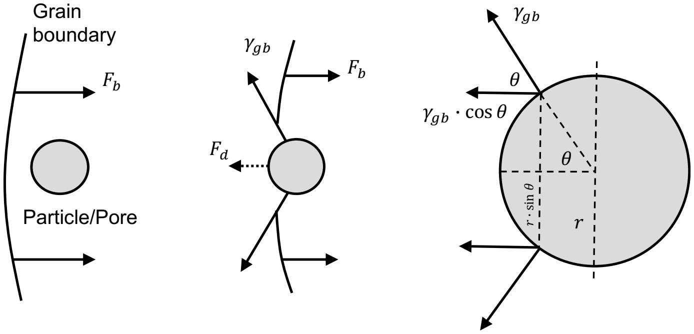

Fig. 2.9 Schematic sketch showing a migrating grain boundary interfering with an inclusion and the resulting forces derived from the geometric relationships of Zener pinning. Graph adapted from [36].

displayed in Fig. 2.9. Considering the driving force of the grain boundary is governed by the curvature of the two adjacent grains, F_b can be described as:

$$F_b = \frac{\alpha\gamma_{gb}}{G} \tag{2.14}$$

where α is a geometrical factor describing the shape of the growing grain ($\alpha = 2$ for spherical grains). When interacting with an inclusion, the grain boundary becomes circular shaped around the particle and further energy has to be applied to maintain grain boundary migration. The drag force acting in the opposite direction of the interfacial movement can be described as:

$$F_d = (\gamma_{gb}\cos\theta)(2\pi r\sin\theta) \tag{2.15}$$

where θ is the angle forming between the centre of the inclusion and the wrapping interface and r is the radius of the particle. As F_b is acting directly opposite to the grain boundary movement this drag force can significantly decrease the grain boundary migration leading to Zener pinning, where the driving force becomes too low for separating the interface from the inclusion stopping further movement.
Transferring this local effect to a solid polycrystalline body is possible by relating the drag force to the volume fraction of the secondary inclusions and deriving a net driving force:

$$F_{net} = F_b - RF_d^{max} = \gamma_{gb}\left(\frac{\alpha}{G} - \frac{3f}{2r}\right) \tag{2.16}$$

where RF_b^{max} is the maximal retarding force and f is the volume fraction of the inclusions. This relationship clearly describes the limiting factors of grain growth due to drag forces induced by pores and inclusions. If the net driving force reaches zero ($F_{net} = 0$), grain growth in a theoretical material system with a fixed amount of inclusions of one average size ceases. The maximal grain size which can be determined for this boundary condition G_{max} can be defined as:

$$G_{max} = \frac{2\alpha r}{3f} \tag{2.17}$$

Even though these theoretical considerations include a lot of estimations, the fundamental relationships are becoming obvious and provide a good basis for better understanding of particle and pore drag in polycrystalline materials.

The solute drag effect of dopants and impurities

Another important mechanism which can be applied to control the grain boundary movement during the processing of polycrystalline ceramics is associated to the impact of segregated solute atoms on the grain boundary movement. In this case, soluble dopants are included in the lattice structure and segregate to the interface forming a strong local gradient. This local gradient changes the chemical and structural composition at the grain boundary and therefore influences the migration of atoms perpendicular to the interface resulting in a change of the grain boundary migration behaviour. This so-called solute cloud moves along with the grain boundary inducing a decelerating force which is called *solute drag*. A schematic visualization of a migrating grain boundary with a solute cloud is displayed in Fig. 2.10. Due to the differences in perpendicular diffusion rates of the host and solute atoms, the concentration gradient becomes asymmetric and solute drag is subjected to the grain boundary. If the driving force for grain growth is high enough the grain boundary is able to separate from the dopant concentration gradient and leaves behind a solute cloud inside the grain. After removal of the solute cloud from the grain boundary the migration rate can highly increase by approaching the materials intrinsic grain boundary mobility M_b. In the following section a short summary of the extensive analytical description of solute drag which was introduced by Cahn in 1962, will be given to summarize the main influencing factors governing segregation induced grain boundary drag [50]. The model of Cahn is using some assumptions to simplify the

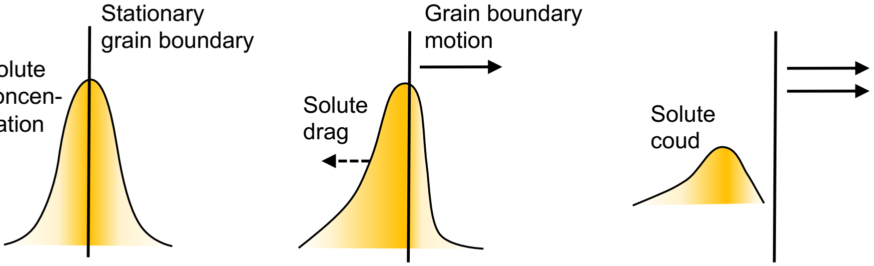

Fig. 2.10 Schematic behaviour of a solute cloud of segregated dopant atoms. (I) Symmetric concentration gradient in the stationary condition (II) Asymmetric concentration gradient of the solute cloud surrounding a migrating grain boundary. Solute drag is acting upon the moving interface reducing its overall velocity. (II) Breakaway of the solute cloud at high grain boundary velocities. Graph adapted from [36].

analytical description of the solute drag effect: (I) The dopant species is assumed to be only a small fraction of the host atoms.(II) An interaction potential exists between the dopant atoms and the grain boundary which is defined as $U(x)$. It is independent from the boundary velocity and the dopant concentration and is only a function of the distance from the boundary x. (III) The grain boundary velocity is constant.

In the model of Cahn, comparable to Zener pinning, a decelerating force gets exerted by the dopant atoms concentrated around the grain boundary. The total solute drag force F can be described as the sum of the intrinsic drag F_b (Eq. 2.10) plus the drag force induced by the dopant atoms F_s:

$$F = F_b + F_s = \frac{v_b}{M_b} + \frac{\lambda C_\infty v_b}{1 + \beta^2 v_b^2} \tag{2.18}$$

where C_∞ is the concentration of dopant in the bulk of the grain (with a maximum distance from the boundary), and λ and β are complex parameters which are defined as:

$$\lambda = \frac{4 N_V k T \delta_{gb} Q}{D_b} \tag{2.19}$$

$$\beta^2 = \frac{\lambda k T \delta_{gb}}{2 N_V U_\infty^2 D_b} \tag{2.20}$$

where N_V is the number of host atoms in per unit volume, Q is a partition coefficient describing the dopant distribution from grain boundary to the bulk (Q is increasing with the degree of segregation) and U_∞ is the interaction energy of dopant atoms with the grain boundary. Cahn analysed the solute drag in two regimes, high and low grain boundary velocity, and Rahaman highlighted that especially for ceramics the low limit is more likely to be applied. For this case, it is possible to neglect the term $\beta^2 v_b^2$ in Eq. 2.18 which simplifies the description of the grain boundary velocity in the case of solute drag.

$$v_b = \frac{F}{{}^1/_{M_b} + \lambda C_\infty} \tag{2.21}$$

From this simplified description of the velocity, several relationships can be derived. Foremost, it becomes clear that the velocity is low, which means that the solute drag effect is high, when $\lambda C_\infty \gg {}^1/_{M_b}$. From this relationship some major factors can be deducted which trigger the solute drag effect in doped ceramics:

- The dopant concentration in the bulk is high ($C_\infty \Uparrow$) suggesting an overall high dopant concentration.
- The partition coefficient Q is high, meaning that a high amount of segregation of the dopant species to the grain boundary has occurred.
- The perpendicular diffusion coefficient of dopant species through the grain boundary (D_b) is small in comparison to the diffusion rate of the host atoms.

2.3.3 Microstructure control through doping of Y_2O_3

After introducing the fundamentals of sintering and grain growth, this final section discusses the application of doping to control the densification and microstructure development of Y_2O_3 ceramics. In most experimental studies, the sintering and grain growth behaviour are investigated apart from each other, just focusing on one of both phenomena. The same distinction will be made in the following: At first, applications of doping as described in the literature will be introduced and the general strategies, which are applied, will be discussed. After that, systematic studies of Chen et al. and Yoshida et al. are introduced, summarizing their extensive discussion of the effects of various dopants onto sintering and grain growth. Finally, the application of dopants for the production of transparent ceramics will be highlighted. Here, doping of yttria is already in industrial use for adjusting optical and mechanical properties. The first reported investigation of doping Y_2O_3 are from the 1960ies. Jorgensen and Anderson implemented a ThO_2 doping to increase densification and optimize final stage sintering of Y_2O_3 ceramics aiming on high relative densities [51]. A high amount of dopant species (up to 10 mol % ThO_2) was applied and extreme sintering temperatures of 2000 °C were needed for achieving complete densification. Later, Rhodes conducted a comparable study using the grain boundary drag effect of a transient secondary phase, which only exists at very high temperatures (La_2O_3), resulting in Zener pinning of grain boundaries and decreased grain growth kinetics [52]. In the following years, work by Katayama et al. mainly focused on the application of the divalent cations of CaO, MgO and SrO to increase the concentration of oxygen vacancies in the structure and thereby improve diffusion mechanisms. These dopants led to increased densification rates in the early stage of sintering as well as higher final relative densities [53, 54]. Finally, Baumard and Gasgnier investigated aliovant doping to decrease the sintering temperature [55, 56] by introducing tetravalent dopants through TiO_2, SiO_2, CeO_2 and ZrO_2. Especially doping with low amounts of TiO_2 between 0,2 and 1,0 wt.% promoted densification through increased diffusion kinetics. These early studies clearly indicate the two main strategies applied for promoting the densification of Y_2O_3:

- Reducing the interfacial mobility through a drag force by including tetravalent (Th^{4+}, Zr^{4+}) or trivalent (La^{3+}) cations: Here, the drag force is either caused by dopant segregation at the grain boundaries or by the occurrence of a transient solid second phase at very high temperatures.

- Improving the densification behaviour by including divalent cations (Ca^{2+}, Mg^{2+}, Sr^{2+}) or selected tetravalent cations (Ti^{2+}): In this case, the cations generate an increased oxygen vacancy concentration which decreases the activation energy for diffusion leading to improved densification.

The first systematic investigations on how doping influences the grain growth behaviour in polycrystalline oxides was conducted by Chen and Chen focusing on the fluorite structured CeO_2 [58, 59] followed by the C-type rare earth structured Y_2O_3 [57, 60]. The authors assumed that cation diffusivity controls grain boundary mobility in doped yttria, concluding that divalent cations (acceptors) accelerate

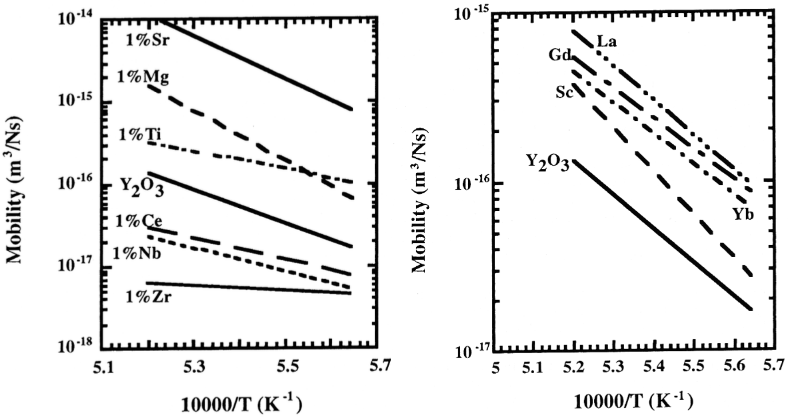

Fig. 2.11 Grain boundary mobility for a broad variety of doping elements with different valency. All compositions use a dopant concentration of 1 mol%. Taken from [57].

and tetravalent as well as pentavalent cations (acceptors) decelerate the the grain boundary velocity [61]. Additionally, enhanced mobilities were observed for dopants which exhibit a large size mismatch in comparison to the host lattice (Ti^{4+}, Nb^{5+}). In this case, the effects could not be attributed to defect chemistry. Trivalent dopants (La^{3+}, Gd^{3+}, Sc^{3+}, Yb^{3+}) also induced an acceleration of the grain growth kinetics which could not be associated to defect chemistry. Therefore, for this class of cations, a pronounced effect of lattice distortions induced by ionic size mismatches was assumed [57]. In the systematic studies of Chen and Chen, no final conclusion on the mechanism governing the influence of trivalent cations on the grain growth of Y_2O_3 was made mainly due to the lack of high resolution electron microscopy, which is crucial to determine the dopant distribution at the grain boundary. However, the optimized microstructural control which was facilitated through the profound understanding of the grain boundary kinetics induced through metal ion doping enabled to develop a two-step sintering method. This method allows to achieve high densities and to prevent almost all of the processing induced grain growth normally happening at the final stage of sintering [62, 63].

The first systematic study investigating the influence of cation doping on the sintering behaviour of Y_2O_3 ceramics was conducted by Kodo et al. focusing on co-doping yttria. They applied co-doping with Ni^{2+}/Er^{3+} and Mn^{4+}/Er^{3+}, which enabled a reduction of the processing temperature from 1600 °C to 1300 °C, while achieving a densification rates comparable to undoped compounds [64]. Further extensive sintering studies on doped yttria from the Yoshida group focused on divalent [65], trivalent and tetravalent cations [66]. Different interlocking mechanisms were discussed to be responsible for the observed effects of dopants: The segregation of selected cations (which have an ionic size mismatch) to the grain boundary, an increase of the oxygen vacancy concentration (for divalent cations) at the grain boundaries and changes of the ionicity of the oxygen anion [65, 66].

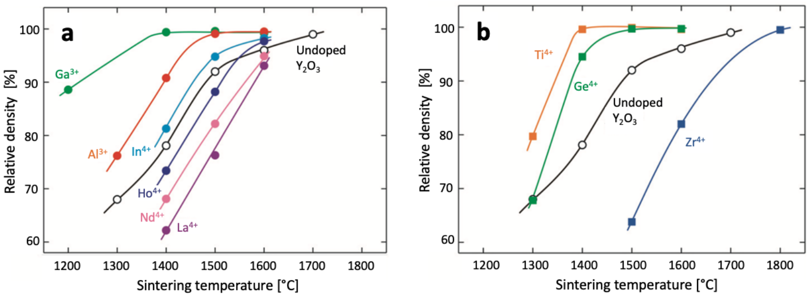

Fig. 2.12 Densification behaviour for a broad variety of doping elements with different valency. All compositions use a dopant concentration of 1 mol%. Taken from [66].

In addition, cation doping is widely used as a sintering aid for manufacturing transparent Y_2O_3. Various processing techniques (vacuum sintering, sintering in hydrogen atmosphere, HIP and combinations thereof) and application of different trivalent dopants [67, 68, 69, 70], tetravalent dopants [71, 72] as well as co-doping approaches [73, 74, 75, 76, 77] are reported in literature. Most investigations use a combination of both doping strategies, firstly an improved densification through increased defect concentration at the grain boundaries (I) and secondly, grain growth control in the final stage of sintering (II).

Despite the large amount of works discussing the advantage of cation doping to produce Y_2O_3 with optimized properties, the direct one step processing of doped yttria using FAST/SPS is rarely applied. Only two studies focus on a combination of cation doping and FAST/SPS processing: Yoshida et al. used 1 mol.% Zn^{2+} doping to strongly reduce the sintering temperature to 870 – 900 °C under high uniaxial pressures (170 MPa) [78]. Additionally, Furuse et al. applied a 1 to 50 mol.% Yb^{3+} doping and investigated the optimum amount for yttria when being used as a transparent laser ceramic [79]. The limited number of publications dealing with the processing of cation doped yttria during FAST/SPS sintering clearly indicate the need for further, thorough research in this field.

2.4 Field assisted sintering technology/spark plasma sintering (FAST/SPS)

After introducing the fundamental mechanisms of sintering with and without pressure and of grain growth, in the following chapter the FAST/SPS method will be presented focusing on the working principle, the mechanisms of sintering and the application of FAST/SPS for the consolidation of Y_2O_3.

2.4.1 Fundamentals and working principle

In the course of this work the main focus is put on the application and the industrialization of the consolidation and synthesis technique FAST/SPS. This technique is a field assisted, low voltage, direct current activated, pressure assisted sintering technique. Through combination of high temperature, direct current and uniaxial pressure it is possible to consolidate powder materials in a single processing step, often at reduced temperature and dwell time. The basic principle is comparable to hot pressing (HP) but instead of convection heating the temperature gets transmitted to the powder sample through Joule heating of the conducting tools and direct heat transfer. Tools are in most cases made from isostatic graphite. A sketch of the working principle of a FAST/SPS device is displayed in Fig. 2.13 (a). The device consists of a pulsed DC power source (Fig. 2.13 Nr. 10,11) which is connected to two steel punches, which act as electrodes and enable to load the toll by a hydraulic system. A vacuum chamber enables processing in vacuum or in an inert gas atmosphere. Other atmospheres are possible, but reactions of the tool materials or sample with the atmosphere must be taken carefully into account. The powder sample is filled into the pressing tool which is afterwards mounted between the steel electrodes for sintering. During sintering uniaxial pressures of maximal 80 MPa can be applied using standard graphite qualities and heating rates of up to maximal 300 K/min are possible, when small sample and tool sizes are applied. When graphite is used as the tool material, a maximal sintering temperature of 2200 °C is possible. The process parameters can be programmed and monitored using a control unit allowing

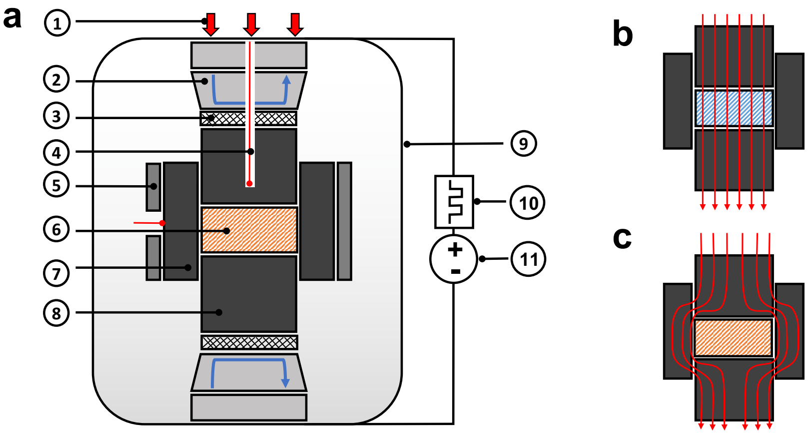

Fig. 2.13 Schematic sketch of a FAST/SPS sintering facility (a) and the material dependent current flow. Powders with a high (b) and low electronic conductivity (c) strongly influence the current flow and current density in the tool setup. (1) Uniaxial pressure via a hydraulic system (2) Water cooled steel electrode (3) Optional CFC spacer (4) Axial pyrometer (5) Graphite felt insulation (6) Sample (7) Graphite pressing die (8) Graphite pressing punch (9) Vacuum chamber (10) Electric pulse generator (11) DC power source.

to determine various sintering variables during densification.
The heat distribution inside the tool setup is strongly depending on the electrical conductivity of the applied materials. If the conductivity of the powder is higher than of the graphite tool, the current is diverted though the green body and supports the sintering process (Fig. 2.13 (b)). In case of non-conductive powder samples the current is running only through the tool, which can induce inhomogeneous heat distributions especially when high heating rates are applied. The heat is solely generated inside the tool by Joule heating and heat conduction is necessary to homogenize the occurring thermal gradients (Fig. 2.13 (c)) [18, 80].

2.4.2 Mechanisms of densification

The active mechanisms being responsible for consolidation of powders using by FAST/SPS can be divided into mechanical, thermal and electrical effects which act simultaneously. Furthermore, the atmosphere and the partial gas pressure inside the chamber influence the sintering process and the resulting material properties [18].
The fundamentals of pressure assisted sintering have been already described in detail in section 2.2.3 but further specific characteristics contribute to densification in FAST/SPS, which will be summarized below. The applied mechanical load in the FAST/SPS process leads to increased green densities with enhanced particle contact in the initial stages of sintering. Furthermore, the applied pressure increases the overall driving force for densification (Eq. 2.5) while having only a minor impact on diffusion mechanisms which cause grain growth [37]. Additionally to particle rearrangement and the increase of the driving force, high stresses are able to activate new densification mechanisms like plastic deformation and grain boundary sliding. However, the pressure which can be applied using graphite tools is limited to maximal 100 MPa by its moderate strength. For increased loads alternative tool materials (WC, SiC, Si_3N_4 or TZM) have to be applied, but there might be restrictions with respect to the maximum temperature [81, 82, 83].
Furthermore, thermal effects play an important role in the powder densification during FAST/SPS. Extremely high heating rates favour densification mechanisms with higher activation energy, like grain boundary diffusion, and retard coarsening mechanisms because the final sintering temperatures are achieved more rapidly. In ideal case, this enhances the densification rate and reduces grain coarsening effects at the same time. Moreover, high local temperature gradients, non-uniform thermal distribution and macroscopic temperature fields support the rapid but often inhomogeneous densification of FAST/SPS samples. Finite element simulations by different groups show the massive influence of tool design (tool thickness, diameter), tool material and powder material (electrical conductivity) on the thermal distribution inside the sample [84, 85, 86]. Especially during the consolidation of non-conductive materials over-heating effects at the edge of the sample occur and lead to thermal and therefore microstructural inhomogeneities. Advanced tooling concepts can overcome these problems as Giuntini et al. showed using modified pressing punches (circular holes and concentric ring shaped channels) and partly BN-coated tools to improve the thermal homogeneity during the consolidation of Si_3N_4 [87, 88]. All of the above

discussed effects enhance diffusion mechanisms active during FAST/SPS of powder compacts and therefore improve densification [18, 89].

Electrical effects on the densification mechanisms can be divided into field and current effects. Current effects are only expected when electrically conducting powder is used and can be divided in: percolation effects in the porous powder bed, Peltier effects at the interface between powder and pressings tools, electrochemical reactions and electromigration. All of these effects presume the existence of a current running through the powder compact and therefore are not likely to be found when processing non-conductive powders [18]. As electrically conductive materials play a minor role in the present work, these effects will be not further discussed.

Electrical fields without a current flow through the specimen can affect the defect concentration and the development of space charge layers leading to changed grain boundary migration rates (e.g. in $SrTiO_3$), but voltages above 50 V/mm are necessary for those effects [90, 91]. However, for selected cases (e.g. Gd doped CeO_2) the voltages observed during FAST/SPS have shown similar effects leading to inhomogeneous microstructure evolution due to polarity [92]. Nevertheless, investigations on stable oxides have shown that almost no electrical field effects are observable. Studies by Langer et al. investigated the consolidation of Al_2O_3 or ZrO_2 with FAST/SPS and hot pressing [42, 43] and found no changes of the densification mechanism. Further investigations using higher electrical fields are necessary to understand the influence of field activation at elevated temperatures in field assisted sintering [18].

2.4.3 Field assisted sintering of Y_2O_3

The following paragraph will give a brief overview on scientific studies dealing with FAST/SPS of Y_2O_3 ceramics. The densification of polycrystalline Y_2O_3 is complex because of the high melting temperature (2410 °C) and therefore high temperatures and elaborated sintering methods like vacuum sintering or hot isostatic pressing (HIP) are needed to achieve fully dense parts. Hence, FAST/SPS offers significant advantages over conventional processing routes and was investigated by several groups which tried to lower the sintering temperatures or to increase the density through optimized sintering cycles. Tab. 2.3 summarizes the sintering parameters which were applied in literature for FAST/SPS of Y_2O_3 ceramics. Two main strategies can be derived from the literature study:

I) The research group of Yoshida et al. uses moderate sintering temperatures from 850 to 1050 °C combined with low heating rates and long dwell times. This enables a steady densification at low temperatures which impedes grain coarsening and thereby enables nano-sized microstructures at high relative densities. Yoshida et al. highlight the possible influence of electric field effects on the defect concentration during consolidation which could be able to improve matter transport and therefore the sinterability [20, 93]. Further investigations done by Zhang et al. use comparable parameters and are able to sinter Y_2O_3 to densities enabling transparency by using elevated uniaxial pressures of 200 to 300 MPa [82]. Both approaches use a careful design of the sintering cycle with slow heating rates to avoid thermal gradients. Furthermore, conducting FAST/SPS with high pressures at low temperatures allows to reduce grain growth and preserves a high driving force for sintering even at high relative densities.

II) The second group of publications focuses on shortening cycle times by applying increased sintering temperatures and high heating rates at uniaxial pressures of 100 MPa. Chaim et al. described the densification of nano-crystalline yttria powders using temperatures from 1100 to 1600 °C at different heating rates and dwell times of 5 min. The maximum of relative density was observed at 1400 °C. A further increase yielded lower relative densities which could be caused by activating competing mechanisms (densification ↔ enhanced grain growth) at temperatures above 1400 °C [19]. Subsequent studies by Marder et al. observed a grain growth stagnation during isothermal dwell experiments at 1100 °C varying the dwell time between 10 - 30 min. While grain growth was strongly decreased, densification continued resulting in an increase of the relative density from 95,0 to 98,5 %. Theoretical calculations considering drag effects based on triple junctions and nano pores suggested that grain growth stagnation is mainly induced by nano pores at grain boundaries which ceased after sufficient dwell time at high temperature, then followed by rapid grain growth [94]. Further publications focused on the optimization of the optical transmittance through variations of processing parameters. Most of the investigations varied the main process parameters sintering temperature, heating rate and dwell time to influence the microstructure and thereby optical properties. An et al. applied slow heating rates of 10 K/min and long dwell times up to 45 min achieving highly dense samples at intermediate temperatures of 1300 °C [21]. Studies by Ahmadi et al. and Razavi et al. applied comparable parameters (but increased heating rates) and reported similar trends [95, 96]. General observations reveal the high impact of sintering temperature on the densification and grain growth in the final stage of sintering. Thereby, temperature is the main factor to control the microstructure and optical as well as mechanical properties.

Tab. 2.3 Overview on the FAST/SPS sintering parameters applied in various studies with pure Y_2O_3 powders.

Sintering Temperature [°C]	Pressure [MPa]	Heating Rate [K/min]	Dwell time [min]	Source
650 – 1050	83	10	60	Yoshida 2008 [20]
850 – 1050	80	2- 50	60	Yoshida 2011 [93]
1050	200 – 300	20	60	Zhang 2011 [82]
1100 – 1600	100	10	45	An 2012 [21]
1100 – 1600	100	50, 100, 180	5	Chaim 2009 [19]
1200 – 1600	100	100	20	Ahmadi 2016 [95]
1100	100	180	5 - 40	Marder 2010 [94]

Both strategies, which were applied in the literature for the densification of Y_2O_3 ceramics, are able to yield dense ceramic samples. However, only nano-sized powders were applied in all presented studies, with primary particle sizes ranging from 18 to 40 nm. The broad variety of processing parameters hints on the manifold possibilities offered by FAST/SPS. A broad range of sintering temperatures, heating rates and dwell times enable to achieve fully dense samples. However, sample sizes realized so far did not exceed the lab-scale indicating the main challenge of processing ceramics via FAST/SPS. Increased sample sizes induce the risk of larger thermal gradients resulting in inhomogeneous microstructures. To overcome current limitations, advanced tool engineering and process control as well as process simulation are necessary.

2.5 Plasma etching for semiconductor applications

The final section introduces the theory and the current state of research in the field of reactive plasma etching. An overview on the basic principles of reactive ion etching using fluorine based chemistries will be given. Hereby especially the formation of a characteristic fluorocarbon film during plasma processing will be introduced. A specific focus will be the interaction of reactive plasma species with polycrystalline ceramics.

2.5.1 Fundamentals of reactive plasma etching

Reactive plasma etching is a plasma assisted processing technique which uses chemical reactants to effectively remove or deposit material on a substrate. This method has numerous applications in the microelectronic and semiconductor industry due to its broad variability concerning processable materials, selectivity and efficiency. In the following paragraph reactive plasma etching using fluorine based components will be introduced, due to its broad application spectrum in different stages of the microelectronic manufacturing chain, making it the most applied etching chemistry. The main functional layers and components which are produced using reactive plasma etching are transistor gates (Si etching), dielectric layers (SiO_2 etching) or spacer layers (SiO_2 or Si_3N_4 etching) in microelectronic devices [97].

During reactive plasma etching a mixture of the inert plasma gas (mostly Ar) and the reactive fluorine species (CF_4, SF_6, CHF_3 or C_4F_8) are ionized either through inductively or capacitively coupled plasma generators. The energy introduced into the system allows to initiate different plasma reactions mechanisms mainly controlled by dissociation (2.22), ionization (2.23) and attachment (2.23), which are displayed below for the application of CF_4 [97].

$$CF_4 + e^- \longrightarrow F + CF_3 + e^- \tag{2.22}$$

$$CF_4 + e^- \longrightarrow CF_3^+ + F + 2e^- \tag{2.23}$$

$$CF_4 + e^- \longrightarrow CF_4^- \longrightarrow CF_3^- + F \tag{2.24}$$

These processes create a gas mixture in the plasma chamber that consists of initial molecules, single fluorine atoms, radicals, electrons as well as positive and negative ions. The various components of the ignited plasma gas atmosphere serve different functions during the etch process. The ionized Ar ions are accelerated by the additionally applied DC-bias and lead to a physical sputtering of sample material or process induced polymer layers. These layers are generated by the deposition of fluorocarbon radicals (CF_x) through adsorption processes at the sample surface. The nm-thick polymer layer is of large importance during the interaction of inorganic materials with the plasma because it facilitates the surface fluorination and induces a high selectivity (especially for Si-SiO_2). Therefore, the different reaction processes which are taking place on the sample surface in an Ar/CF_4 plasma are displayed in Fig. 2.14 [98, 99].

The polymer layer formation is controlled by deposition and removal processes which are induced by different molecular and ionic gas components. Fluorocarbon radials form the polymer layer directly on the sample surface through adsorption processes (1). A similar effect leads to the further growth of the layer (2). On the other hand fluorine atoms (3) and ionic bombardment (4) lead to material removal through chemical and physical interaction with the polymer layer [100, 101, 102]. Both removal and deposition processes are forming an equilibrium condition which is controlled by the gas composition and the applied bias voltage. Additional control of the polymer layer formation is possible through the addition of O_2 (reduction of layer formation [103]) or H_2 (increase of layer formation [104]) to the plasma gas composition.

The chemical interaction of the substrate with the deposited fluorocarbon layer is strongly dependent on the substrate material as well as its corresponding halogenide compounds [97]. Fluorocarbon containing plasmas are mainly applied for the processing of Si-based substrates due to the high selectivity between SiO_2 and Si, allowing the fabrication of structures with a high geometrical ratio. Furthermore, Silicon compounds are decomposing into volatile reaction products (Eq. 2.25 [105]) reducing the risk of detrimental particle formation and increasing the overall purity inside the

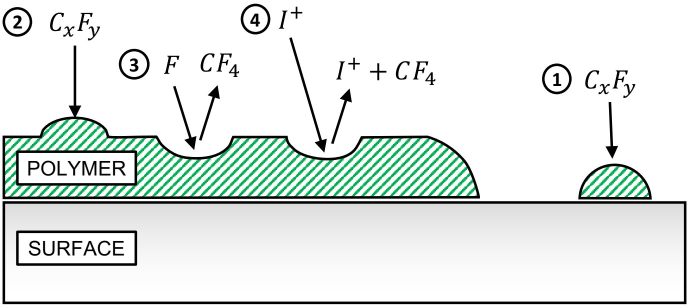

Fig. 2.14 Fluorocarbon polymer layer deposition mechanisms during the reactive plasma etching with CF_4 as the reactant. (1/4) Fluorocarbon radical deposition through adsorption. (2) Direct reaction of fluorine atoms with the polymer layer. (3) Physical sputtering of the polymer layer by accelerated ions. Graph adapted from [100].

plasma chamber.

$$SiO_2 + CF_4 \longrightarrow SiF_4 + CO_2 \tag{2.25}$$

Therefore, mainly high purity quartz glass components get applied in critical manufacturing steps. However, due to the direct decomposition pathway the lifetime of quartz components is very limited and novel long lasting materials are proposed. In this study especially Y_2O_3 and other yttrium containing compounds will be investigated due to their extremely promising etch resistance.

2.5.2 Plasma erosion of polycrystalline ceramics

Polycrystalline ceramics like yttria (Y_2O_3) and other yttrium based materials are getting increased attention as plasma resistant components inside etching chambers due to their high erosion stability in contact with fluorine based etching plasma [9, 10, 35]. In contrast to high purity quartz glasses which corrode under the formation of a gaseous phase, most polycrystalline ceramics form solid reaction products leading to etch rates which are of magnitudes lower compared to silica glass [7]. However, the application of plasma resistant ceramics leads to an increased risk of particle formation which can cause a detrimental failure during the processing of microelectronic components [3].

In literature, several processing routes are introduced to apply Y_2O_3 ceramics as a plasma resistant material for etching devices. First approaches developed Y_2O_3 coatings which are applied on low resistant alumina or quartz substrates to increase their erosion resistance in contact with reactive plasmas. Various coating techniques are described to deposit Y_2O_3 layers: Firstly, aerosol deposition layers (AD) got introduced by Iwasawa et al. using conventional quartz glass substrates. Jung et. al and Ashizawa et. al. reported on further developments of the AD deposition process by applying different rare earth oxides coatings and testing their erosion resistance [106, 107]. Additionally, various thermal spray techniques are applied to deposit Y_2O_3 coatings: The main focus was on high energy processes like atmospheric plasma spraying (APS) [108, 109], and suspension plasma spraying (SPS) techniques [110, 111].

In addition to plasma resistant coatings, bulk ceramic samples made from Y_2O_3 were investigated in literature. The preferred processing routes include conventional sintering [112] and a combination of conventional sintering and hot isostatic pressing [17]. However, the existence of residual porosity is the major drawback in sintered components due to the predominant plasma attack of surface pores [17, 113]. Additional investigations related to bulk ceramic components are the functionalization through an addition of conductive phases [114], the plasma resistance of alumina-yttria composites (YAG) [11] or the application of oxyfluorides as coating or bulk material [13, 14, 115].

Parallel to studies focused on the performance during under applied conditions, the general erosion behaviour of Y_2O_3 was investigated in several studies mainly using x-ray photoelectron spectroscopy (XPS) to characterize the formed reaction layer as well as its chemical bonding state. Initial studies of Kim et al. and Miwa et al.

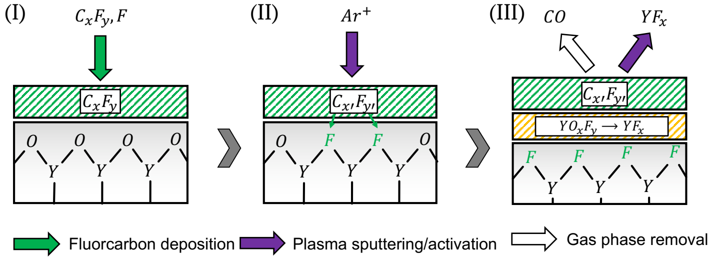

Fig. 2.15 Schematic sketch describing the surface erosion mechanism of Y_2O_3 in reactive fluorine based plasmas after Miwa et al. [8]. (I) The fluorocarbon radicals and molecules present in the plasma chamber from a thin polymer layer (Fig. 2.14) (II) Plasma activation breaks Y-O bonds and allows fluorination (III) A chemical gradient is forming at the surface consisting of yttrium oxyfluorides (YO_XF_Y) which is leading to the removal of surface material.

investigated the fluorination as well as chlorination of the near surface area after plasma exposure which they attributed mainly to the strong chemical interaction between the deposited reactive species from the plasma gas and the surface [8, 10]. Miwa et al. firstly described the mechanism controlling the fluorination process during the exposure of pure Y_2O_3 (Fig. 2.15): The surface reaction is mainly controlled by the fluorocarbon top layer which is deposited from the plasma gas, as described in Fig. 2.14. Under the impact of accelerated Ar ions from the plasma, surface reactions take place which break the Y-O bonds and facilitate the replacement of oxygen with fluorine atoms. The step by step formation of an oxyfluoride YO_XF_Y reaction layer is prone to material removal by physical sputtering and therefore increases the etch rate [12], enabling a more pronounced interaction of the reactive fluorine top layer with the substrate material. Further studies aiming to clarify the mechanism of erosion investigated the reaction layer formation in detail. A chemical gradient was observed, formed from the surface and proceeded to the bulk [9]. Overall, the erosion mechanism can be described as a physicochemical process, which is controlled by the chemical interaction between the substrate and plasma induced fluorocarbon depositions at the surface. The etch rate is therefore highly dependent on the sputtering properties of the halogenide compounds which form during the chemical corrosion. This correlation was clearly illustrated in sputter rate experiments on Al_2O_3, Y_2O_3 and their corresponding fluorides conducted by Kim et al. showing the higher etch resistance of YF_4 in comparison to AlF_3, which explains the low plasma etch resistivity of Al_2O_3 compared to yttrium based oxides [12].

A basic understanding of the active mechanisms which control the erosion behaviour of Y_2O_3 during the exposure to fluorine based plasma has been described in the literature. However, important material features which could have a major impact on the erosion mechanism have not been taken into consideration. Especially the influence of microstructural features like grain boundaries or the crystal orientation of the surface grains has not been investigated yet. Therefore, studying the erosion behaviour at the microscopic scale could be the key to understand and control problems like particle formation.

3 Experimental procedure and methodology

In the following chapter the experimental procedure ranging from powder characterization, sintering parameters to post processing characterization will be introduced. The structure of this section represents the processing and characterization steps given by the design of this study. First powder characterization methods and the applied processing routes are introduced being the basis to understand the ceramic processing used in this study. The experimental work conducted during this study is separated into two independent work packages focusing on the processing and doping of Y_2O_3 ceramics using FAST/SPS and the investigation of plasma-material interaction of polycrystalline Y_2O_3 with fluorine based etching plasmas. Finally, the major characterization techniques are shortly introduced, contributing to a better understanding of the subsequent discussion.

3.1 Powder characterization

The physical and chemical properties of ceramics powders are of fundamental importance for understanding the processing behaviour from powder to bulk. Several specific techniques were applied to determine the particle size, chemical impurities as well as crystallographic phases of the starting materials and processed powders.

Particle size measurement

The particle size distribution (PSD) was determined by laser granulometry using a laser diffraction method. A laser diffraction particle size analyser LA-950 (Horiba, Kyoto, Japan) with a wavelength of 405 nm was applied to determine the PSD as well as the cumulative values d_{10}, d_{50} and d_{90}. Particle size determination by light scattering is based on the relationship between the scattering angle and the particle sizes of the investigated powder.
When the laser beam hits a powder particle, a fraction of the incident beam gets scattered. Through the application of diffraction theory, the correlation between the variation of the scattered beam intensity and the particle size can be used to determine the PSD. In general, two diffraction theories are applied for the characterization of ceramic powders: The Fraunhofer and the Mie theory. The Fraunhofer theory is usually applied for larger particles where the particle size D is exceeding the wavelength of the used laser source λ. Nano-sized particles generally require the application of the more complex Mie theory to derive reasonable results from the diffraction data. In addition to the intensity, the size of the diffraction pattern

depends on the particle size, which can be described by:

$$\sin\theta = \frac{1,22 \cdot \lambda}{D} \tag{3.1}$$

where θ is the scattering angle, λ is the wavelength of the applied laser source and D is the particle size. In general, the range of particle sizes which can be investigated is larger when using the Mie theory. Here the measurement range is roughly 0.1 - 1000 μm, making it more practical for the investigation of ceramic powders. In practice only a small amount of powder is needed for the determination of the PSD. Usually the powder is dispersed in a liquid (deionized water or ethanol) and routed through a measurement cell where the laser light passes through the dilute suspension while the scattering is measured [36].

Additionally, the primary particle size and the powder morphology were determined by scanning and transmission electron microscopy techniques (SEM, TEM). Due to their manifold application in this work, the working principle, the material specific applications and the specific facilities will be introduced in detail in section 3.5.

Inductively coupled plasma mass spectroscopy

The amount of chemical trace elements in commercial and doped powders which are critical with respect to application in semiconductor etching environments was determined by inductively coupled plasma mass spectroscopy (ICP-MS). This technique is a fast and robust method to determine low amounts of impurities present in a powder sample. The powder sample is dissolved in HNO_3 at 100 °C and the solution is evaporated using a inductively coupled Ar plasma. This allows to separate all atoms of the investigated sample volume and induces a high ionization inside the plasma gas. The hereby generated gas mixture is fed into a mass spectrometer to determine the amount of trace elements. All powders were investigated by a ICP-MS 7900 analyser (Agilent Technologies, Santa Clara, USA) solving 20 mg of powder in water containing 2 ml of HNO_3. All measurements were repeated three times using the same solution to derive average impurity values.

X-ray diffraction

The phase composition and the possible presence of secondary phases, especially after milling and doping, was investigated by powder X-ray diffraction (XRD). This method is a versatile non-destructive material characterization technique which allows to determine the crystal structure, phase composition and lattice parameters by diffraction of X-rays on the lattice of crystalline materials. The elastic scattering of X-rays follows Bragg's law:

$$2d \cdot \sin\theta = n\lambda \tag{3.2}$$

Where d is the distance between adjacent lattice planes, θ is the incidence angle of the radiation, n is the order of diffraction and λ is the characteristic wavelength of the X-ray source [36, 116]. During the measurement, the X-ray source and the detector

are arranged in a 2θ set-up and the intensity of scattered radiation is determined dependent on the incident angle. The characteristic peaks are generated through constructive interference of the monochromatic X-ray beam at material specific diffraction angles. This means that the XRD pattern is material and phase specific and delivers a fingerprint of the crystal structure [116].
For the measurements, a semi automatic XRD system, D4 Endeavor (Bruker, Billerica, USA) using a Bragg-Brentano measurement geometry and Cu K_α radiation was applied. All measurements are conducted between $2\theta = 110 - 80°$ with a step size of 0.02 °. The characteristic XRD pattern derived from diffraction experiments was analysed and indexed using the software package HighScore Plus (Malvern Panalytical, Malvern, UK) and a ICDD database.

3.2 Starting materials and powder processing

Different commercial starting materials, milling and doping processes were applied for sample preparation. This section summarizes all starting materials and powder processing procedures.

Starting materials

For the investigation of the sintering behaviour and the plasma-material interaction, three types of commercial Y_2O_3 powders were used. Additionally to Y_2O_3, yttrium oxyfluoride (YOF) powders were considered to investigate the differences in the fluorination and erosion mechanisms active during plasma exposure. An overview of all starting materials in given in Tab. 3.1. For every powder, only one batch was purchased or provided by project partners to ensure reproducibility throughout all experiments.

Tab. 3.1 Overview of the starting powders used in this work.

Material	Manufacturer	Purity as indicated	Abbreviation	Applied in Sec.
Y_2O_3	KDL Resources	99.999 %	PJ2	4.1-4.3; 5.1-5.3
Y_2O_3	Treibacher AG	99.99 %	Treib	4.1; 4.2
Y_2O_3	H.C. Starck	99.99 %	H.C.	4.1; 4.2
YOF	American Elements	99.9 %	AE	5.3

Milling processes and doping

Throughout the study different powder processing techniques were applied to investigate the optimization potential of commercial powders for different sintering methods. Furthermore, different rare earth dopants were included into the powder materials to investigate their influence on microstructure development. Two kinds of milling processes were applied in this study, planetary milling and roll bench milling.

Planetary milling is a high energy milling process which uses a rotating set-up. This includes an Al_2O_3 milling crucible which rotates against the direction of the rotating base plate it is attached to, inducing high sheer energy to powder. For improving the milling process, ethanol was used as a liquid dispersant and 2 mm ZrO_2 balls act as the milling media. In section 4.1, the impact of optimized PSD on sintering of Y_2O_3 is investigated. Therefore, parameters used for planetary milling are summarized in Tab. 3.2.

Tab. 3.2 Overview on the processing parameters used in the milling study

t_m [min]	rpm [1/min]	$m_{Y_2O_3}$ [g]	$m_{Eth}[ml]$	m_{balls} [g]
30; 60; 90; 120	200	60	100	200

For comparison, low energy milling on a roll bench was applied to benchmark the elemental impurities induced by high energy planetary milling. In roll bench milling, the powder suspension (powder particles and ethanol) is blended with ZrO_2 balls in a polyethylene (PE) bottle and placed on two rotating cylinders. This setup decreases the total energy input during milling and leads to lower abrasive impurities but requires prolonged processing times. The rotation speed was fixed at 200 1/min and the processing time was set at 10h.

Roll bench milling was also applied to mix the dopants with PJ2 commercial powder. A liquid nitrate route was used consisting of two consecutive processing steps. First, the powder and the nitrate salts $La(NO_3)_3 \cdot 6\ H_2O$ (99,99% purity, Sigma Aldrich, USA) and $Gd(NO_3)_3 \cdot 6\ H_2O$ (99,99% purity, Sigma Aldrich, USA) were mixed with ethanol and ZrO_2 balls in a PE bottle. Y_2O_3 powders doped with 1 mol% La and 1 mol% Gd were prepared by milling with a rotation speed of 200 1/min for 24 h. After milling, the powders were dried for 24h at 80°C and afterwards calcined in air for 2h at 600 °C. As a reference material undoped Y_2O_3 powder was processed using the same procedure to achieve comparable powder properties.

3.3 Sintering experiments

The first part of experiments in this work is focused on the sintering of Y_2O_3 ceramic samples and components using conventional sintering and FAST/SPS. Therefore, the different experimental setups and parameters, which are used, are presented below.

Conventional sintering experiments

The conventional sintering behaviour of commercial and milled Y_2O_3 powders was investigated by free sintering and axial dilatometry. The free sintering experiments were conducted using commercial PJ2 powder in the as delivered state and with milled powders processed by planetary milling applying the parameters displayed in Tab. 3.2. Green compacts were produced by uniaxial pressing using 100 MPa for 1

min in a steel die. After removal from the pressing tool the samples were sintered at 1600 °C for 2 h in a commercial box furnace (Nabertherm GmbH, Lilienthal, Germany). For all experiments a heating and cooling rate of 5 K/min was used.
Additional to free sintering experiments, axial dilatometry was conducted to further investigate the impact of optimized PSD on the axial shrinkage during sintering. Therefore green bodies with a diameter of 8 mm were formed by uniaxial pressing of as delivered and planetary milled powders. The dilatometry measurements were carried out with an adjusted sintering cycle (1500 °C, 2h, ± 3 K/min) due to limitations of the experimental setup. A commercial axial dilatometer TMA 402 (Netzsch, Selb, Germany) was used, equipped with a SiC furnace (max Temp. 1550 °C, save operation up to 1500 °C), an inductive displacement measurement system and a force control system enabling to apply forces up to 3 N.

FAST/SPS sintering experiments

The major part of sintering experiments was conducted using field assisted sintering/spark plasma sintering technology (FAST/SPS). The experiments can be separated into three parts: (I) Processing of commercial powder using FAST/SPS (II) Upscaling and powder bed sintering experiments (III) Densification and grain growth of rare earth doped Y_2O_3 during FAST/SPS sintering.
All FAST/SPS experiments followed a general scheme. Graphite sheets (Mersen, Courbevoie, France) were placed between punches and die as well as between punches and powder. The powders are filled in the graphite die and are pre-pressed using a hydraulic hand press. The graphite die was wrapped with a graphite felt to reduce radiation losses and increase the thermal homogeneity in the tool.
First experiments targeted on the influence of sintering temperature on the processing of commercial Y_2O_3 powders. These experiments were conducted using a laboratory scale HP-D5 FAST/SPS facility (FCT Systeme, Rauenstein, Germany) and a 20 mm diameter graphite tool setup. All three commercially purchased Y_2O_3 powders (Tab. 3.1) were sintered at temperatures ranging from 1400 °C to 1600 °C. Other processing parameters are kept constant to conclude on the influence of sintering temperature on density and microstructural development. The applied processing parameters are summarized in Tab. 3.3. After sintering, the samples are recovered from the tool and residual graphite is removed by grinding.

Tab. 3.3 FAST/SPS parameters of commercial Y_2O_3 powders.

Sintering temperature [°C]	1400 - 1600 (50°C steps)
Dwell time [min]	10
Uniaxial pressure [MPa]	50
Heating rate [K/min]	100

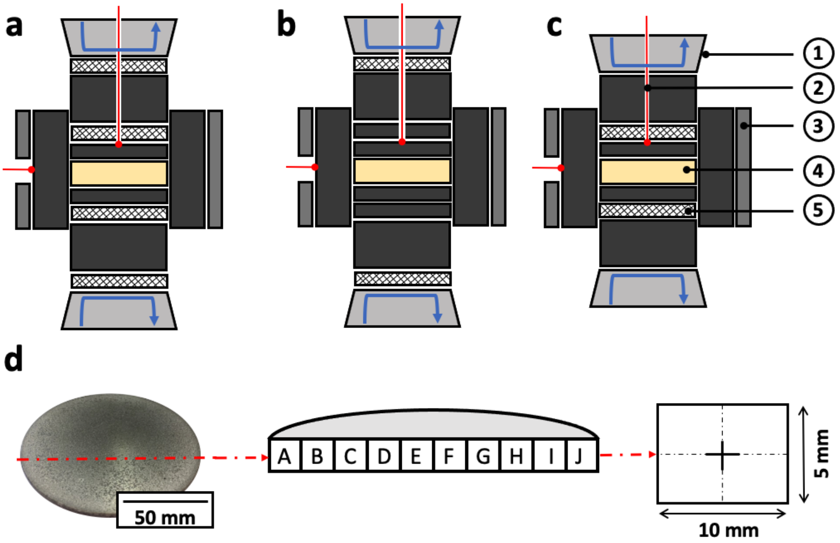

Fig. 3.1 FAST/SPS tool set-ups to investigate the influence of the CFC spacer position on the sintering of large scale yttria ceramics. (a) CFC spacers at all positions. (b) CFC spacers at the electrodes. (c) CFC spacer near to the sample. (d) Segmentation procedure for density and microstructure investigation. (1) Steel electrode, (2) Optical pyrometer, (3) Graphite felt insulation, (4) Sample, (5) CFC spacer.

For the sintering experiments aiming to investigate the challenges with respect to sample scale-up and the sintering of complex shaped parts, a hybrid FAST/SPS device H-HP-D25 (FCT Systeme, Rauenstein, Germany) was utilized. Two types of experiments were conducted. First, the influence of the CFC spacer position on the sintering of Y_2O_3 samples was examined. Therefore, a commercial 100 mm diameter graphite die (FCT Systeme, Rauenstein, Germany) was utilized. Carbon fibre reinforced graphite (CFC) spacers were placed at distinct positions of the tool set-up to optimize thermal distribution and reduce temperature gradients. This was achieved by exploiting the difference in thermal conductivity between CFC and graphite despite both having comparable electrical properties. Fig. 3.1 shows the three different tool set-ups which were benchmarked during this study. The two possible positions are either inside the pressing tool near the powder sample or as a thermal insulation directly in contact with the steel electrode. The CFC spacers were placed at both positions, only at the electrode position and only near the sample position. A set-up without any application of CFC spacers was also tested but the reference cycle was not possible due to high thermal losses leading to a security machine shutdown.

The FAST/SPS parameters used in this investigation were a sintering temperature of 1400 °C, a uniaxial pressure of 30 MPa, a heating rate of 25 K/min and a dwell time of 30 min. The reduction of uniaxial pressure from 50 MPa used in preliminary

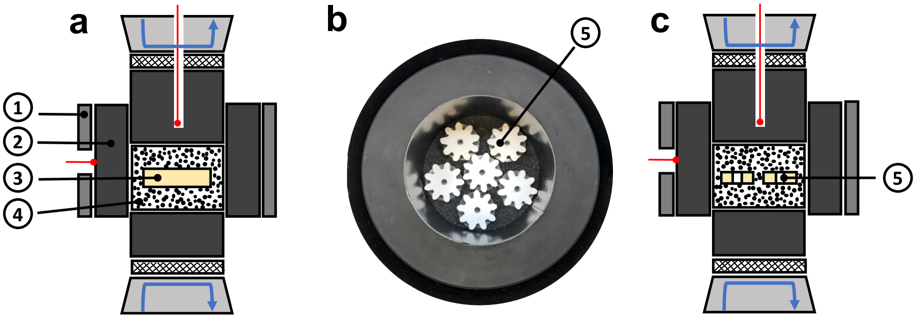

Fig. 3.2 FAST/SPS tool set-ups to investigate graphite powder bed sintering of simple and complex geometries. (a) Tool setup used for preliminary sintering experiments with a pellet shaped sample geometry (b) Top view image of the arrangement of gear-shaped Y_2O_3 samples inside a 100 mm graphite tool (c) Tool setup used for the powder bed sintering of complex shaped samples. (1) Graphite felt insulation (2) Graphite pressing tool (3) Ceramic green body (4) Graphite powder bed (5) Complex shaped Y_2O_3 sample.

experiments to 30 MPa was caused by the limited hydraulic force of 250 kN available in the H-HP-D25 facility. A slow heating rate was applied to reduce strong thermal gradients and to achieve the heating rate with respect to the maximum heating power of 60 kW in the FAST/SPS mode. After sintering the consolidated samples are cut following the procedure shown in Fig. 3.1 (d) for density and microstructure analysis at different positions along the diameter.

The second part of the scale-up study is focused on sintering of net-shaped Y_2O_3 parts vias FAST/SPS by using a graphite powder bed. Therefore, in a first step simple shapes (20 mm pellets) were selected to investigate the general possibility of powder bed sintering. Commercial Y_2O_3 powder (PJ2) was used because of the possibility to compare achieved densities and microstructures to results gathered during the conventional FAST/SPS sintering of this powder. The powder bed consists of a coarse graphite powder (Alfa Aesar, Haverhill, USA, -20+100 mesh, 99.9%) to prevent a sintering of the graphite powder. Preliminary experiments were conducted using the H-HP-D25 facility with a 45 mm graphite die that was filled with a defined graphite bed (Fig. 3.2 (a)) and a Y_2O_3 green body (5g; 20 mm; 100 MPa; 1 min; uni-axially dry pressed) was included. Both sintering temperature and applied pressure were varied during the consolidation process (1400 °C; 1500 °C; 1600 °C) and (20 MPa, 50 MPa). All other parameters were kept constant (10 min dwell; 100 K/min heating rate). After the removal from the powder bed the samples were ground to remove graphite residues and afterwards wire saw cut to investigate the microstructure along the diameter.

For the investigation of sintering of complex shaped yttria components a specifically designed pressing tool was manufactured in-house. This tool allows to press a gear shaped ceramic green body (diameter 30 mm) in one step without using any additional binder or pressing aids. In the following, gear shaped green bodies were pressed using a hydraulic hand press (10 kN, 1 min) for a direct processing inside a

100 mm FAST/SPS graphite die (Fig. 3.2 (b), processing six samples simultaneously). Part of the pressed green bodies were pre-sintered at 1400 °C for 2 h in a conventional box furnace to increase their mechanical stability.

For the FAST/SPS sintering, the 100 mm graphite tool was filled with two types of graphite powders: coarse graphite powder (-20+100 mesh) and fine graphite powder (-325 mesh) both from Alfa Aeser (Haverhill, USA). The sintering was conducted at 1500 °C, for 30 min with a uniaxial pressure of 30 MPa (pressure was applied at the beginning of the dwell time) and a heating rate of 50 K/min. A hybrid heating set-up using an additional induction coil was applied to enable the heating rates of up to 50 K/min. After sintering, the gear components were removed from the graphite bed and residual carbon was ground to enable density and microstructural investigations.

The last set of experiments was conducted during a research stay at the National Institute for Material Science in Tsukuba, Japan using a Japanese FAST/SPS sintering facility (SPS-1050, Fuji Electronic Industrial Co., Ltd., Saitama, Japan) and graphite tools with 20 mm diameter. Aim of this set of experiments was the investigation of the densification and grain growth of three types of powders: pure Y_2O_3, 1 mol% La doped Y_2O_3 and 1 mol% Gd doped Y_2O_3. Specific powder preparation is described in section 3.2.

Graphite sheets were used to separate the powder sample from the pressing tools, to improve heat transfer and to ease sample removal. All sintering cycles were done applying a uniaxial pressure of 50 MPa and a heating rate of 100 K/min. The sintering temperature was controlled by using a radial pyrometer focused on the outer surface of the die through a hole in the graphite felt. Two kinds of sintering experiments were conducted to investigate the densification behaviour as well as grain growth during the FAST/SPS sintering: I) The densification behaviour was investigated by varying the sintering temperature from 1100 °C to 1400 °C in 50 °C steps, while keeping the heating rate (100 K/min), dwell time (10 min) and applied pressure (50 MPa) constant. II) The grain growth behaviour during field assisted sintering was investigated by varying the dwell time at a sintering temperature of 1400 °C to 0, 30, 60 to 120 min. All other sintering parameters were kept constant. The sintering parameters for both experiments are summarized in Tab. 3.4.

Tab. 3.4 Overview on the sintering parameters applied during the investigation of densification and grain growth of rare earth doped Y_2O_3.

	Grain growth exp.	**Sintering trajectory exp.**
Sintering temperature [°C]	1400	1100 - 1400 (50 °C steps)
Dwell time [min]	0; 30; 60; 90; 120	10
Uniaxial pressure [MPa]	50	50
Heating rate [K/min]	100	100

Sample preparation and grain size determination

The microstructure characterization via microscopy requires a ceramographic preparation of the samples. Within this study, an optimized grinding and polishing procedure was developed to guarantee a reproducible surface quality. The steps of ceramographic preparation are summarized in Tab. 3.5. After removal from the sample holder and thorough cleaning, the polished samples were thermally etched at 1200 °C for 2h in a muffle furnace. The samples have to be packaged in a closed crucible to avoid surface contamination.

After thermal etching, microstructural features like grain boundaries became visible enabling measurement of grain sizes via optical methods coupled with image analysis. The average grain size was determined by the mean linear intercept method using the ASTM E112-13 norm "Standard Test Methods for Determining Average Grain Size". Random straight lines of a fixed length were drawn in the microstructure image and the number of grain boundary and triple point intersections are counted and divided by the length. This procedure was repeated for several images of the same sample until at least 250 grains were measured, resulting in the average grain size.

Tab. 3.5 Ceramographic preparation procedure for Y_2O_3 ceramics.

Step	**SiC Paper / polish**	**Time [min]**	**Rotation speed [1/min] / direction**	**Force [N]**
Plane grinding	P 240	1	150 / >>	10
Grinding	P 400	3	150 / >>	10
Grinding	P 800	3	150 / >>	10
Fine grinding	P 1200	5	150 / >>	10
Fine grinding	P 4000	5	150 / >>	10
Polishing	Soft cloth (MD-Nap) 3 µm diamond	5	150 / ><	10
Polishing	Soft cloth (MD-Nap) 1 µm diamond	5	150 / ><	10
Final polishing	Chem cloth (MD-Chem) OPS final	+1 only water	150 / ><	10

3.4 Plasma material interaction experiments

The second part of experiments aims on characterization and understanding of the plasma-material interaction of polycrystalline Y_2O_3 ceramics in fluorine based etching plasmas. An etching chamber with inductively coupled plasma (ICP) was used for all experiments. This experimental setup was designed and tested during the dissertation of M. Stamminger at the Ruhr University Bochum (RUB) and further details on the experimental setup can be found elsewhere [117].

A schematic sketch of the experimental setup is shown in Fig. 3.3 highlighting the main functionalities. The investigated samples were mounted in a custom made, water cooled sample holder (1) and the reactive plasma is ignited and maintained through an ICP generator on the bottom of the system (5). A DC bias voltage included in the chamber allows an exposure under physical sputtering conditions with a possible bias voltage up to 300 V.

Tab. 3.6 Plasma etching parameters applied in this study to investigate the fundamental behaviour (S), the influence of bias voltage (B) and the influence of plasma gas composition (C.)

	t_{etch} [min]	P_{ICP} [W]	U_b [V]	$Ar[cm^3/min]$	O_2 $[cm^3/min]$	$CF_4[cm^3/min]$
S150	120	600	150	5.0	0.3	1.0
B50	120	600	50	5.0	0.3	1.0
B300	120	600	300	5.0	0.3	1.0
C5	120	600	150	5.7	0.3	0.3
C10	120	600	150	5.4	0.3	0.6
C40	120	600	150	3.6	0.3	2.4
C80	120	600	150	1.2	0.3	4.8

A continuous gas flow controlled by flow regulators maintained a stable gas pressure and mixture during the plasma etching. The plasma gas consists of Ar, O_2 and CF_4 which were applied in different mixing ratios. All plasma parameters used in this study are summarized in Tab. 3.6. The standard parameter set (S150) was varied with respect to bias voltage (B50, B300) and plasma gas compositions (C5, C10, C40, C80).

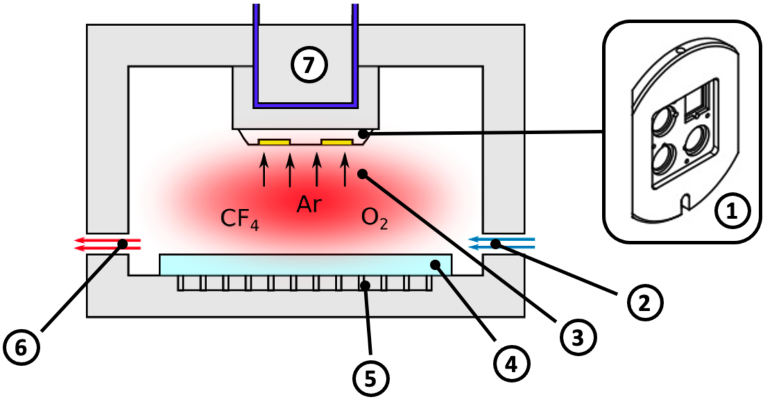

Fig. 3.3 Schematic sketch of the experimental ICP plasma etching chamber at the RUB. (1) Custom made sample holder for FAST/SPS sintered Y_2O_3 samples (2) Gas inlet (3) DC self-bias (4) Protection window (5) ICP-generator (6) Vacuum pump (7) Sample cooling system.

Tab. 3.7 Overview about all investigated plasma etched samples including the applied sintering procedure, plasma etching parameters and applied characterization techniques. (r) in brackets indicates that the re-localization technique was applied to enable a correlation between sample microstructure before and after exposure.

Type	**Etch parameters**	**Sintering parameters**	**Pre-characterization**	**Post-characterization**
Dense-polished	S150; B50; B300; C5; C10; C40; C80	1500 °C; 50 MPa; 10 min; 100 K/min	SEM (r) EBSD (r)	SEM (r) AFM (r) TEM SIMS
Porous-polished	S150; B50; B300	1150 °C; 50 MPa; 10 min; 100 K/min	—	SEM
Dense-ground (P120)	S150	1500 °C; 50 MPa; 10 min; 100 K/min	SEM	SEM
Dense-ground (P1200)	S150	1500 °C; 50 MPa; 10 min; 100 K/min	SEM	SEM
Y2O3/YOF (80/20 wt%)	S150	1500 °C; 50 MPa; 10 min; 100 K/min	SEM (r) EBSD (r)	SEM (r) EDS (r) AFM (r)

Different material and surface properties as well as processing variations were investigated to see their specific influence on sample erosion:

- Processing induced defects, including surface roughness, residual porosity and surface damage.
- Plasma processing parameter induced differences of sample erosion including the influence of bias voltage and plasma gas composition
- Comparison of the fluorination and erosion behaviour of Y_2O_3 and YOF on the microscopic scale

A broad variety of samples at different etching parameters was studied. All samples were sintered in a HP-D5 FAST/SPS device (FCT Systeme, Raunstein, Germany) using a 12mm graphite die. Before etching, the samples were prepared metallographically using the procedure shown in Tab. 3.5. Some of the samples were only ground using SiC papers to create different types of surface roughness. A complete overview on the sintering, applied plasma parameters and used pre-/post characterization techniques is shown in Tab. 3.7.

Additional to the standard investigation using scanning electron microscopy (SEM), transmission electron microscopy (TEM) and secondary ion mass spectroscopy (SIMS) at a random position of the sample, a straightforward re-localization technique was applied to correlate microstructural and material properties before and after plasma exposure. Characteristic cracks induced by hardness indents, which are applied by a commercial Vickers hardness testing machine (Duramin A-300, Struers, Denmark), were used as markers to relocate microstructural features after exposure. Using this method, a direct correlation between e.g. crystal orientation and erosion behaviour became possible, allowing an in-depth investigation of the active erosion mechanisms. A schematic sketch illustrating the re-localization procedure is displayed in Fig. 3.4.

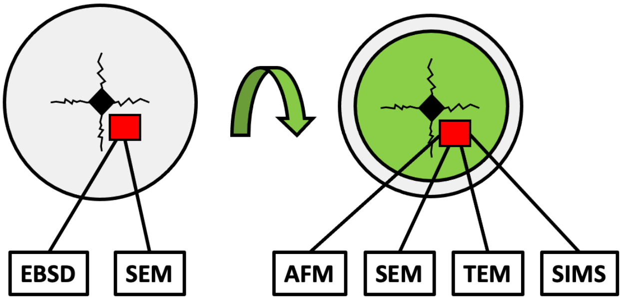

Fig. 3.4 Schematic sketch of the re-localization technique using Vickers hardness indents as markers and the applied characterization techniques before (left) and after plasma etching (right).

3.5 Microstructure and surface characterization techniques

In the last section of this chapter the characterization techniques which are applied to characterize microstructures and chemical composition are introduced. In particular, scanning electron microscopy, transmission electron microscopy, atomic force microscopy and secondary ion mass spectroscopy were used.

Scanning electron microscopy and electron backscatter diffraction

Electron microscopy and in particular scanning electron microscopy were used for different purposes in this study. This includes the analysis of grain size of sintered bulk compounds as well as the surface morphology after plasma exposure. The large variety of characterization methods offered by a electron microscopy includes high resolution surface topography imaging, elemental composition mappings and determination of crystalline orientation. A short summary of the working principle and the main investigation modes, which were used, is given below [118, 119].

Scanning electron microscopy (SEM) uses an electron beam, which is accelerated between a cathode and an anode and directed through an electron lens system to the sample. Compared to light microscopes significantly higher magnifications can be achieved due to the shorter wave length of the electrons. Information of

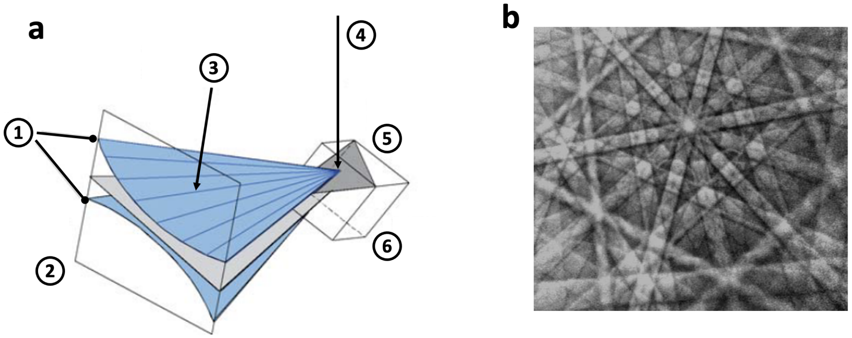

Fig. 3.5 Working principle and formation of orientation dependent Kikuchi patterns in electron backscatter diffraction (EBSD). (a) Schematic sketch showing the diffraction of the electron beam by a 70 °tilted sample and the formation of Kikuchi lines on a phosphorus screen. (1) Kikuchi lines (2) Phosphor screen (3) Cone of intense electrons (4) Electron beam (5) Diffracting plane (6) tilted specimen (b) Example image of a Kikuchi pattern of Cd at 20 kV. Graph and image taken from [118].

the sample surface is obtained by scanning the surface with the electron beam. Dependent on the interaction of the electrons with the sample material, different kinds of signals are generated and analysed by suitable detectors. In this work several characterization methods were applied, including: imaging using secondary electrons (SE), determination of chemical composition using energy dispersive X-ray spectroscopy (EDS), and investigations of the crystal orientation using electron backscatter diffraction (EBSD). Several material-electron interactions occur when the accelerated electron beam emitted from the cathode hit the sample: (I) Some of the electrons are elastically scattered by the sample atoms and re-emitted from the bulk. These electrons are called backscattered electrons (BSE). The intensity of backscattered electrons depends on the atomic number of the sample material, inducing a material specific contrast. Because in this work mainly highly pure single phase materials were investigated, this mode is of minor interest.

The second detection mode available in SEM is based on secondary electrons. This kind of electrons are inelastically scattered at the electron shell of sample atoms. Secondary electrons are generated near the sample surface and have a low interaction depth allowing high resolution imaging of topographic features. This is especially important for the investigation of the surface topography after plasma exposure.

When electrons with a sufficient accelerating voltage are used they are able to interact with the inner shell of the sample atoms, removing inner shell electrons from the atom. Recombination of the electrons lead to the emission of a characteristic X-ray radiation from the sample which is specific for distinct elements. The analysis of the characteristic X-ray spectrum is called energy dispersive X-ray spectroscopy (EDS). The characteristic EDS spectrum contains information about the elemental composition of the investigated area. However, due to high accelerating voltages, the

interaction volume of SEM-EDS is relatively large complicating sound conclusions on very localized phenomena.
The last and very versatile characterization tool is electron backscatter diffraction (EBSD), which can be used to obtain information about the crystallographic orientation, phase differences and the specific properties of grain boundaries character in crystalline solids. The Bragg scattering (Eq. 3.2) of high energy electrons (>15 keV) by a tilted (70°) sample produces diffraction bands which are visualized with the help of a phosphor screen. These phase and orientation specific diffraction patterns are called Kikuchi patterns. The basic working principle of a EBSD measurement setup is shown in Fig. 3.5. By scanning a pre-defined sample area with the electron beam, the crystal orientation in relation to the sample coordinate system can be detected and a phase and orientation map can be derived using related detection systems. In this work, orientation information gathered from EBSD measurements will be used to correlate the crystalline orientation of the surface with the erosion mechanisms active during plasma etching.

Transmission electron microscopy

Comparable to SEM, transmission electron microscopy (TEM) uses accelerated electrons which are interacting in various ways with the sample. However, in TEM electrons are transmitted through the specimen and analysed on the backside of the sample instead of analysing backscattered electrons. Therefore, the specimen has to undergo a specific preparation procedure which leads to electron transparency through the very thin, so-called TEM lamella. In general, focused ion beam (FIB) techniques are used to cut these thin lamella from the bulk of the sample. Additionally, accelerating voltages for TEM analysis are considerably higher than in conventional SEM devices (100- 300 keV), which enables the major part of the incident electrons pass through the sample. Furthermore, high electron energies lead to an increased imaging resolution due to the smaller wavelength of the electron beam [119, 120].
Additional instrumentation allows to scan the specimen moving the focused electron beam comparable as in SEM. This technique is called scanning transmission electron microscopy (STEM). This method is especially useful for spectroscopic investigations, allowing to map the chemical composition inside the sample which can facilitate a deeper understanding of physical and chemical processes at the atomic scale.
Out of the broad variety of detection methods, which are available in TEM and STEM, some specific techniques were applied in this work to investigate the physical structure and the chemical composition at the surface of plasma etched Y_2O_3 as well as at the grain boundaries of doped Y_2O_3.
Three types of TEM/STEM techniques were applied in cooperation with the GFE at the RWTH Aachen University as well as the ERC-2 of Forschungszentrum Jülich:

- Phase-contrast imaging (high-resolution TEM, HRTEM)
- Energy dispersive X-ray spectroscopy (STEM-EDS)
- High-angle annular dark-field imaging (HAADF)

Phase-contrast imaging offers the possibility to investigate materials at an atomic scale resolution by revealing the columns of aligned crystallographic domains in relation to the electron beam. In comparison to bright and dark field TEM imaging, phase-contrast imaging at a high resolution is enabled through the relation between the transmitted beam ("forward scattered" - not interfering with the crystal structure) and the diffracted beam. Both signals are needed to calculate the phase difference induced by diffraction of the electron beam. This method enables to directly observe the arrangement of the atoms in a very narrow area, which is the preferred TEM mode for the observation of structural defects in crystals. The main drawback of HRTEM is that it can not be coupled with spectroscopic investigations limiting its possibilities to draw conclusions on chemical distributions and gradients [120].
Therefore, STEM in combination with EDS methods were applied in this work to derive information on the chemical composition at the surface of plasma exposed Y_2O_3 samples and at the grain boundaries of rare earth doped Y_2O_3. Bright field STEM and HAADF imaging were used to investigate the samples at different resolutions. The detection of X-rays induced by electron scattering is comparable to the procedure applied in SEM. Due to the low thickness of specimens investigated by TEM the interaction cone usually generated in bulk samples becomes significantly smaller, increasing the spatial resolution which can be achieved in analytical TEM [120].
For the investigation of the chemical distribution at the atomic scale, HAADF imaging is combined with EDS signals. Compared to HRTEM, HAADF imaging is based on the detection of incoherent elastically scattered electrons. In incoherent scattering the sum of intensities of electrons, which are individually scattered at atoms from the specimen are used instead of the amplitudes of the wave function. This kind of data analysis avoids drawbacks like phase differences and electron beam interferences occurring in HRTEM and enables to interpret the gathered images more directly concerning atomic structures and defects. HAADF images are collected using the STEM mode and a annular dark-field detector which captures a large fraction of high angle diffracted electrons. This increases the resolution by an order of magnitude in comparison to a medium voltage field emission STEM, allowing to observe atomic columns in crystalline materials as sharply resolved structures [120].
The combination of HAADF imaging with spectroscopic techniques like EDS yields a very powerful tool for structure determination and chemical investigation at the atomic scale. In this study, the combination of HAADF and EDS was applied to understand the different influences of rare earth dopants on the structure and chemical composition at the grain boundaries in yttria.

Atomic force microscopy

For detailed investigation of the plasma-material interaction, an exact characterization of the surface topography before and after plasma exposure is necessarily required. For this purpose atomic force microscopy (AFM) is applied mainly on plasma etched samples after the exposure. AFM is a high resolution surface characterization technique, which utilizes the attractive and repulsive forces acting on a nano-sized tip, close to the sample surface. A schematic sketch of the basic working principle and general setup of an AFM is shown in Fig. 3.6 (a). For measuring the surface topography by AFM, the tip scans over a pre-selected area, while its position in z-direction is determined, generating a 3D map of the topography with a high z-resolution. When a nano-tip approaches the surface, different forces are acting on it (Fig. 3.6(b)): (I) If the distance between surface and tip is too big, no force is measurable (II) If the distance is in a distinct range an attractive force is acting on the tip (III) Very near the sample surface strong repulsive forces are active, pushing the tip away. The optimal working distance lies in the attractive regime but due to the existence of two slopes with comparable forces (point 1 and 2 in Fig. 3.6 (b)), the working distance has to be limited to one of them. The acting force bends the cantilever the tip is mounted on and this cantilever movement can be measured by a laser which is focused on the top of the cantilever and a photodiode which is used for the detection of changes of the laser signal. Additionally to the adjustment of the working distance, two different modes of operation are possible: Contact and non-contact mode. In contact mode the tip approaches the sample surface and the distance between sample and tip are kept constant during the whole measurement. This is enabled by monitoring the force acting on the tip and adjusting the distance of the sample while scanning. This mode is optimal for the investigation of small topographic changes on samples with high hardness like inorganic materials. Non-contact mode or tapping mode uses an oscillating cantilever with a higher working distance to the sample surface. The cantilever vibrates near its own free resonance frequency and a change of the acting force due to the sample topography will thus change its oscillating frequency. The feedback cycle controlling the measurement adjusts the tip-sample distance by regulating the vibration amplitude. This investigation mode is very variable with respect to the kind of samples. Its application ranges from soft, biological samples to hard materials with quite different topographies [121].

In this work, AFM will be applied in mainly tapping mode to correlate the microstructural changes of the surface topography of FAST/SPS sintered Y_2O_3 before and after plasma exposure.

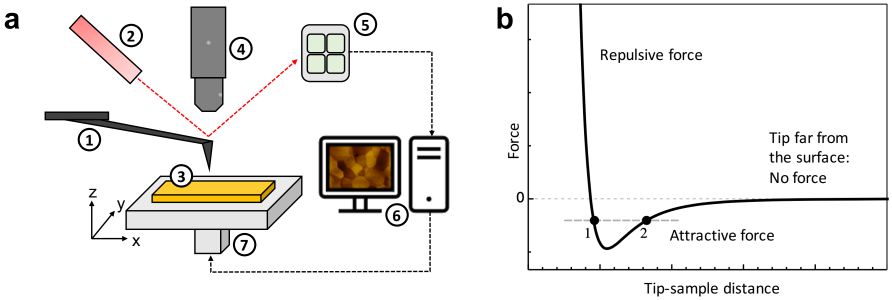

Fig. 3.6 Working principle of an atomic force microscope. (a) Schematic of a AFM setup (1) Cantilever with nano-tip (2) Laser (3) Sample (4) Light microscope (5) Photodiode (6) PC control and analysis. (b) Force distance relationship acting onto the nano-sized tip.

Secondary ion mass spectroscopy

Secondary ion mass spectroscopy (SIMS) is a surface analysis technique which can be applied to investigate the chemical composition of reaction layers, chemical gradients or thin films. Among the analytical tools available, it exhibits the highest detection sensitivity for all elements and a good depth resolution. Therefore, SIMS is an optimal tool to investigate the formation of chemical gradients at the surface of Y_2O_3 ceramics induced by the exposure to a fluorine based etching plasma [122].
In SIMS a primary ion beam (for example Ar^+, , Ga^+, Cs^+ or Bi^+) is used to remove material from the near surface region (1-2 monolayers) by physical sputtering. The secondary particles which are removed from the surface due to primary ion bombardment can be electrons, neutral atoms, ions and molecular fragments. During the measurement only charged ions are detectable and are analysed by mass spectroscopy. A specific elemental spectrum is measured, which enables to draw conclusions about the relative chemical composition [122].
In addition to the surface analysis, SIMS can be operated in a so-called "dual beam mode" enabling to investigate chemical gradients and diffusion profiles. Hereby, a second ion beam is used to remove the analysed surface layer after the sputtered ions were analysed by mass spectroscopy. The so called time-of-flight (TOF)-SIMS mode is used to characterize chemical gradients by measuring the elemental intensity dependent on the sputtering depth. In this work, TOF-SIMS (ION-TOF, Münster, Germany) is applied to investigate the chemical surface gradients induced by the exposure of Y_2O_3 ceramics to reactive etching plasmas [122].

4 Results and Discussion Part I: FAST/SPS of Y_2O_3

The following chapter primarily focuses on the processing of Y_2O_3 ceramics using conventional and field assisted sintering. At first, the influence of powder properties on conventional and field assisted sintering will be investigated highlighting the advantages of FAST/SPS. Subsequently, two major aspects which retard the application of FAST/SPS in industry are discussed: Upscaling of sample sizes from lab-scale to industrial dimensions and the need to consolidate samples with a more complex geometry overcoming the restrictions of densification of powders in a usual graphite tool. Lastly, rare earth doping as a promising option for microstructure control will be discussed in detail, focusing on the role of dopant segregation.

4.1 Conventional sintering of Y_2O_3

4.1.1 Powder characterization and material selection

A complete and thorough understanding of ceramic processing and sintering is based on the characterization of the starting material, in our case commercial Y_2O_3 powders. Therefore, the properties of three commercial powders were investigated focusing on morphology, primary particle size, particle size distribution and chemical impurities. Tab. 4.1 summarizes the particle properties measured by laser diffraction and BET. The powders from PJ2 and Treibacher show a comparable particle size distribution with a d_{50} value of around 5 μm. Compared to those results the Grade B powder from H.C. Starck shows a broader particle size distribution with a smaller d_{50} value of around 2 μm due to a significantly increased amount of fine particles. The detailed graphs in Fig. 4.1 show that PJ2 and Treibacher powders have a mono-modal size distribution while the H.C Starck powder exhibits a bimodal distribution, which hints on the existence of agglomerates that could not be broken up by ultrasonic

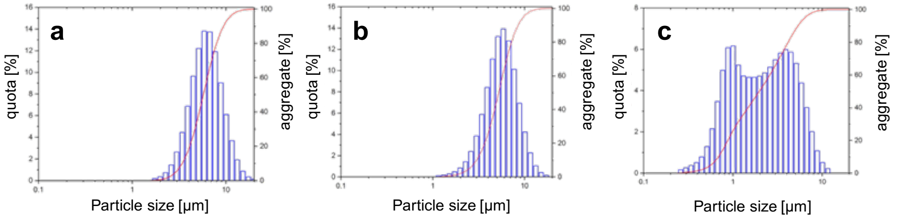

Fig. 4.1 Particle size distribution of commercial powders measured by laser granulometry. (a) PJ2. (b) Treibacher AG. (c) H.C. Starck Grade B.

Tab. 4.1 Particle size and the specific surface area of the starting powders measured by laser granulometry and BET.

Powder	d_{10} [μm]	d_{50} [μm]	d_{90} [μm]	SSA [cm^2/g]
PJ2	3.0	5.2	8.5	3.0
Treibacher	3.4	5.7	9.4	2.7
H.C. Stark	0.7	2.0	5.4	4.4

Tab. 4.2 Chemical impurities of the commercial powders investigated by inductively coupled plasma mass spectroscopy (ICP - MS). All values are displayed in mg/kg and the mean value (MV) and standard deviation (SD) are calculated from three separated measurements.

[mg/kg]	PJ2		Treibacher		H.C. Starck	
	MV	SD	MV	SD	MV	SD
Al	<2	—	<2	—	<2	—
Ca	20	10	19	8	16	7
Fe	<1	—	<1	—	<1	—
Zn	1.9	0.7	2.3	0.5	3	0.5
Sr	0.2	0.03	0.19	0.02	0.211	0.018
Zr	<0.1	—	<0.1	—	0.16	0.04
Ba	0.57	0.03	0.27	0.02	<0.08	—

treatment. The values of the specific surface area shown in Tab. 4.1 correlate to the measured particle sizes. The powders with smaller particle sizes exhibited a higher specific surface area. All commercial powders have a comparably coarse particle size distribution which is not optimized for conventional processing routes. Pressureless sintering of these raw materials is not possible without optimized powder processing. Nevertheless, sintering of these powders using FAST/SPS was expected to be possible without any further powder processing due to uniaxially applied pressure during sintering.

In addition, the amount of chemical impurities for selected elements (critical for an application in semiconductor manufacturing environments) was analyzed using ICP -MS. Tab. 4.2 shows the total amounts of elemental impurities, which is at a comparable level for all investigated powders. All powders considered in this study have a low amount of critical impurities with PJ2 powder showing the lowest values. For a deeper understanding of the applicability of the commercial powders, an investigation of the powder morphology, agglomeration state and the primary particle size is needed. Therefore, SEM investigations were conducted on all commercial powders. The results in Fig. 4.2 confirm the already presented data on particle sizes. The powders PJ2 and Treibacher exhibited a comparable particle morphology. Both powders have an angular shape and a narrow particle size distribution is visible. In comparison, powders supplied by H.C. Starck (grade B) have a smaller particle size, but similar morphology. However, the agglomerates measured by laser granulometry

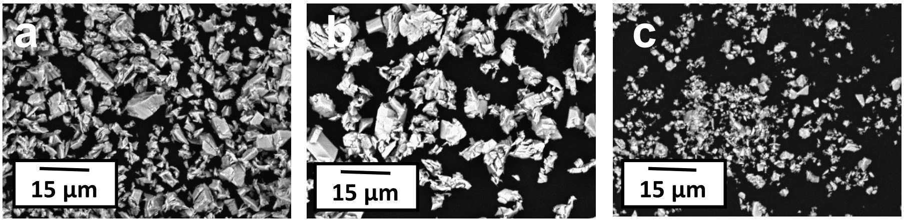

Fig. 4.2 SEM overview images of the powder morphology. (a) PJ2. (b) Treibacher AG. (c) H.C. Starck Grade B.

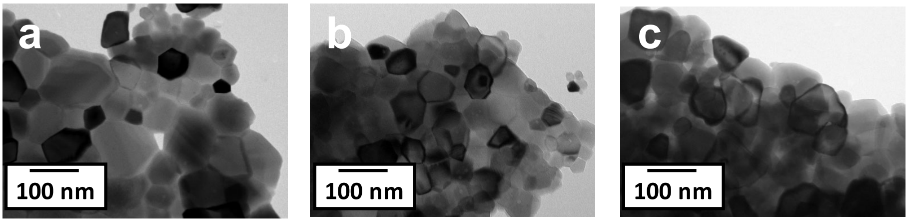

Fig. 4.3 Bright field TEM images of a powder agglomerate displaying the primary particles. (a) PJ2. (b) Treibacher AG. (c) H.C. Starck Grade B.

studies were not confirmed in SEM images. This could be caused by the SEM sample preparation. Pressured air is used to remove particles insufficiently attached to the sample holder to avoid contamination of the SEM chamber. The morphology of all powders was comparable, showing an angular shape indicating crushing or milling steps during powder synthesis.

Additionally, TEM investigations were conducted to visualize the primary particle size of all purchased powders. The bright field TEM images are displayed in Fig. 4.3. Quantitative measurements of the primary particles by image analysis reveals a primary particle size of 60 ± 17 nm for PJ2, 50 ± 17 nm for H.C. Starck and 35 ± 12 nm for Treibacher powders. The small differences in primary particle size were expected to have a negligible influence onto the sintering behaviour, which is mainly controlled by the agglomeration state. Here, the large difference between the size of agglomerates (secondary particles) was expected to significantly impact sintering behaviour and microstructural evolution.

The powder characterization revealed that two of the purchased commercial powders (PJ2 and Treibacher) had comparable properties concerning chemical composition, particle size and powder morphology. The Grade B powder distributed through H.C. Starck exhibited lower particle sizes and a bimodal size distribution of the agglomerates. Despite the differences in morphology, the primary particle size observed by bright field TEM imaging is comparable for all powders.

The powder selection was done with respect to and application in the semiconductor industry. Here, high chemical purity as well as homogenous particle size distribution leading to reproducible processes are the most important properties. Therefore, PJ2 powder was selected for all investigations, which focused on the plasma etching behaviour. This powder combined high chemical purity with intermediate particle sizes (which can be further optimized by e.g. milling) and a mono-modal distribution. In the following, the potential for conventional processing of PJ2 powder was optimized by additional milling steps. Additionally, direct sintering of all powders by FAST/SPS was investigated in detail.

4.1.2 Influence of powder processing on conventional sintering

Due to the angular powder morphology and large agglomerate sizes, conventional processing (uniaxial dry pressing and pressure-less sintering) did not lead to sufficient densification. Therefore, planetary milling was applied using different processing times from 30 to 120 min and ethanol as dispersant. The commercial powder PJ2 was selected to investigate the potential of powder pre-processing before conventional and FAST/SPS sintering. Changes of the particle morphology, size distribution, chemical purity and sintering behaviour are presented and discussed. The SEM images in Fig. 4.4 show the powder morphology after milling and drying. The unprocessed powder, shown in Fig. 4.4 (a) exhibits the coarse microstructure that was already described in the previous section. Already after 30 min milling improved particle morphology and size distribution were observed. With increase of milling time, the particle size was stepwise reduced but hard agglomerates were still visible after 30 and 60 min of milling. A further increase of processing time up to 90 min led to a homogenization of particle morphology and a mono-modal size distribution. After 120 minutes soft agglomerates were formed. In addition, fine particle sizes could have an additional influence on the dry pressing properties and the subsequent sintering step.

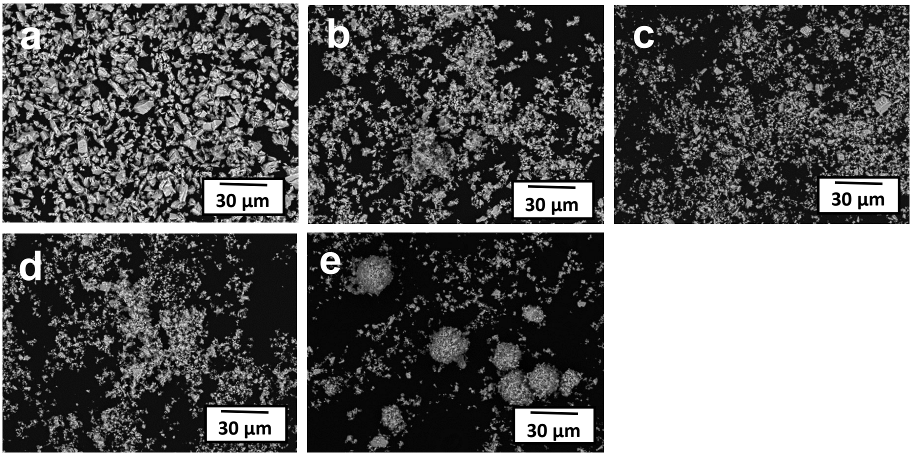

Fig. 4.4 SEM overview images of the powder morphology of PJ2 powders after milling in a planetary mill for different time durations. (a) unmilled. (b) 30 min. (c) 60 min. (d) 90 min. (e) 120 min.

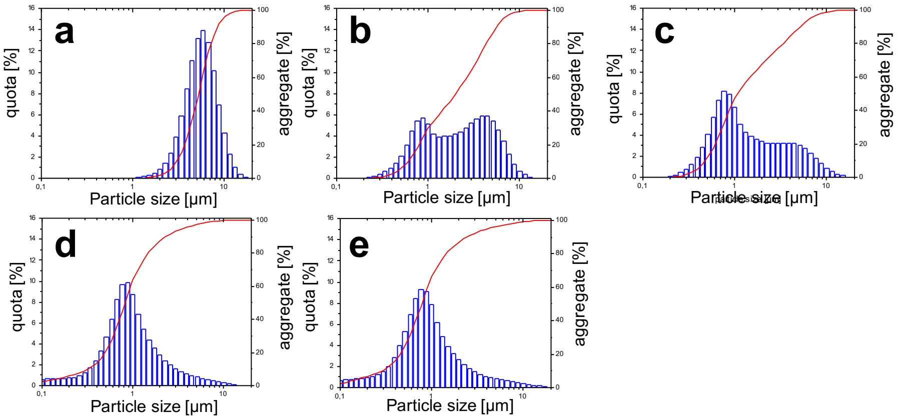

Fig. 4.5 Particle size distribution of PJ2 powders after milling in a planetary mill for different time durations measured by laser granulometry. (a) unmilled. (b) 30 min. (c) 60 min. (d) 90 min. (e) 120 min.

The particle size distribution was measured using laser granulometry directly on dispersed powders probed from the milling crucible. The results are displayed in Fig. 4.5 and confirm the observations by SEM. The particle sizes constantly decreased with increased milling time and the milling process saturated after 90 minutes. Further increase of the milling time did not further decrease the particle size and was therefore not useful for an optimized powder processing.

Fig. 4.5 clearly shows the change from a bimodal distribution after 30 and 60 minutes to a mono-modal distribution when exceeding 90 minutes. Short processing times are not sufficient to break all agglomerates and leave particles with increased sizes in the powder mixture.

The results reveal that the application of planetary milling offers a good possibility to optimize the particle morphology and size distribution of commercial coarse yttria powders. Besides the obvious advantages, abrasive wear from the crucibles and the milling media can occur during high energy milling. This can increase the chemical impurities of the powders especially with respect to elements used for crucibles and milling balls, like Al_2O_3 and ZrO_2. To quantify the effect of abrasive wear, XRD and ICP-MS was applied to measure the amount of impurities after planetary milling.

Fig. 4.6 shows the XRD diffraction pattern of PJ2 powder which was processed for 30 min in a planetary mill using Al_2O_3 crucibles and ZrO_2 milling balls. The diffraction pattern mainly shows the peaks of the cubic Y_2O_3 phase but minor additional peaks were visible (see inserted figure), which can not be related to cubic Y_2O_3. Obviously, high energy milling in ceramic crucibles clearly increased the amount of impurities through abrasive wear. Therefore, the amount of chemical impurities in the milled powder (30 min, 200 1/min) was determined by ICP-MS. Additionally to planetary milling, a low energy milling process, on a roll bench, was performed, which uses polyethylene (PE) bottles and strongly decreased milling energy. The results of the

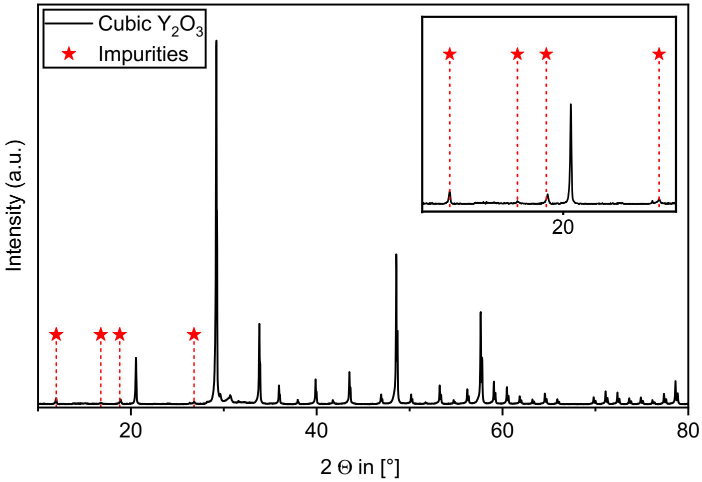

Fig. 4.6 XRD diffraction pattern of PJ2 powder after milling for 30 min in a planetary mill. The inserted figure shows the diffraction pattern at low angles in higher magnification indicating the presence of impurities.

chemical analysis (Tab. 4.3) revealed a small increase of Al, Ca and Fe and a strong increase of Zr in the powder. Especially the zirconia milling balls seemed to be prone to abrasive wear during high energy milling. A comparison of both milling processes showed only 6,05 mg/kg of Zr for powders milled by roll bench milling (RB), which is around 10% of the Zr impurities measured after planetary milling. Additionally, chemical impurities induced by abrasive wear of the milling crucible were prevented completely. A substitution by roll bench milling can significantly decrease the amount of chemical impurities but strongly increases the processing time to achieve comparable particle sizes.

To validate the impact of different processing times on the conventional and FAST/SPS, dilatometry and sintering experiments were performed. The processed powders were sintered conventionally (uniaxial pressing with 50 MPa for 1 min; sintering at 1600 °C, 2 h, 5 K/min) and by FAST/SPS (1300 °C, 50 MPa, 10 min, 100 K/min) to compare the impact of optimized powder morphology and particle sizes. Additionally axial dilatometry was used to measure the shrinkage during the sintering (1500 °C, 1 h, 5 K/min). The maximum operation temperature of the dilatometer of 1500 °C must be considered when comparing the results of conventional sintering and dilatometry. The green density was determined geometrically by measuring the diameter and thickness of green bodies as well as their mass before conventional sintering. As it was not possible to determine the green density of FAST/SPS samples prior to sintering, the dry pressing parameters were kept the same to apply the measured green density values for both methods. The relative density after sintering was determined using

Tab. 4.3 Chemical impurities of milled PJ2 powders investigated by ICP-MS. A low energy milling process (roll bench milling (RB)) was included for comparison. All values are displayed in mg/kg and the mean value (MV) and standard deviation (SD) are calculated from three separated measurements.

[mg/kg]	PJ2		PJ2 PM 30 min		PJ2 RB 10h	
	MV	SD	MV	SD	MV	SD
Al	<2	—	14	3	<3	—
Ca	20	10	18	7	<10	7
Fe	<1	—	13	4	<1	—
Zn	1,9	0,7	<4	—	5,7	0,2
Sr	0,2	0,03	7,9	0,8	0,21	0,05
Zr	<0,1	—	66	4	6,05	0,98
Ba	0,57	0,03	0,81	0,11	0,64	0,03

the Archimedes principle. Fig. 4.7 summarizes the density measurements of all sintering experiments conducted with planetary milled PJ2 powders depending on the milling time. The different powder processing conditions had no measurable effect in the case of the FAST/SPS samples. The applied pressure during sintering levelled the influence of bimodal particle size distribution and the presence of remaining coarser agglomerates. For demonstration of the influence of different milling durations on FAST/SPS sintering the uniaxial pressure and/or the sintering temperature has to be further reduced. The applied uniaxial pressure during FAST/SPS makes powder pre-processing steps like milling not necessary and the direct use of starting powders reduces the risk of processing induced impurity uptake. In contrast, samples which were conventionally sintered, show a strong dependency on the initial powder properties. Using the as purchased powder only 62 % relative density was achieved. The milling process improved the sintering stepwise to relative densities around 90 %. Milled powders which exhibited a bimodal particle size distribution (30-60 min) have a slightly increased sinterability compared to unprocessed powders but only milling durations of more than 90 min led to acceptable results.

Additionally to sintering experiments, dilatometry was applied to investigate the axial shrinkage of the as purchased and milled powders at 1500 °C. The densification curves are summarized in Fig. 4.7 (left) and confirm the results of the sintering study. Through a stepwise decrease and homogenization of particle sizes the sintering activity could be significantly increased. The densification starts at lower temperatures compared to unmilled powders and sustains longer, reaching higher relative densities. Moreover, powders milled for 120 min showed a slightly decreased densification which could be caused by the formation of soft agglomerates during powder pre-processing. The milling parameters have a major impact on the conventional sintering of Y_2O_3 and the optimal particle morphology and size has to be optimized. This can enable a high sintering activity leading to acceptable relative densities. Nevertheless, high quality requirements concerning the amount of residual porosity and chemical purity would require increased sintering temperatures or a changed atmosphere (vacuum,

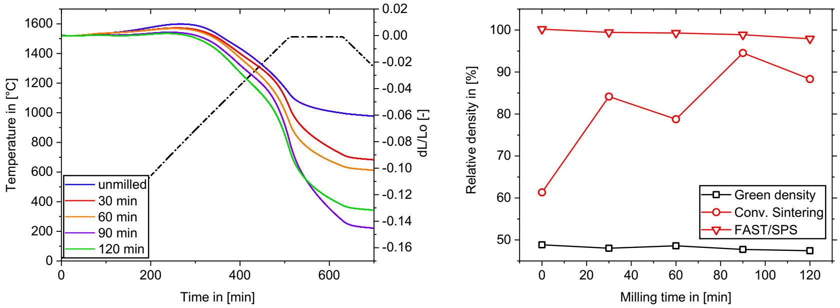

Fig. 4.7 Sintering behaviour of milled powders investigated by dilatometry (left, 1500 °C, 1 h, 5 K/min), conventional sintering (right, 1600 °C, 2 h, 5 K/min) and FAST/SPS (right, 1300 °C, 10 min, 100 K/min, 50 MPa).

Ar) [51, 52] or additional densification steps like hot isostatic pressing (HIP) to achieve high relative densities (> 99 %).
FAST/SPS sintering is less sensitive to the initial particle size due to the applied uniaxial pressure during sintering. Therefore, milling steps can be avoided using optimized FAST/SPS parameters. To further evaluate the potential of FAST/SPS, the different commercial powders will be densified at different sintering temperatures to investigate the potential for microstructure control by initial particle properties and sintering temperature.

4.2 FAST/SPS of commercial Y_2O_3 powders

In the following section, FAST/SPS of Y_2O_3 ceramics will be discussed emphasising several aspects: (I) The possibilities of microstructural control by applying different initial particle sizes and adjusting the sintering temperature (II) Challenges during the sample size scale-up and possibilities to manufacture complex shapes using FAST/SPS (III) Optimization of the microstructural evolution using cation doping with rare earth lanthanides. This combination of applied and fundamental research topics enable a comprehensive evaluation of the possibilities, which are offered by FAST/SPS aiming on producing Y_2O_3 ceramics for plasma etching applications.

4.2.1 Control of microstructure evolution using commercial powders

In the previous section it was demonstrated that in case of FAST/SPS processing, pre-processing of commercial powders did not have a major impact on the final relative density, when sintering temperatures at least 1300 °C are applied. As the general aim is to achieve Y_2O_3 ceramics with a relative density near the theoretical value, a sintering study in the temperature range from 1400 to 1600 °C (in 50 °C steps) was done to investigate the possibility to tune the microstructure by temperature. All other processing parameters were kept constant at 50 MPa uniaxial pressure, 100 K/min heating rate and a dwell time of 10 min. The three available commercial powders, which were characterized in section 4.1.1 were used as starting materials. Additionally, planetary milled PJ2 powder was densified to investigate possible effects of pre-processing on the microstructure. This will facilitate a correlation between the initial powder properties and the microstructure evolution at different sintering temperatures to guide the requirements for an optimized processing of Y_2O_3 ceramics using FAST/SPS.

The sintering temperature has only a minor effect on the final relative density as all of the investigated samples exhibit a relative density higher than 99 % over the investigated temperature range and therefore can be treated as sufficiently densified. The final relative density over all samples varied between 99.1 and 99.9 % and had an average value of 99.6 ± 0.2 %.

The average grain size and micro hardness depending on the sintering temperature is displayed in Fig. 4.8. For temperatures between 1400 and 1500 °C, the grain size distribution shows only a narrow deviation. Deviation increases at higher sintering temperatures. This is connected to the formation of larger grains through coalescence of small crystallites and subsequent grain growth. An influence of the powder properties is observable, as the starting powder with the smallest agglomerates (H.C. Starck Grade B) led to the smallest average grain sizes after sintering. Parts made of the other two, coarser powders had comparably larger grain sizes. Here, the main influencing factor controlling the microstructure development is not the primary crystallite size but the size of agglomerates. Similar observations have been made for ZnO by König et al. It was shown that agglomerated nano powders tend to densify their secondary agglomerates before macroscopic densification can be observed [123]. At the maximal sintering temperature of 1600 °C the grain size distribution is very broad due to the onset of abnormal grain growth.

The micro hardness values showed an inverse behaviour with respect ot the sintering

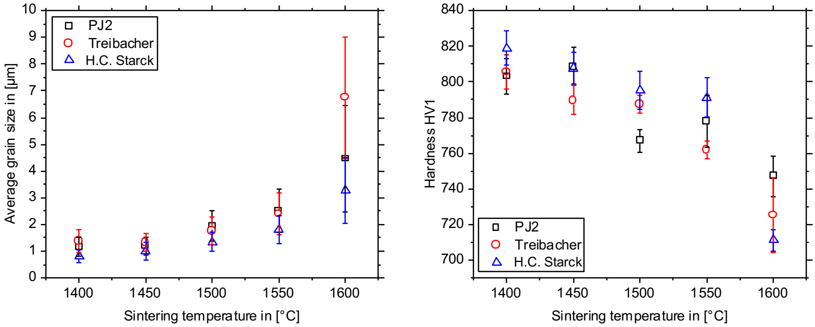

Fig. 4.8 Development of average grain size and micro hardness as a function of the sintering temperature during the FAST/SPS sintering of different commercial Y_2O_3 powders.

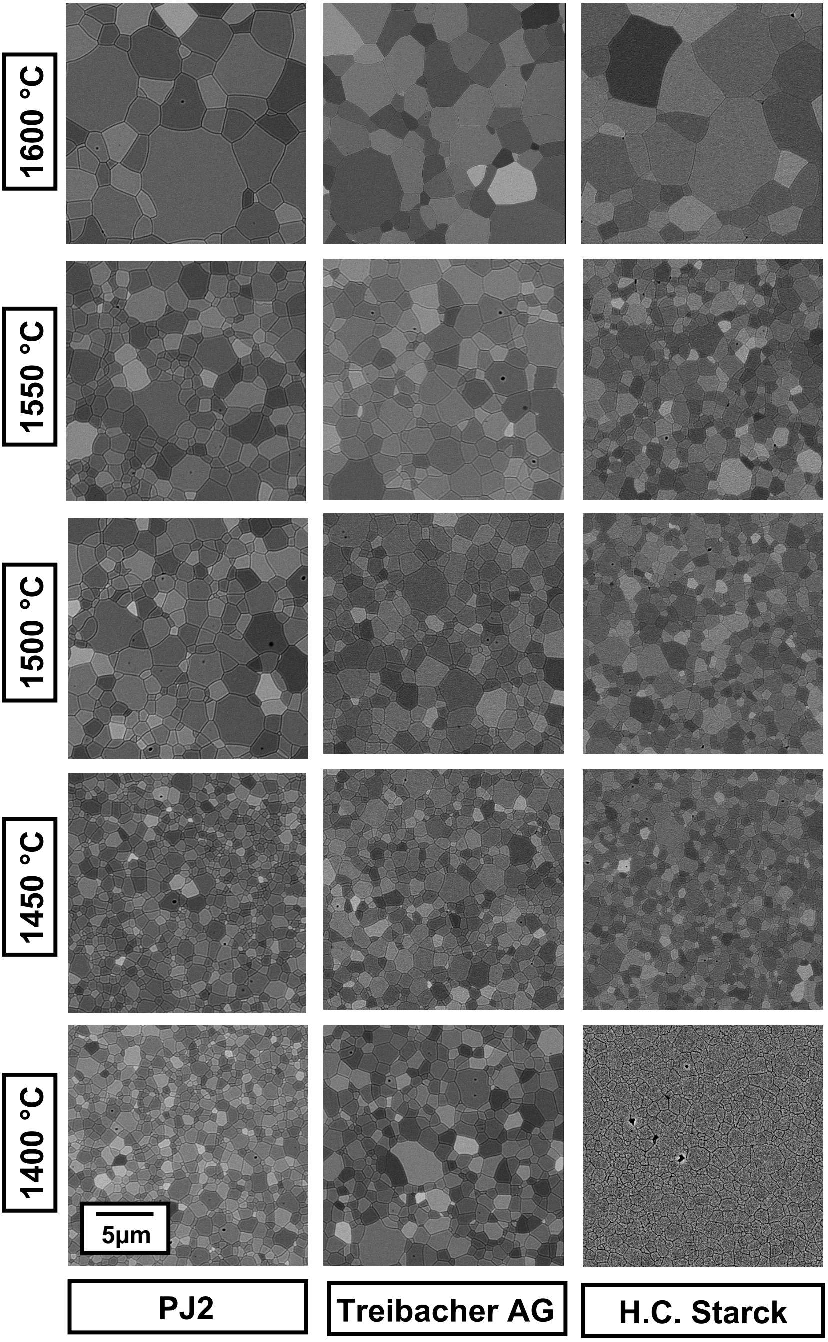

Fig. 4.9 Development of the microstructure as a function of the sintering temperature during the FAST/SPS sintering of different commercial Y_2O_3 powders.

temperature. Larger grain sizes at increased sintering temperatures resulted in a stepwise decrease of hardness. At low sintering temperatures, the hardness values are in the range of 800 - 820 HV1. With the clearly pronounced grain growth between 1550 - 1600 °C the hardness decreased to values around ca. 720 HV1. This behaviour can be related to the Hall-Petch-relationship which predicts the dependency of hardness and grain size as $H \sim 1/\sqrt{d}$ for materials with an average grain size larger than 1 μm [124].

Fig. 4.9 gives an overview of the microstructural development of all densified powders depending on the sintering temperature. All microstructures show a high relative density and only very small amounts of residual porosity. The pores were mainly intragranular as already detached from the grain boundaries during densification and isothermal dwell [36]. This observation hints on the high driving force for grain boundary migration, which enables pore detachment. Even though high relative densities were achieved, further densification is not possible due to the occurrence of mainly intragranular pores [37]. Steady and stepwise increase of grain sizes by adjusting the sintering temperature demonstrate the possibility of microstructure control during FAST/SPS. The size of powder agglomerates in the starting powders was found to be one of the main controlling factors to tune the final grain size. Nevertheless, FAST/SPS showed a high robustness with respect to the application of coarse powders, making this method advantageous compared to other sintering techniques without pressure. Control of the microstructure can be achieved, like in our case, through varying the sintering temperature, or through changes in the dwell time and the heating rate. The size of agglomerates had an additional effect on the final grain sizes. Increased agglomerate size led - at comparable primary particle size - to increased grain size.

Additionally to unprocessed powders, milled PJ2 powder, which was conventionally sintered in section 4.1.2 has been consolidated using FAST/SPS to investigate the

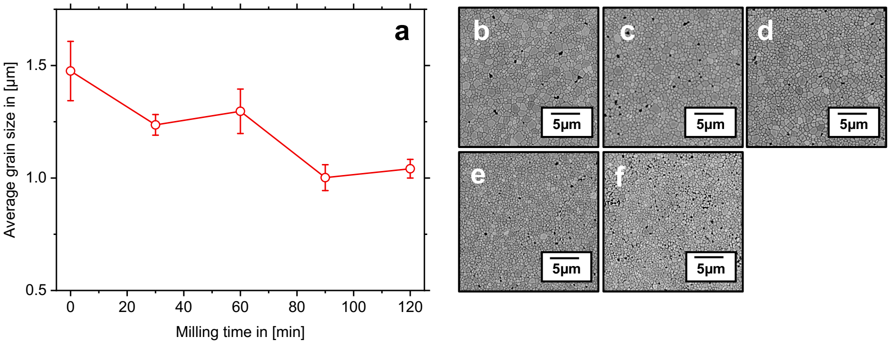

Fig. 4.10 Development of the average grain size and the microstructure of milled PJ2 powders after the FAST/SPS sintering at 1500 °C for 10 min under 50 MPa uniaxial pressure. (a) Average grain size development as a function of milling time (b-f) Corresponding SEM images showing the influence of milling on the final microstructure. All samples show a comparable relative density (see Fig. 4.7).

influence of initial agglomerate size on the final grain size development. The influence of the milling time on the average grain size after FAST/SPS sintering (1500 °C, 10 min, 50 MPa, 100 K/min) is displayed in Fig. 4.10. Increasing the milling time led to a stepwise decrease of average grain size, as agglomerates get broken up during the milling process. The decrease of the initial secondary particle sizes does not have a major impact on the sintered density but helps to manufacture components with finer microstructures.

4.2.2 Characteristics and challenges of sample scale up

The densification of unprocessed Y_2O_3 ceramic powders by FAST/SPS sintering is possible and yields highly dense samples with a low amount of residual porosity. This proves the applicability of this sintering method for small scale samples with a diameter of up to 20 mm. The main challenge for an application of FAST/SPS in industry is the processing of ceramic components having diameters much larger than 100 mm. Additionally, up to now FAST/SPS does not offer good possibilities to manufacture complex shapes exceeding the simple circular, square or ring shape. Few reports have shown the possibilities of industrial scale-up using FAST/SPS and mainly focused on metallic alloys (Ti, Steel), metal ceramic functionally graded materials (FGM, ZrO_2/Steel) and cermets (WC-Co) [125, 126, 127]. Industrial scale production of large scale ceramic components is not discussed in literature due to either confidentiality of industrial achievements or major problems occurring during scale-up like thermal gradients resulting in inhomogeneous densification and mechanical instabilities [84, 86, 128].

The direct processing of complex shapes via FAST/SPS is still a challenge hindering a more widespread application in industry. Recently, several approaches were proposed in literature to partly overcome some of these disadvantages. A sacrificial material and a deformed interface approach were demonstrated by Maniere et al., which enabled to sinter complex shapes but required a high extra effort for tool and green body preparation [129, 130]. Additionally, complex shaped tools were applied to manufacture single parts with an increased geometrical complexity [131, 132]. The most promising approach is to use an inert powder bed to manufacture complex shapes from pre-sintered bodies [133]. In this work, the influence of tool configuration on the sintering of samples with a diameter of 100 mm and a preliminary investigation of sintering complex shaped Y_2O_3 parts by FAST/SPS were investigated.

To investigate the influence of the position of CFC spacers in the tool setup during the processing of large scale Y_2O_3 samples, three different tool configurations were considered (Fig. 3.1). In all experiments, processing parameters were kept constant using a sintering temperature of 1400 °C, a uniaxial pressure of 30 MPa, a dwell time of 30 min and a heating rate of 25 K/min. After sintering, the samples were cut along the diameter and the local relative density and the average grain size was determined following the procedure described in section 3.3 (Fig. 3.1 (d)).

The development of the relative density dependent on the position of CFC spacers is displayed in Fig. 4.11. High relative densities above 97.0 % were achieved for all three tool setups. The most homogenous densification was achieved with CFC

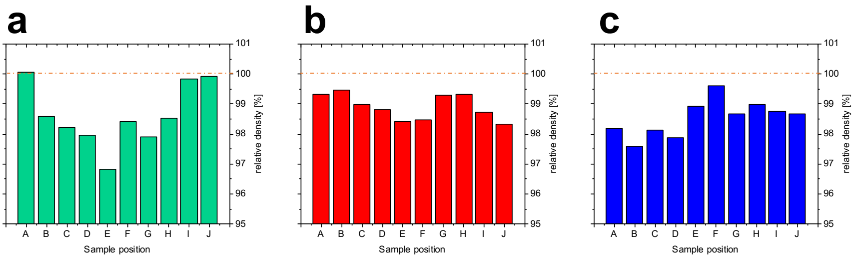

Fig. 4.11 Development of the relative density along the diameter of a FAST/SPS sintered Y_2O_3 sample (1400 °C; 30 min; 30 MPa; 25 K/min) with changed tool setups. (a) CFC spacers at both positions (b) CFC spacers at the electrode (c) CFC spacers near to the sample.

spacers located at the electrodes while omitting the second set of spacers near to the sample. Both other configurations, using CFC spacers at both positions and only near the sample led to slightly higher inhomogeneities in the density distribution. This could be caused by an inhomogeneous temperature distribution in the tool, which is less pronounced when the spacers are placed near to the electrodes. Additionally, the average grain size was determined and is displayed in Fig. 4.12 for all three tool configurations ((a) at both positions; (b) at the electrodes; (c) near the sample). The most homogeneous distribution of grain sizes was achieved using CFC spacers at both positions in the pressing tool. The average grain size is around 1,5 μm for all positions along the diameter. The two latter set-ups showed slightly increased inhomogeneity of the grain size distribution along the diameter with a minimum in the centre of the sample for the set-up applying CFC spacers at the electrode. The tool set-up using spacers only near the sample led to small average grain sizes which were inhomogeneously distributed. An overall comparison of densification and grain size development using three tool setups recommends the use of CFC spacers, which led to smaller and more homogeneous microstructures. Experiments without CFC spacers have been conducted but were not successful due to large thermal losses through the water cooled electrodes causing a safety shutdown of the sintering facility. The implementation of CFC spacers at both positions was found to

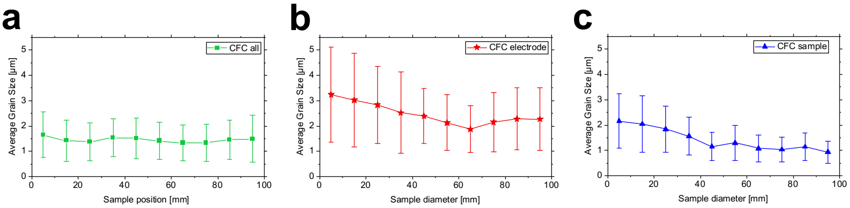

Fig. 4.12 Development of the average grain size along the diameter of a FAST/SPS sintered Y_2O_3 sample (1400 °C; 30 min; 30 MPa; 25 K/min) with changed tool setups. (a) CFC spacers at both positions (b) CFC spacers at the electrode (c) CFC spacers near the sample.

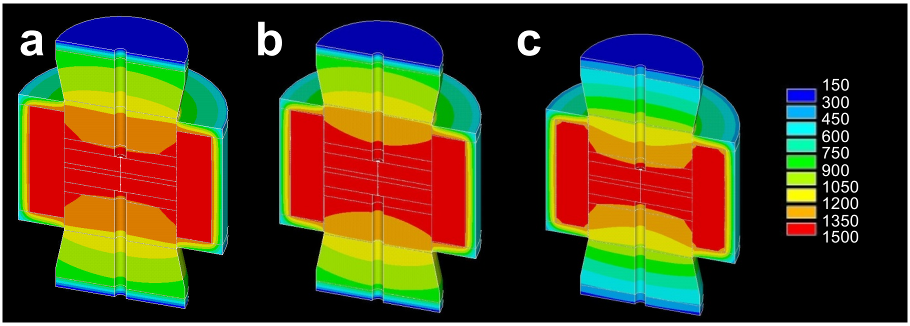

Fig. 4.13 FEM modelling results displaying the temperature distribution inside the tool setup using different CFC spacer configurations. The thermal field is displayed at the beginning of the dwell time at 1400 °C. (a) CFC spacers at both positions (b) CFC spacers at the electrode (c) CFC spacers near the sample.

be beneficial for the homogenisation of the microstructural development concerning relative density and average grain size. During the microstructure investigation only one sample was segmented for each setup limiting the conclusions to be drawn from the results. Processing influences like powder filling and pre pressure cycles could induce additional variations in sample quality.

Additional to the experimental investigation of sintered samples, the thermal distribution was calculated using finite element modelling to increase the understanding of the influence of CFC spacers on the processing of large scale. The modelling was performed by Prof. A. Laptev and details on the applied method can be found elsewhere [85, 86].

The modelling results are shown in Fig. 4.13 (overall thermal distribution tool setup) and Fig. 4.14 (thermal distribution in the sample). The calculations showed a temperature distribution, which is in accordance with the results of the microstructural investigation. Although being small, an influence of CFC spacer placement on the temperature distribution was observed. Removal of the CFC spacer near the sample (Fig. 4.13 (b)) led to the formation of a larger thermal gradient in the centre of the tool set-up. This hints on the importance of CFC spacers placed inside of the tool, concentrating the heat into the volume around of the sample. On the other hand, the removal of the spacer near the electrode (Fig. 4.13 (c)) caused an increased heat loss. However, modelling recommends to keep the CFC spacers near the electrodes due to the positive influence on the thermal field around the sample.

The temperature distribution inside the sample at the beginning of the dwell time showed similar results (Fig. 4.14). Removal of CFC spacers on both positions led to an increase of thermal gradients from the centre to the edge of the sample. Change of CFC spacer position was coupled with a clear increase of thermal gradients, which rise from 20 K (a) to 45 K (b) and 55 K (c).

The modelling results support the understanding of the observed microstructure development and help to improve thermal management through tool insulation and tool design. It is important to emphasize the necessity of applying CFC spacers

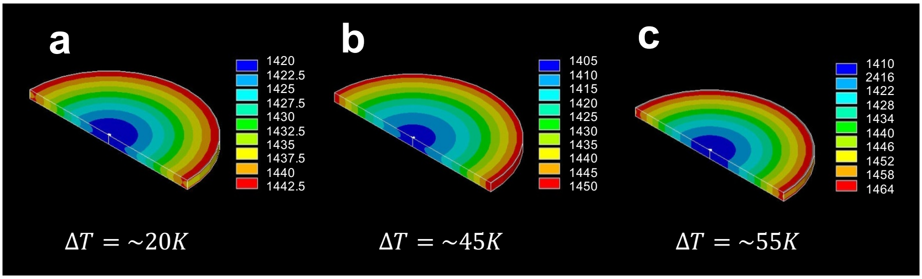

Fig. 4.14 FEM modelling results showing the thermal distribution inside the sample using different CFC spacer configurations. The thermal field is displayed at the beginning of the dwell time at 1400 °C. (a) CFC spacers at both positions (b) CFC spacers at the electrode (c) CFC spacers near the sample.

to achieve the aspired heating rates and sintering temperatures. An additional advantage of CFC spacers, especially in the vicinity of the sample, is the higher electrical resistivity compared to isostatic graphite, which helps to increase the heat dissipation through Joule heating.

In the second part of this section, the results of powder bed sintering of net-shaped Y_2O_3 parts by FAST/SPS are discussed and further development potential is highlighted. Results from the preliminary sintering study on powder bed FAST/SPS (PB-FAST/SPS) are summarized in Fig. 4.15, which shows the relative density, optical appearance and microstructure development of Y_2O_3 pellets which were sintered in a graphite powder bed (coarse graphite powder) with varying uniaxial pressure (20, 50 MPa) and temperatures ranging from 1400 to 1600 °C. The applied graphite powders were defined in detail in chapter 3.3. A strong influence of temperature and especially applied pressure on density became obvious. At low pressure of 20 MPa maximum density was around 88 %, while an increase of pressure to 50 MPa enabled densities ranging from 94 to 98 %. A direct adoption of the processing parameters from preliminary FAST/SPS sintering experiments to powder bed sintering with ceramic green bodies was possible, but decreased densification was observed for all cases. The probable reason is a changed temperature and pressure transfer from the graphite tools through the powder bed to the green body. Especially high heating rates are difficult to realize due to the slower heat conduction through the powder bed increasing thermal gradients. Fig. 4.15 (b) shows the visual appearance of sintered pellets that were ground after sintering to remove graphite residues. Images A to C show samples sintered with an uniaxial pressure of 20 MPa at 1400 to 1600 °C, while the images D to E display samples produced applying 50 MPa at 1400 to 1600 °C. Increased sintering temperatures at both pressures caused a stepwise colour change of the samples from white to red or dark green which can be associated with the diffusion of elemental impurities from the graphite powder into the sample body. This effect became stronger pronounced when higher sintering temperatures were applied. A subsequent thermal etching treatment at 1200 °C for 2 h in air resulted in a complete de-colouration of all samples appearing clear white afterwards.

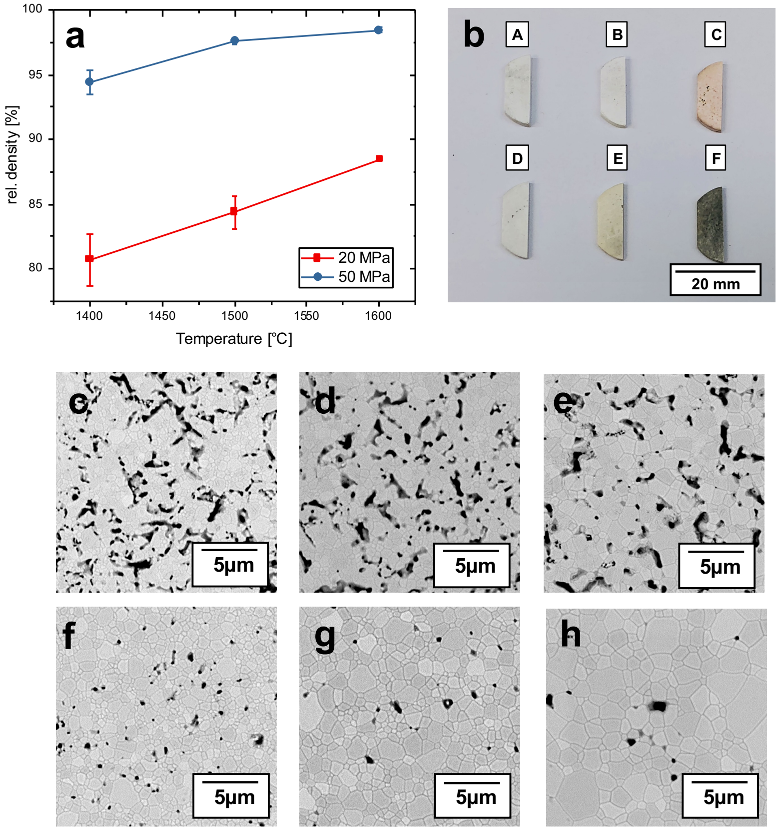

Fig. 4.15 Parameter study on FAST/SPS of Y_2O_3 green bodies in a graphite powder bed. (a) Relative density of sintered samples depending on uniaxial pressure (20 - 50 MPa) and sintering temperature (1400 - 1600 °C) (b) Visual appearance of samples after sintering in a powder bed. (top) 20 MPa (bottom) 50 MPa (c-h) SEM images of the microstructure using a uniaxial pressures of 20 MPa (top) and 50 MPa (bottom).

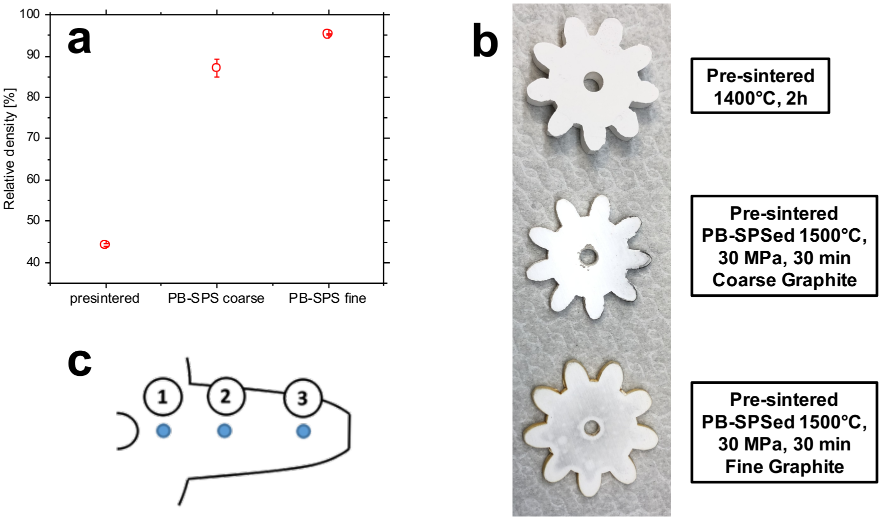

Fig. 4.16 Sintering of complex shaped Y_2O_3 components using graphite powder bed sintering. (a) Relative density of the sintered bodies measured by Archimedes principle. (b) Visual appearance of the gear-shaped Y_2O_3 samples before and after powder bed sintering. (c) Sample positions investigated by SEM.

Furthermore, all samples were stable and unbroken after the recovery and are only sectioned due to preparation purposes.

The reduced densification ability of PB-FAST/SPS compared to FAST/SPS was also confirmed by microstructural investigations shown in Fig. 4.15 (e-h). Samples sintered at low uniaxial pressure still showed a large amount of interconnected porosity, which could not be removed even at high sintering temperatures. However, increased temperatures slightly reduced the porosity and additionally contributed to grain coarsening. The increase of the applied pressure from 20 to 50 MPa led to a strong decrease of the residual porosity. However, densification was lower compared to samples which were directly processed in a graphite tool (Fig. 4.9). Nevertheless the preliminary results achieved with this simple sample geometry were promising and therefore directly transferred to the processing of complex shaped Y_2O_3 components. To investigate the upscaling potential and the possibilities to process complex shaped samples using FAST/SPS, a gear-shaped component was designed and used for demonstration of the technology. Gear shaped green bodies were dry pressed and either directly processed in graphite powder bed sintering or additionally pre-sintered at 1400 °C for 2h to enhance sample stability. All sintering experiments were conducted in a 100 mm graphite die using two types of graphite powder beds (fine and coarse graphite powders). The sintering cycle was fixed at 1500 °C, 30 MPa, 30 min dwell and a heating rate of 50 K/min to 1300 °C and 25 K/min from 1300 to 1500 °C. For additional experimental details, see section 3.3.

The post-characterization of gear-shaped Y_2O_3 samples included relative density measurement and microstructural investigation at different sample positions (Fig. 4.15 (c)). The relative density was determined by Archimedes method for all samples processed in one sintering cycle to determine the average achievable densification. An overview on the achieved relative densities and the visual appearance after sintering and post thermal treatment (1000 °C, 10 h) is given in Fig. 4.16. The pre-sintered Y_2O_3 gears exhibited a very low relative density of 44.2±0.2 % because of the non-optimized commercial PJ2 powders used during this study. Nevertheless, the sample stability during the powder bed sintering was strongly increased by adding this additional pre-sintering step before final consolidation inside the FAST/SPS device. Samples which were processed in a green state lacked mechanical stability and only a low amount of samples could be removed from the powder bed without mechanical damage after PB-FAST/SPS. Pre-sintered components could be densified to relative densities of 87.1±2.1 % and 95.3±0.1 % applying coarse and fine graphite powder beds.

The application of different powder beds had an additional influence on the sample geometry after PB-FAST/SPS (Fig. 4.16(b)).The application of a coarse powders bed triggered radial as well as axial shrinkage and therefore maintained the component geometry as defined by the pressing tool and the pre-sintered part (Fig. 4.16(b)). In contrast, samples densified in the fine graphite powder bed show almost no radial shrinkage and sample densification is dominated by axial compaction. This can be explained by the different behaviour of the applied graphite powders during PB-FAST/SPS. Coarse powders resisted any shrinkage up to high temperatures because of their large agglomerated morphology. This allowed to transfer the pressure in a quasi-isostatic way on the pre-sintered compacts, enabling the observed sample shrinkage in all directions. Finer graphite powder however tends to sinter in the applied processing window and therefore changes the pressure distribution inside the powder bed. Hereby, the densification in axial direction (z-direction) is favoured causing the observed inhomogeneous shrinkage of the sample. However, the increased density of the powder bed probably also increased the thermal conductivity of the tool setup leading to a better heat distribution in the powder bed. This could be one of the main reasons for the improved relative density which was observed when fine graphite powders were applied. Finally the local development of the microstructure during powder bed FAST/SPS sintering was investigated for three types of samples: directly processed green bodies and pre-sintered samples embedded in coarse and fine graphite powders. The microstructure was analysed at three different positions of the sample being located at the inner diameter near to the centre (Pos. 1) to the edge of the gear wheel (Pos. 3). An overview of the related SEM images is given in Fig. 4.17 showing polished cross-sections at three positions (Fig. 4.16 (c)).

The most homogeneous microstructure development was achieved by directly sintering pressed green bodies, which still exhibited a considerable amount of porosity but the densification was comparable at all three positions. However, the overall sample stability was not sufficient for conducting reproducible PB-FAST/SPS cycles, making a pre-sintering step necessary to improve processing stability. Due to the high level of agglomeration present in the used powders, the introduction of a pre-sintering stabilized the samples in a sufficient way. Nevertheless, the high pre-

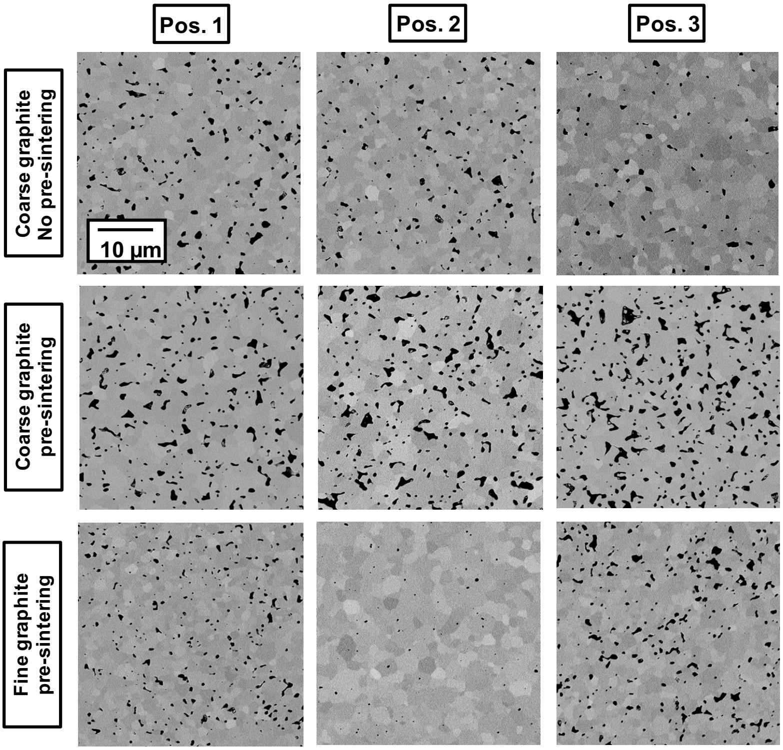

Fig. 4.17 SEM investigation of the microstructure at different positions along the diameter of the complex shape (Fig. 4.16 (c)).

sintering temperatures induced grain coarsening in the powder agglomerates, which reduced the overall driving force for densification during PB-FAST/SPS. This can be observed in the low densified sample, which was sintered in coarse graphite. At all positions, a high amount of porosity remained which made these processing parameters (powder properties, pre-sintering procedure, graphite powder bed and FAST/SPS sintering parameters) unsuitable for manufacturing complex components. However, the replacement of coarse graphite powders by finer graphite powders was coupled with an improvement of the microstructural development. Especially at the positions 1 and 3 residual porosity was still present, but in the bulk high local densities were reached. The changed densification behaviour of the fine graphite powder bed induced an improved thermal transfer from tool to the sintered bodies coupled with improved densification of the sample. The results achieved so far reveal a large optimization potential of PB-FAST/SPS.

4.3 FAST/SPS of rare earth doped Y_2O_3

As the last part of the processing optimization a doping strategy using rare earth oxides was developed to control densification and microstructural evolution during FAST/SPS processing. Rare earth oxides from the lanthanide group were used because the application of more effective divalent dopants like Ni^{2+} and Zn^{2+} is restricted by the requirements of the semiconductor industry regarding permissible impurities. As alternative dopants, the influence of 1 mol% doping with La^{3+} and Gd^{3+} on densification and grain growth will be discussed in detail. The sintering kinetics are correlated to the structural and chemical properties at the grain boundary using HAADF-STEM imaging and EDS mappings. Finally, a comparison of the grain boundary mobility determined from grain growth experiments with literature values allows a sound discussion of the impact and potential of lanthanide doping of Y_2O_3 ceramics.

4.3.1 Densification and grain growth behaviour

The densification behaviour of doped and undoped Y_2O_3 powders was investigated by measuring the development of relative density and average grain size at sintering temperatures in the range of 1100 to 1400 °C. Fig. 4.18 (left) shows the relative density, measured by the Archimedes method, as a function of the sintering temperature. The development of density led to two main conclusions:

(I) Below a sintering temperature of 1300 °C, the doping of 1 mol% La led to a clearly pronounced retarding effect on the densification. The densification curve was shifted to higher temperatures by roughly 100 °C and relative densities comparable to undoped Y_2O_3 were achieved later accordingly. At increased temperatures (1350 °C and 1400 °C), the retarding effect of La doping became neglectable as almost full density is achieved. The decelerating effect of 1 mol% La doping on the densification of Y_2O_3 was previously described by Yoshida et al. [66]. They associated the decreased densification with a changed ionic bonding strength around the dopant.

(II) Contrary to La, doping with Gd did not have any clear influence on the densification despite having almost comparable physical and chemical properties compared to La with respect to ionic radius and energy of the valence electron orbitals [66].

During FAST/SPS the rate-controlling sintering mechanism is grain boundary diffusion as reported for sub-micron Al_2O_3 with comparable processing parameters (heating rates between 10 and 150 K/min, uniaxial pressure from 15 to 50 MPa) [42, 43]. Supposing that these mechanisms were also active in the case of Y_2O_3, the present results reveal the different influence of La and Gd doping on the grain boundary diffusion during consolidation by FAST/SPS: As discussed below, this is probably caused by a different kind of segregation behaviour of La and Gd to the grain boundary.

The relationship between of average grain size and sintering temperature (Fig. 4.18 (right)) and relative density (Fig. 4.19) confirms the hypothesis stated above. Gd

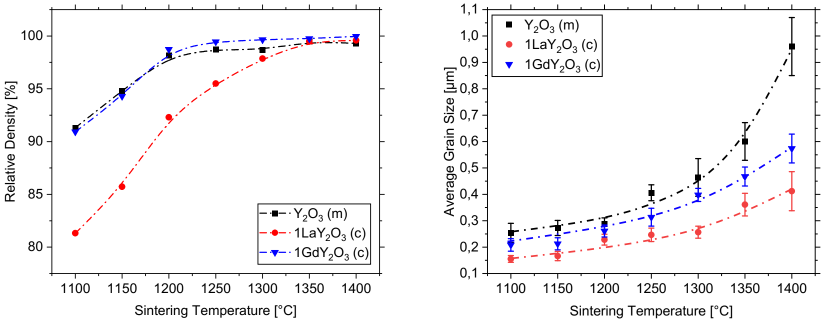

Fig. 4.18 (left) Development of the relative density as a function of the sintering temperature during FAST/SPS processing of doped and undoped Y_2O_3. (right) Development of the average grain size during FAST/SPS densification. The dwell time of 10 min and the applied pressure of 50 MPa are constant for all experiments. Lines are added to guide the eye.

as well as La doping decreases the grain growth during early stage sintering, which resulted in smaller grain sizes within the whole temperature range considered in this study. Doping of Y_2O_3 with La shows a larger deceleration effect on grain growth than doping with Gd. Additionally, the grain growth was decreased at increased sintering temperatures with La doping showing the clearest effect.

Furthermore, the development of average grain sizes depending on the relative density, the so called sintering trajectory, (Fig. 4.19) hints on two overlapping effects. For both dopants, a specific reduction of grain growth during sintering was observed. Doping Y_2O_3 with Gd does not change the densification behaviour compared to undoped Y_2O_3 (see Fig. 4.18), while doping with La clearly leads to a lowered sintering activity. This indicates a clear change of grain boundary diffusion rates as a characteristic of La doping.

For a better understanding of the influence of rare earth doping on the grain boundary mobility in Y_2O_3, grain growth experiments were performed by conducting FAST/SPS experiments with varying dwell times from 0 - 120 min at a maximum temperature of 1400 °C. The samples achieved almost full density already during the heating ramp allowing to investigate grain coarsening at dwell temperature. Fig. 4.20 shows the average grain size of doped and undoped Y_2O_3 as a function of the dwell time as well as a linear fitting of $G^2 - G_0^2$ to determine the grain boundary mobility from FAST/SPS experiments. The linear fit shown in Fig. 4.20 has a limited accuracy due to the non parabolic behaviour of grain growth observable during FAST/SPS. This could be caused by the occurrence of drag forces, which have a decelerating effect on grain boundary mobility leading to deviation from the ideal behaviour as described by the equation for parabolic grain growth. Nevertheless, mobility values were derived from this fit which will be discussed later with respect to the literature. Both dopants investigated in this study had a decelerating effect on grain growth caused by a decreased interface migration rate. In the same manner as the densification behaviour discussed before, the drag effect is more pronounced for La doping

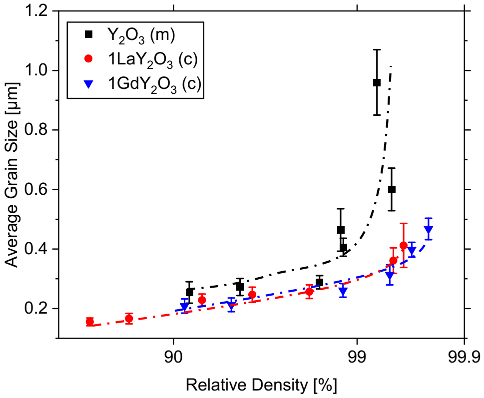

Fig. 4.19 Development of average grain size as a function of the relative density during FAST/SPS. The dwell time of 10 min and the applied pressure of 50 MPa were constant in all experiments. Lines are added to guide the eye.

than for Gd doping. These observations clearly indicate that in Y_2O_3 doped with rare earth cations a drag force acts on the grain boundary, which will be discussed in more detail later. Different TEM studies on doped Y_2O_3 ceramics showed the segregation of dopants to the vicinity of the grain boundary. This is an important observation to understand the behaviour of dopants and their influence on grain boundary motion during isothermal treatments at elevated temperatures. TEM-EDS measurements revealed that different isovalent as well as aliovalent dopants $(Al^{3+}, Ni^{2+}, Zn^{2+})$ in conventionally sintered Y_2O_3 segregate to the core of the grain boundary where they influence sintering and grain growth [65, 66].

As an additional quantification of the drag force caused by La doping, thermal treatments in a muffle furnace were conducted at 1400, 1500 and 1600 °C to measure grain growth and calculate the grain boundary mobility of undoped Y_2O_3 and 1 mol% LaY_2O_3 doped in air. Fig. 4.21 shows the grain boundary mobility calculated using equation 2.12 and microstructure SEM images before and after thermal annealing at 1500 °C for 10h. In the temperature regime between 1400 to 1600 °C, 1 mol% LaY_2O_3 revealed a decreased grain boundary mobility compared to pure Y_2O_3. These results additionally confirm the drag force induced by La doping, since they were observed in ambient atmosphere as well. Additionally, the activation energy was derived from the slope of the linear fit. The activation energy for pure Y_2O_3 is comparable to other studies investigating FAST/SPS sintering of Y_2O_3 [19, 93]. However, activation energy values determined on conventional sintered Y_2O_3 samples were reported to be in the range between 340 – 399 kJ/mol [57, 134]. Even though the grain growth factor was determined in air, the processing techniques utilized for densification seems to have an impact on the activation energy. Furthermore, the introduction of La led to an increase of the activation energy. This could be connected to dopant segregation to the grain boundary, which retards the diffusion of yttrium cations

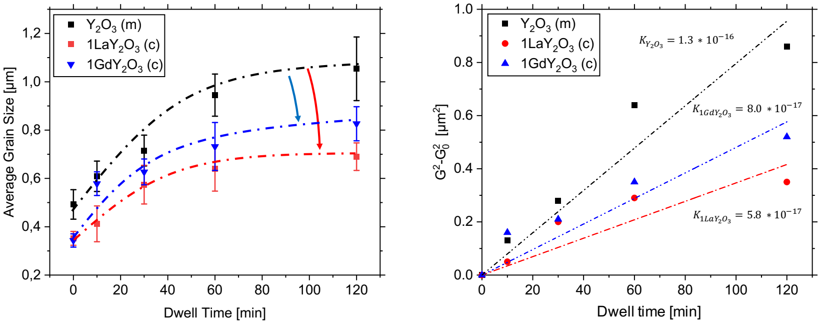

Fig. 4.20 Grain growth behaviour of pure and doped Y_2O_3 during FAST/SPS sintering at 1400 °C. (left) Development of the average grain size dependent on the dwell time at 1400 °C. Lines are added to guide the eye. (right) Linear fitting of the grain growth assuming $n = 2$. The grain growth constant K is derived from the slope of the linear fit.

perpendicular to the interface.

Additionally, Fig. 4.21 shows microstructure images of undoped and La doped Y_2O_3 after complete consolidation using FAST/SPS at 1400 °C (a, c) and after thermal annealing in a muffle furnace in ambient air at 1500 °C for 10 h. Before the annealing process, both samples showed a comparable fine-grained homogeneous microstructure with an average grain size of 0.61±0.06 μm for Y_2O_3 and 0.57±0.07 μm for 1 mol% LaY_2O_3. The selected samples were processed using differing dwell times to balance the different grain growth rates active during during densification (see Fig. 4.20). After the thermal treatment at 1500 °C in air, the microstructure of undoped Y_2O_3 (Fig. 4.21(b)) revealed a significant amount of grain growth. In comparison, 1 mol% LaY_2O_3 still contained some of its initial fine grains, clearly indicating a decelerated grain growth (Fig. 4.21(d)).

In addition to smaller grain sizes, a large amount of intergranular porosity was observed in 1 mol% LaY_2O_3 while undoped Y_2O_3 exhibited only intragranular porosity, similar to the sintering study on commercial powders (Fig. 4.9). Lower grain boundary mobilities during the holding time, which are generated by the solute drag effect of La doping, obviously suppressed the detachment of pores from the grain boundary. Keeping the pores at the grain boundaries is essential when aiming on a complete removal of residual pores during the final stage of sintering. The complete elimination of intragranular porosity only through the means of lattice diffusion is almost impossible because of slow diffusion paths. Therefore, pinning pores at the grains boundary is a good approach for the removal of residual pores through grain boundary diffusion in the final stage of sintering. Combined with optimized sintering parameters, solute drag induced by La doping can be utilized to remove residual porosity even when high sintering temperatures and long dwell times are applied. This doping strategy could be advantageously used to further improve the resistance of Y_2O_3 ceramics during plasma etching because of the predominant material removal of residual pores [17, 113].

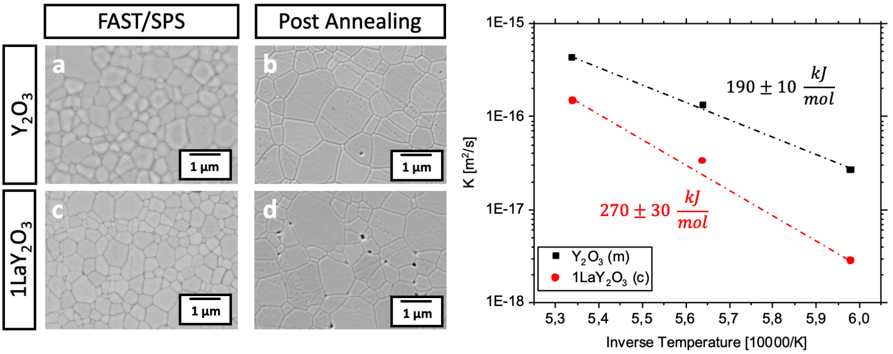

Fig. 4.21 Grain growth of pre-densified pure and La doped Y_2O_3 in air. (left) SEM images of the microstructure before and after thermal annealing at 1500 °C for 10h. (right) grain growth constant K for temperatures from 1400 °C to 1600 °C displayed in an Arrhenius plot.

4.3.2 Grain boundary structure and chemistry

For a deeper insight into the mechanisms controlling densification and grain growth during FAST/SPS of La and Gd doped Y_2O_3, a characterization of the grain boundary structure and chemistry at the atomic scale was necessary. Hence, STEM and STEM-EDS measurements of grain boundaries in pure Y_2O_3, 1 mol% LaY_2O_3 and 1 mol% GdY_2O_3 were conducted. The TEM lamellae were taken from samples sintered by FAST/SPS at 1400 °C, under an uniaxial pressure of 50 MPa, with a heating rate of 100 K/min and a dwell time of 120 min. Fig. 4.22 shows TEM-HAADF images which give an overview of selected grain boundaries for all three compositions. In undoped Y_2O_3, the grain boundary exhibited a clean interface with no observable structural defects (Fig. 8a). Both La and Gd doped Y_2O_3 showed dark secondary phases at the interface which could be either connected to interfacial porosity or

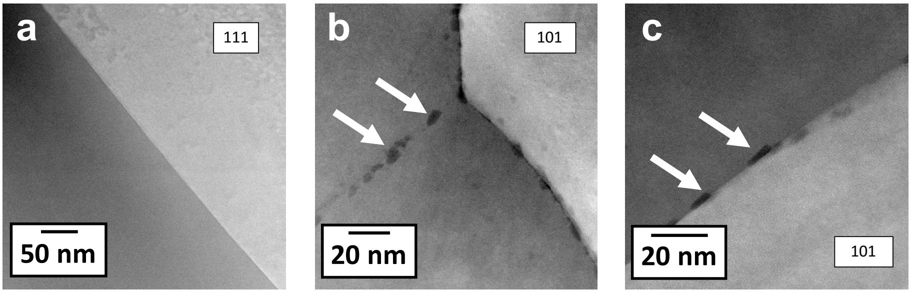

Fig. 4.22 Overview HAADF-STEM images showing grain boundaries in (a) pure Y_2O_3 (b) 1 mol% LaY_2O_3 (c) 1 mol% GdY_2O_3 sintered by FAST/SPS (1400 °C; 50 MPa; 120 min, 100K/min). Structural defects at the grain boundary are marked by arrows.

impurities induced by processing. The amount of defects was slightly higher in La doped Y_2O_3 compared to Gd doped Y_2O_3 but due to the small volume investigated by TEM, a statistically confirmed conclusion on distribution, shape and amount of grain boundary defects is hard to draw. However, interfacial defects were not present in the case of undoped Y_2O_3 indicating the influence of dopants on formation of these defects.

For better understanding of the chemical and structural changes which are induced by rare earth doping, high resolution imaging of the grain boundaries delivered useful insight. STEM measurements using high-angle annular dark field (HAADF) imaging were applied to collect information on the structure at atomic scale. Additionally, EDS mappings were used to investigate the chemical composition at the interface for all three compositions. Fig. 4.23 shows high resolution HAADF images of the atomic structure a the grain boundary of pure Y_2O_3 as well as corresponding EDS mappings. The STEM image in Fig. 4.23 (a) shows a highly ordered, defect free grain boundary without any additional secondary phases or amorphous films. Additionally, STEM-EDS mappings in Fig. 4.23 (b-c) proved the chemical purity and the structural integrity of the grain boundary in undoped Y_2O_3. The EDS intensity of Y and O is dependent on the orientation of the crystallographic planes, leading to slight differences between the adjacent grains. This orientation effect is more pronounced for larger atoms like Y, La and Gd (Fig. 8 b,c and Fig. 9 b,d) in comparison to O.

Afterwards, rare earth doped Y_2O_3 samples were investigated to correlate the sintering and grain growth kinetics with structural features and the chemical composition at the grain boundary. The samples were processed in the similar way as pure Y_2O_3 displayed in Fig. 4.23. High resolution HAADF images of the grain boundary in

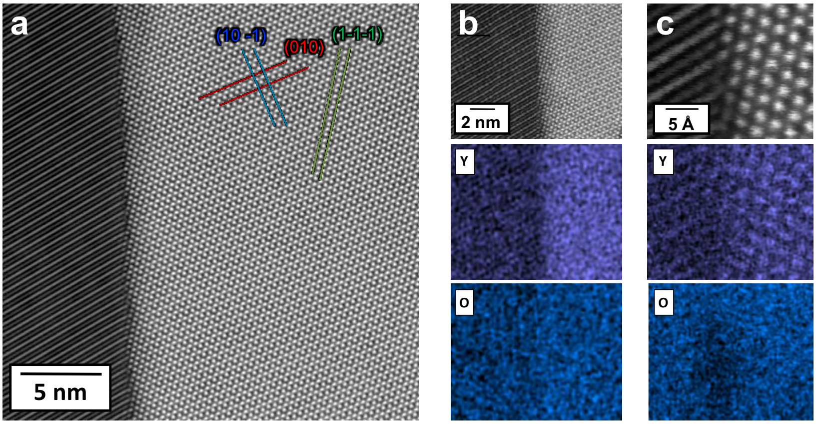

Fig. 4.23 High resolution HAADF-STEM images of pure Y_2O_3 sintered by FAST/SPS. (a) Clean grain boundary showing no structural defects or amorphous interfacial films. (b-c) Overview and detail STEM-EDS mappings showing the elemental distribution of Yttrium and Oxygen at the interface.

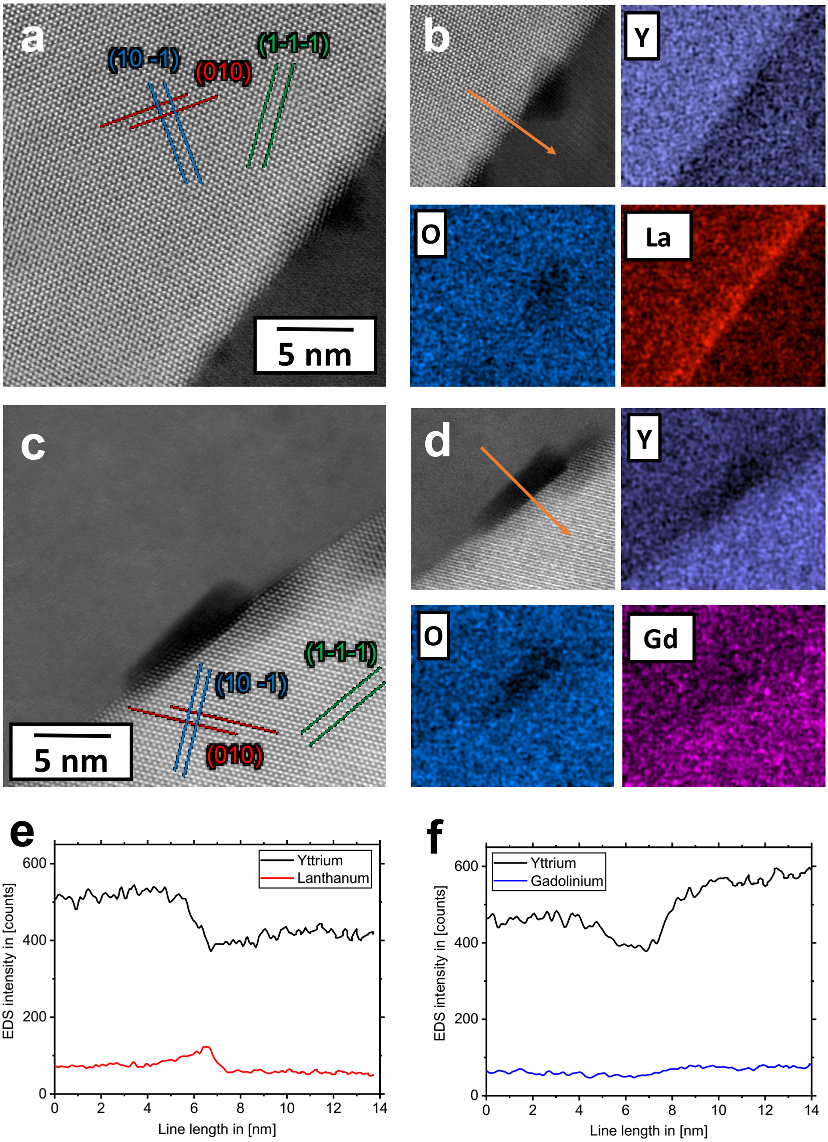

Fig. 4.24 High resolution HAADF-STEM images of La and Gd doped Y_2O_3 sintered by FAST/SPS. (a) HAADF image of a grain boundary in 1 mol% LaY_2O_3 showing no structural changes and intergranular films at the grain boundary. (b) EDS mapping displaying the chemical composition at the interface in 1 mol% LaY_2O_3. (c) HAADF image of a grain boundary in 1 mol% GdY_2O_3. (d) EDS mapping displaying the chemical composition at the interface in 1 mol% GdY_2O_3. (e) EDS line scan taken from the HAADF image in (b) highlighting La segregation at the grain boundary (e) EDS line scan taken from the HAADF image in (d) highlighting even Gd distribution across the grain boundary.

doped Y_2O_3 as well as corresponding STEM-EDS mappings are displayed in Fig. 4.24. Comparable to the grain boundaries in pure Y_2O_3, the interfaces in rare earth doped Y_2O_3 do not show any additional phases or amorphous films. However, in both cases characteristic defects became obvious, which were already visible in the STEM images in Fig. 4.22. Comparing the HAADF images with their corresponding EDS mappings indicated significantly reduced intensities of yttrium, oxygen and the dopant elements in these areas. This hints on the existence of interfacial nano-porosity at the grain boundary for both dopants. This kind of porosity induces an additional drag force on the grain boundary, retarding grain growth. Additionally, EDS investigations on 1 mol% LaY_2O_3 revealed a strong segregation of the dopant atoms in the vicinity of the grain boundary. This behaviour can be observed in the EDS mappings as well as in line scans shown in Fig. 4.24. A segregation of dopants to the grain boundaries in Y_2O_3 has been shown by several authors for different iso- and aliovalent cations (Mn^{2+}, Ni^{2+}) [64], Zn^{2+} [65], Al^{3+} [66]).

The comparison of EDS mappings of La and Gd doped Y_2O_3 further indicates the strong difference in cation solubility in the host lattice. The EDS intensity of Gd (Fig. 4.24(d)) revealed a homogenous distribution in the vicinity of the grain boundary with no observable segregation. Similar observation could be made for line scans, which reveal the pronounced segregation of La atoms. One main factor controlling and influencing the densification and grain growth behaviour during FAST/SPS observed in grain growth experiments (Fig.4.18) seems to be the tendency of distinct dopants like La to segregate in the vicinity of the grain boundary. A homogeneous solution in the host lattice as observed for Gd atoms did not significantly influence the densification behaviour. In contrast, La atoms strongly segregated at the grain boundary inducing a solute drag force and therefore retarding grain growth and densification.

The combination of cation specific segregation behaviour and formation of nano-

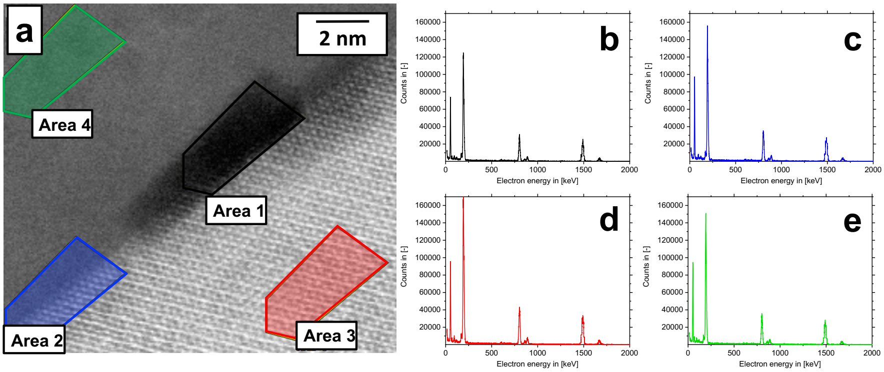

Fig. 4.25 STEM-EDS investigation on a nano pore in 1 mol% GdY_2O_3. (a) HAADF image showing a nano pore at the grain boundary in 1 mol% GdY_2O_3. Areas of interest are highlighted with different colours. The EDS spectra are extracted at the nano pore (b), a clean grain boundary (c) and the adjacent gains (d, e).

porosity during sintering seem to be the main influencing factors controlling the densification and grain growth. Especially the occurrence of nano-porosity at the grain boundaries was not expected because of the long dwell times used for the fabrication of the investigated samples. Pores of this size store a high amount of interfacial energy, which makes them thermodynamically unstable at high temperatures. Therefore, additional STEM-EDS measurements were conducted, comparing the spectroscopic intensity of different areas at the grain boundary, in the adjacent grains and in a nano pore to investigate the presence of secondary phases which could stabilize pores of this size (Fig. 4.25). The extracted EDS spectra revealed no secondary phases and a completely similar peak pattern. A comparison of maximal intensity counts indicated that the EDS scan in the nano pore showed the lowest intensity of all investigated areas. These results support the assumption that nano-pores are present in rare earth doped Y_2O_3 sintered by FAST/SPS. However, the interfacial porosity could be stabilized by the entrapment of a gaseous phase during processing, leading to an additional factor influencing the grain growth kinetics.

4.3.3 Impact of segregation on sintering and grain growth

Finally, the overall impact of dopant segregation and nano pore formation on processing and microstructure evolution will be discussed.

The main driving force for the occurrence of dopant segregation in ceramics is the decrease of Gibbs free energy [135]. Both electrostatic and elastic forces are contributing to the segregation induced by a mismatch in charge and size between the dopant species and the host lattice [53, 136, 137, 138, 139, 140]. Compared to aliovalent dopants where charge plays the dominant role, the size mismatch of isovalent dopants becomes the major factor controlling the segregation behaviour [141, 142]. In ceramics, this behaviour was clearly confirmed for TZP materials [70, 143, 144] and comparable results were shown by Yoshida et al. for Y_2O_3. In Yoshida's studies, cations with a large size difference showed the characteristic segregation (demonstrated for Ni^{2+}, Zn^{2+}, Mn^{2+} as well as for Al^{3+}, Ge^{3+}) [65, 66] and dopants whose size fits to the host lattice are able to be homogeneously solved in the crystal structure [65].

In the present work, cations have been selected which exhibit almost no size mismatch (Gd^{3+}, ionic radius: 0.094 nm) as well as cations with a size mismatch (La^{3+}, ionic radius: 0.106 nm) compared to the host lattice (Y^{3+}, ionic radius: 0.093 nm). Additionally, an applicability in semiconductor environments was taken into account. As expected, the low size mismatch of Gd cations to the host lattice led to a homogenous distribution which is also represented by the high solubility of Gd in Y_2O_3 (up to 100 % [145]).

Due to the size mismatch of La to Y, the overall solubility in the host lattice is low (7 mol% [146]) and this cation tends to segregate to the grain boundaries. This drastic change in the segregation behaviour caused by cation size mismatch is inducing several effects during sintering and grain growth.

The segregation of La cations to the grain boundary leads to solute drag force which is decelerating the grain growth in comparison to Gd doped yttria and the undoped reference material [50, 147]. Comparable observations have been made for zirconia, where doping with Ce^{4+}, which is isovalent and has no size mismatch, shows no interfacial segregation and leads to coarse microstructures, while doping with Y^{3+} (aliovalent with large size mismatch) leads to solute drag and small grain sizes [70, 143, 144, 148]. Comparable observations have been made in doped perovskites $SrTiO_3$ [149] and $BaTiO_3$ [150]. Additional to solute drag caused by dopant segregation, pores present at the grain boundary cause a reduction of grain boundary mobility. Possible formation mechanisms and the effect of pores will be discussed below.

The influence of cation segregation on the sintering behaviour is more complex. The densification during FAST/SPS is expected to be mainly controlled by grain boundary diffusion. In the case of La doping, grain boundary diffusion seems to be reduced, causing a lowered sintering activity [42, 43].

In metals, a decrease of the grain boundary self-diffusion due to segregation of dopants is well documented for several systems (Al, Mg, Ni) [151, 152, 153, 154, 155]. Comparable effects have been observed for ceramics like Al_2O_3 (Mg^{2+} segregation) [156, 157], $SrTiO_3$ (Fe^{3+} segregation) [149] and ZrO_2 (Y^{3+} segregation) [148] where segregated cations induced decreased grain boundary diffusion rates. The effect of doping on grain boundary diffusion in Y_2O_3 was studied in detail by Yoshida et al. showing that isovalent dopants with smaller ionic radii than the host lattice accelerated the sintering kinetics while larger cations decelerated the sintering. They investigated the segregation behaviour for several of the applied dopants (Zn^{2+}, Ni^{2+}, Mn^{3+}, Al^{3+}, Ge^{4+}) and observed comparable results like reported in this work. A general conclusion can be drawn with respect to the literature: The application of larger cations leads to a segregation which decelerates the diffusion along the gain boundary and therefore retards sintering.

A sound conclusion on the mechanism how larger dopant cations retard the diffusion along grain boundaries is difficult to draw. The change of the atomic structure at the grain boundary could lead to a more closely packed grain boundary narrowing down the pathway for diffusion. Additional explanations were proposed by Yoshida et at. emphasizing a changed chemical bonding at the grain boundary resulting in a need for higher temperatures to activate diffusion [66]. Overall it can be concluded that the segregation of La cations to the grain boundaries has two major consequences on the microstructural development in Y_2O_3. Grain boundary migration is decelerated by activating solute drag and the sintering activity is lowered by a reduced grain boundary diffusion.

Additional to the solute drag effect, the observed occurrence of nano porosity (Fig. 4.22 and Fig. 4.24) might induce further decelerating forces on the grain boundary mobility due to pore pinning effects. Despite the high driving force for further shrinkage pores of this size exhibit, long dwell times at high temperatures seem not remove these features. Therefore, additional to HAADF imaging, EDS spectra of the nano-porosity and the adjacent host lattice were compared, and no impurity phases could be detected, and the interfacial porosity revealed the lowest EDS intensity (Fig. 4.25). Additional to solid impurities, entrapped carbon oxides formed from carbon residuals, which are induced by evaporation from graphite papers and tools during the fast heating in the early stages of sintering could stabilize the porosity. The low diffusion rate through the lattice prevents gas removal from the closed porosity and leads to a stabilization against further pore shrinkage. This phenomena has been described for several ceramic material systems like Al_2O_3 [158, 159], ZrO_2 [158] and $MgAl_2O_4$ [160, 161] during hot pressing and FAST/SPS densification. The hereby generated nano-porosity is under high internal pressures which can have a detrimental effect on the mechanical properties. However, pure Y_2O_3 samples did not show the specific nano porosity. The doping process could introduce additional volatile species to the powder compact, which are trapped inside the microstructure during FAST/SPS consolidation. The nano porosity which is present in doped Y_2O_3 induces an additional decelerating force on the grain boundary migration during grain growth which is called pore drag [162, 163]. This effect was observed during the sintering by FAST/SPS (Fig. 4.20) as well as in thermal annealing experiments in air (Fig. 4.21). The combination of solute drag induced by dopant specific grain boundary segregation and pore drag lead to the stepwise decrease of grain boundary mobility.

The grain growth factor, which was measured and calculated on pure and doped Y_2O_3 in this work is summarized in Fig. 4.26) and compared to grain growth data from literature [57, 61, 65, 164, 165, 166]. Both grain growth factors calculated from grain growth experiments in air and derived from FAST/SPS experiments are considered. The grain growth factors calculated in this work are in accordance with

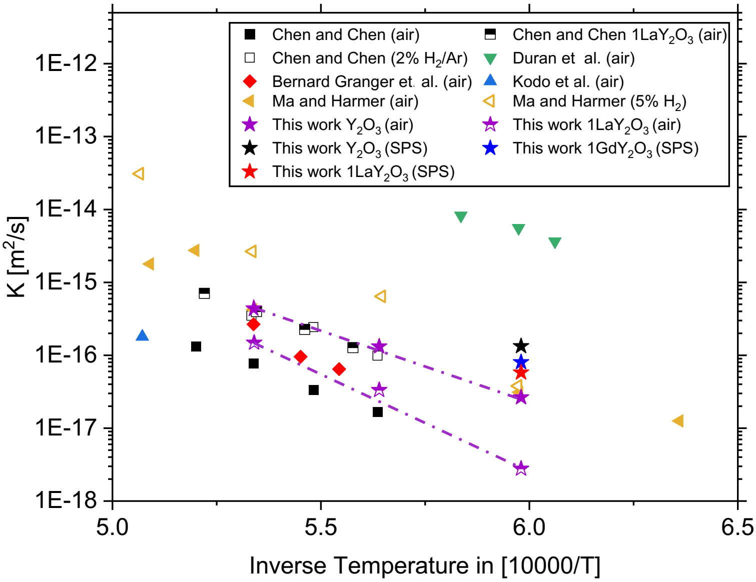

Fig. 4.26 Literature overview of the grain growth factor K displayed in an Arrhenius plot. Related values of K derived from this work are marked with stars.

grain boundary kinetic values reported in literature. Only the investigations by Duran et al. show very high mobility values which could be related to a not exactly defined amount of impurities in the investigated materials [165].

However, the measured grain growth factors in this work display the highest values with respect to the literature when the investigation was done under ambient atmosphere. Furthermore, a contrary effect of La doping on the mobility was observed when compared to the work of Chen and Chen [59]. In the present work, La doping leads to a clear reduction of mobility values due to solute and pore drag, while Chen and Chen reported an increased mobility in La doped Y_2O_3. This opposite behaviour could be induced by the direct implementation of nitrate precursors during powder synthesis in Chen and Chen's work. This leads to a homogeneous distribution of dopant atoms already in the starting powder, which could slow down or even prevent the segregation effects. Grain boundary mobilities calculated from the grain growth experiments during FAST/SPS showed slightly increased values when compared to mobilities calculated from pre-densified samples in air. This could be caused by the low oxygen partial pressure and the contact with graphite when processing by FAST/SPS, which both could trigger the generation of oxygen vacancies, which are known to increase the grain boundary migration rate in Y_2O_3 [57, 164].

The controlled doping of Y_2O_3 offers a versatile tool for the microstructure engineering of Y_2O_3 ceramics for the application in semiconductor industry. While the residual porosity in pure Y_2O_3 tends to detach from the grain boundaries during sintering, preventing their complete removal, the application of La doping successfully enables to pin the residual pores to the interface which allows continuous densification up to high densities. Using the fundamental understanding of dopant segregation in Y_2O_3 opens a new path to further reduce residual porosity. The application of rare earth doping in combination with optimized sintering has a high potential to increase the resistance under physicochemical etching conditions.

5 Results and Discussion Part II: Erosion Behaviour of Y_2O_3 in reactive plasma environments

The following chapter focuses on the discussion of the erosion behaviour of Y_2O_3 ceramics in fluorine based etching plasmas. Different key aspects of the erosion of polycrystalline Y_2O_3 were examined: (I) Extrinsic properties and surface defects which were induced during the processing of bulk ceramic components (II) Erosion behaviour under different plasma processing conditions (III) Intrinsic material properties of Y_2O_3 focusing on influence of microstructure and grain orientation. All aspects which govern the plasma-material interaction of bulk polycrystalline Y_2O_3 were considered. Therefore, sound conclusions could be drawn regarding the requirements of ceramic components in the semiconductor industry. Furthermore, a fundamental scientific understanding of the erosion attack was achieved.

5.1 Influence of processing induced surface defects

During the processing and machining of bulk ceramic components different microstructure defects are formed, which influence the material behaviour in contact with reactive etching plasmas. Here, three types of processing and manufacturing defects are discussed: (I) residual porosity caused by incomplete sintering (II) surface roughness (III) cracks induced by surface damage. Fig. 5.1 sketches the different types of processing and manufacturing induced defects.

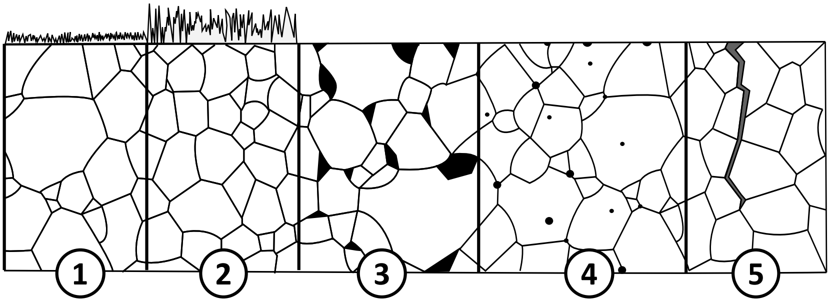

Fig. 5.1 Schematic graph of different processing induced surface defects. (1) fine ground surface finish (2) coarse ground surface finish (3) insufficient densification with a low relative density around 90.0 % (4) sufficient densification with a high relative density over 99.0 % (5) Surface crack induced during machining or mishandling of the component (in this work a hardness indenter is used to induce cracks).

Especially the influence of pores during the plasma exposure has been investigated in the past. Kim et al. and Ashizawa et al. demonstrated the dominating effect of surface pores on the resulting surface morphology after reactive plasma etching [17, 113]. Both studies investigated oxide materials (Al_2O_3 [113], Y_2O_3 [17]) with different pore sizes and clearly highlighted the preferred material removal at the edges of surface pores. Comparable observations were made after the exposure of thermally sprayed coatings which had a high amount of processing induced porosity [108, 110, 111]. Additional to the already discussed influence of surface pores, in the present work a comprehensive investigation was done to conclude on all the influences of surface defects. Therefore, samples were produced with a low relative density, high relative density, increased surface roughness and cracks, which were subjected to a reactive plasma etching environment. All samples were prepared by FAST/SPS. Samples with a low relative density were sintered at 1150 °C with 50 MPa pressure and 10 min dwell (Fig. 5.1 (3)). Samples with a high relative density were sintered at 1500 °C with 50 MPa pressure and 10 min dwell (Fig. 5.1 (4)). The surface roughness pf selected samples sintered at 1500 °C was roughened by mechanical grinding with SiC papers (high roughness P120 (Fig. 5.1 (2)), low roughness P1200 (Fig. 5.1 (1)). For comparison, the surface was polished by metallographical methods. Finally, surface cracks were induced in polished samples to mock a damaged component (Fig. 5.1 (5))

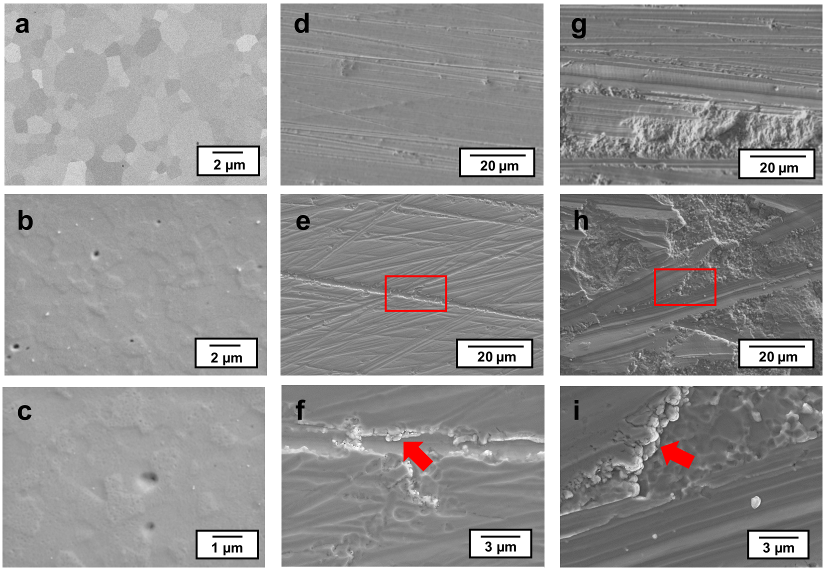

Fig. 5.2 SEM overview and detail images before and after exposure to a fluorine based etching plasma at a bias voltage of 150 V for 2h. All samples were sintered at 1500 °C, 50 MPa for 10 min and mirror polished (a), fine ground (d) and coarse ground (g). (b,e,h) shows the samples with different surface morphologies after plasma exposure. (c, f, i) shows related microstructure details in higher magnification.

All samples were subjected to fluorine etching plasma conditions using the experimental setup described in chapter 3.4 with a fixed plasma gas composition (S150; Tab. 3.6). The applied bias voltage was fixed at 150 V to enable a direct comparison of the behaviour of different surface qualities. The influence of processing induced surface defects are discussed in order as displayed in Fig. 5.1.
Fig. 5.2 shows the surface morphology of samples with a very low amount of residual pores, before the samples were exposed to the plasma atmosphere, as well as post-etching morphologies. Mirror polished surfaces (Fig. 5.2 a, c) display only a minor erosion of the surface. An exposure to the reactive plasma atmosphere leads to a porous surface reaction layer which shows a plateau-like topography resembling the underlying microstructure. The surface morphology and topography formation will be discussed in following sections in detail. In addition to the bulk material response, residual pores were mainly subjected to erosion. The edges of these pores got rounded resulting in an erosion crater, whose diameter increased with prolonged etching time. Samples, which were ground before plasma exposure, exhibited a rough surface (Fig. 5.2 d, g) with higher specific surface area and sharp grinding marks, which were more vulnerable to material removal during plasma etching than polished samples. Y_2O_3 samples ground with coarse SiC papers (P120) showed material breakouts additionally to characteristic grinding grooves, which can be found in both ground samples. Both kind of ground samples exhibited a levelling of the surface roughness due to preferred material removal on the sharp grinding marks. In higher magnification, accelerated erosion of positions, where material breakout occurred

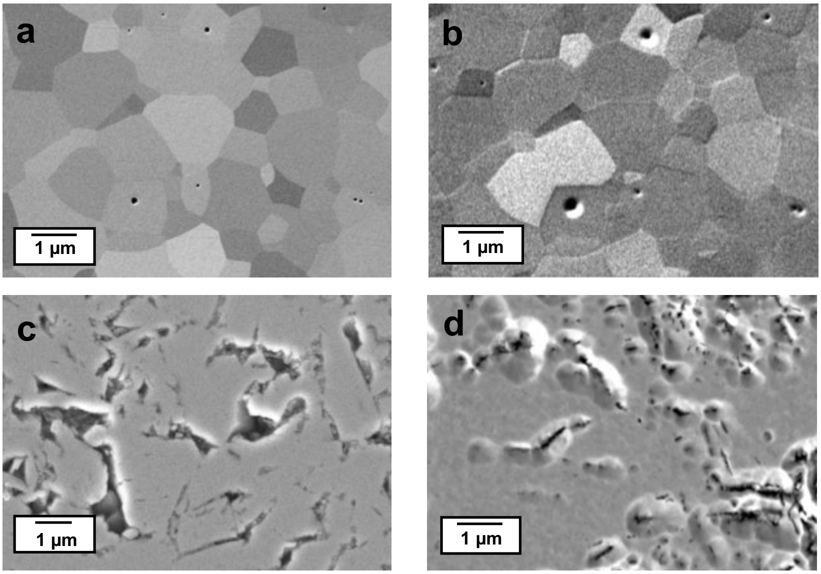

Fig. 5.3 SEM images of a dense sample (1500 °C, 50 MPa, 10 min) before (a) and after plasma exposure (b), as well as an insufficiently densified samples (1150 °C, 50 MPa, 10min) before (c) and after (d) plasma exposure.

was observed as well (marked by red arrows in Fig. 5.2 f, i). The removal of rough surface features could additionally cause formation of smaller wear particles especially during the initial phase of a plasma treatment. Therefore, the machining quality of ceramic components plays a major role to resist harsh plasma processing conditions. Nevertheless, plasma exposure enables to level out surface roughness, which might decrease the influence of initial surface roughness in the case of long term exposure. Additionally to the already discussed preferred erosion attack in the case of residual pores in Fig. 5.2 (b, c), Fig. 5.3 displays the plasma erosion behaviour of a Y_2O_3 sample with high porosity. The direct comparison between a highly dense sample (around 99.8% rel. density) in Fig 5.2 (a, b) and an insufficiently densified sample (around 90.0 % rel. density) in (c, d) clearly shows the dominating effect of pore content on the post etching topography. The clearly pronounced pore networks were subjected to the same erosion mechanism but comparably more severe surface damage could be observed. Contrarily, the parts of the surface without pores still showed a smooth appearance after etching (Fig. 5.3 d). Even in this case, a certain plateau-like topography was indicated in these areas.

To further investigate the active erosion mechanism acting on spherical surface pores, AFM investigations were carried out after etching. Fig. 5.4 shows the AFM measurement of an almost dense Y_2O_3 sample subjected to plasma etching for two hours with a bias voltage of 150 V. In addition to the topographic effect indicated by the color code in Fig. 5.4 a, the erosion attack on a selected pore is shown in Fig. 5.4 b. Line scans at different positions of the pore clearly exhibit the rounding of the pore edges. The initial pore diameter of around 100 nm (measurement not shown here) increases to a defect size of around 300 nm. The initially sharp edges of the pore after polishing were preferentially removed by physical sputtering due to their exposed faces. As final processing induced surface defect, hardness indentation cracks were subjected to the plasma etching environment. During manufacturing, handling and application of plasma facing components, surface cracks can occur due

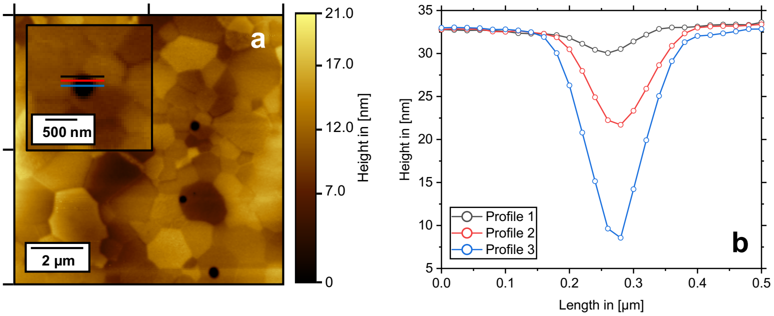

Fig. 5.4 (a) AFM topography scan of the surface of a dense sample after plasma exposure. Graphical detail highlights the position of line profiles in a spherical pore. (b) AFM line profiles through a spherical pore highlighting the main material removal process at sharp edges during the plasma exposure.

to mishandling. Fig. 5.5 shows related crack before (a, b) and after plasma exposure (c, d). The preferred erosion of sharp edges as observed in the case of pores can be directly transferred to surface cracks, which showed comparable erosion behaviour (increased defect area, rounded edges). Due to the local character of surface cracks induced by external damage the negative impact on the overall plasma performance should be containable.

All processing induced surface defects considered here have a significant influence on the erosion behaviour of polycrystalline Y_2O_3. The main material removal occurs in areas with high roughness or sharp edges. This leads to a reduction of plasma resistance due to inhomogeneous material removal throughout the whole plasma exposure. Especially high surface roughness values due to insufficient surface polishing is classified as critical with respect to the formation of particles especially in the beginning of the components life cycle. With increased operation time, it is expected that the risk of forming particles is reduced due to ongoing levelling of surface roughness and rounding of sharp edges.

Therefore, insufficient densification and small amounts of residual porosity are the major influence reducing the plasma resistance. The appearance of residual porosity in plasma facing components reduces the erosion resistance throughout the whole life cycle lowering the potential of these components especially for critical manufacturing steps in the semiconductor industry. As the last investigated defect, cracks have shown a quite comparable erosion behaviour to pores. Sharp edges formed during cracking get predominantly removed and increase the defect area. Nevertheless, the localized nature of cracks limits the impact onto the total plasma resistance of the component.

In the following section the impact of plasma processing parameters as well as the

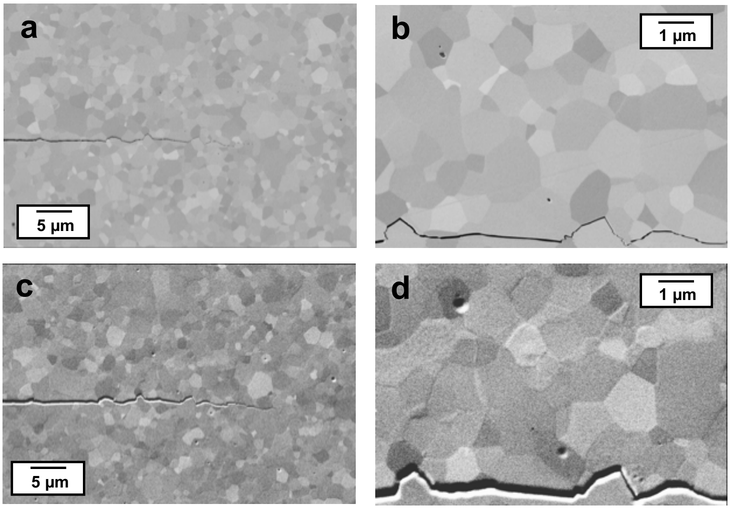

Fig. 5.5 SEM overview and detail images of a indentation induced cracks before (a, b) and after (c, d) plasma exposure under 150 V bias for 2 h.

intrinsic properties of Y_2O_3 on microstructural changes during plasma exposure was investigated in detail. Therefore, samples with high density and low surface roughness were produced to reduce processing induced influence factors to a minimum.

5.2 Influence of plasma processing parameters

This second part will focus on the investigation of the material behaviour under different plasma processing conditions. The two main parameters, which are discussed in literature to be rate and mechanism controlling are the applied bias voltage [9, 11] and the plasma gas composition, meaning the ratio between Ar and CF_4 [108, 167, 168]. Therefore, the influence of both parameters has been investigated thoroughly and will be discussed in detail.

5.2.1 Influence of applied bias voltage

As already explained in the introduction, the bias voltage is the main driving force for material removal in reactive plasma etching of polycrystalline ceramics because of the non-volatile phases formed during the chemical reaction with the fluorine containing plasma species [8]. This makes applied bias voltage one of the key parameters, which defines the generated surface morphology as well as the physical and chemical interaction in the near-surface area.

The reactive plasma erosion process is based on a physicochemical mechanism and the accelerating voltage defines the intensity of ion bombardment and therefore influences the major factors of the erosion mechanism:

- The fluorocarbon polymer layer deposition and its steady removal
- The interaction depth of the reactive species with respect to the surface
- The degree of physical material removal of ceramic and polymer reaction products from the surface

In this study, the focus lied on characterizing the surface topography as well as the reaction layer formation at three bias voltages of 50, 150 and 300 V. All other plasma parameters were kept constant (B50, S150, B300; Tab. 3.6) and dense and polished Y_2O_3 samples (1500 °C, 50 MPa, 10 min) were investigated to minimize the impact of surface defects. All samples were subjected to a reactive plasma atmosphere for two hours enabling a direct comparison to subsequent investigations focusing on the influence of grain orientation.

Fig. 5.6 shows SEM images of the surface morphology as a function of the applied bias voltage. The comparison of the surface topographies clearly indicates the strong impact of bias voltage on the topography after plasma exposure. The surface morphology after a plasma exposure under 50 V bias (Fig. 5.6 a) shows only slight microstructure changes. Grain boundaries and pores seemed to get preferentially attacked during the exposure. At this bias voltage, surface grooving and pore

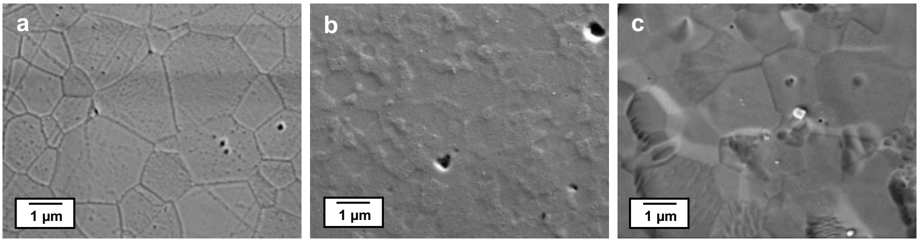

Fig. 5.6 SEM images of the surface morphology after a plasma exposure for 2 h under a bias voltage of (a) 50 V (b) 150 V (c) 300V.

rounding were less pronounced, but first changes in the surface morphology between different grains were already visible.

Increasing the applied bias voltage to 150 V strongly changes the morphological appearance of the surface after plasma exposure. Higher sputtering rates form a nano porous surface morphology, which is selective in its development, leading to areas with a strong formation of nano-porous appearance and areas with no formation of this kind of top layer. Furthermore, a plateau-like surface topography appeared, which depicts the grain structure of polycrystalline Y_2O_3. Additionally, surface pores show a strong rounding due to the predominant removal of their sharp edges.

A further increase of the bias voltage to 300 V led to a much more pronounced change of surface topography compared to the microstructure at lower accelerating voltages. Here, the formation of the morphology is dominated by an increased amount of material removal due to physical sputtering leading to a surface with clearly increased roughness. The nano-porous surface layer was not observable anymore indicating a high removal rate of the reaction layers formed at the surface. Additionally, it is possible to distinguish between three different categories of grain dependent morphologies: (I) in detail, smooth and flat surfaces, (II) rough and flat surfaces and (III) microstructural rumpling were formed. The microstructure dependent formation of different morphologies could be connected to a removal process which is dependent on the crystallographic orientation of certain grains. The connection between these intrinsic properties of Y_2O_3 will be discussed in detail in the following chapters 5.3 and 5.4.

Further investigations of the surface topography depending on etching parameters were performed using AFM on the samples displayed in 5.6. The topographic scans in Fig. 5.7 (a, c, d) confirmed the increase of surface damage with increased bias voltages over 50 V. While the topography after the exposure at 50 V leaves the microstructure almost physically undamaged, voltages of 150 V and 300 V caused strong topographic changes which depended on the primary grain structure. Furthermore, the amplitude scans displayed in Fig. 5.7 (b, d, f) clearly illustrate the formation of different morphologies at low and high bias voltages. The formation of nano-porous top layers was limited to lower bias voltages while high voltages of 300 V caused a complete removal of the intermediate surface layer.

In addition to the microstructure dependent topography formation, high bias voltages

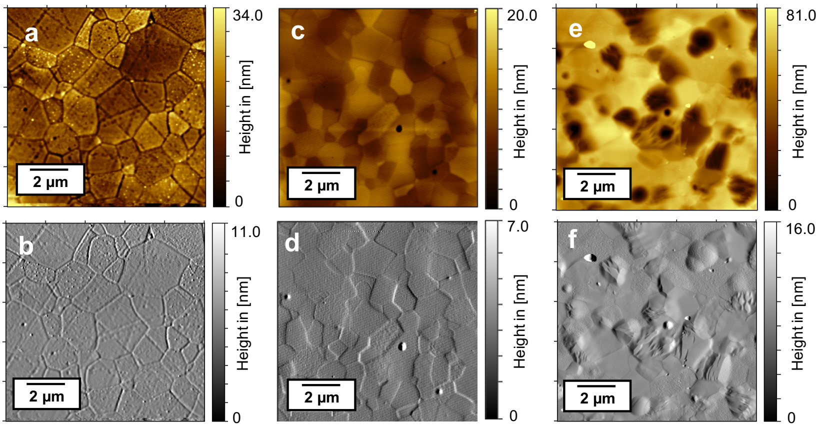

Fig. 5.7 AFM scans of the surface morphology in topographic and amplitude mode after a plasma exposure for 2 h under a bias voltage of (a, b) 50 V. (c, d) 150 V. (e, f) 300V.

hint on an independent, superimposed removal mechanism leading to sputtering craters randomly distributed on the surface. Fig. 5.8 shows details of the AFM scan of a sample surface after being exposed to a bias voltage of 300 V focusing on the orientation dependent topography. Line profiles are extracted from the topography scan to highlight different surface morphologies, which were dependent on the underlying microstructure. Grains represented by red and blue lines exhibited a flat surface and differed only by a slightly increased roughness of certain grains. In

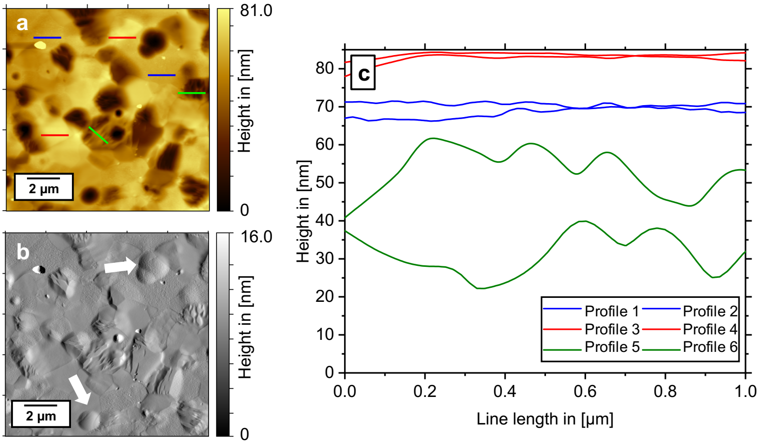

Fig. 5.8 Detailed AFM analysis of the surface morphology after a plasma exposure for 2 h under a bias voltage of 300V in topographic (a) and amplitude mode (b). Colored lines in (a) mark the position of the AFM line profiles. Arrows in (b) highlight the position of microstructure independent sputtering craters. (c) AFM line profiles extracted from topography scan.

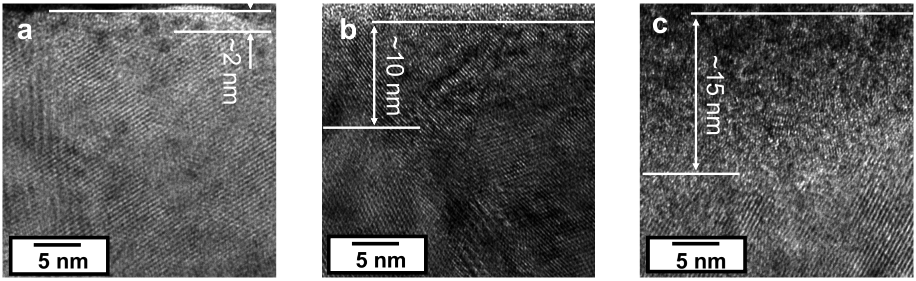

Fig. 5.9 HRTEM images of Y_2O_3 after plasma exposure for 2 h under varied bias voltages of 50 V (a), 150 V (b) and 300 V (c). Included markers illustrate the increasing physical interaction depth from the surface.

contrast, grains indexed by green lines display a clearly rugged surface. This specific morphological effect was observable only at high Ar^+ ion energies and indicated a strong orientation dependency, which has been only described so far for metals exposed to plasma environments [169, 170].
Furthermore, microstructure independent craters are visible (white arrows), which indicated an additional erosion mechanism superimposing the already described orientation dependent removal mechanism. The variation of the accelerating voltage during the plasma exposure of Y_2O_3 ceramics revealed major differences between the erosion mechanisms that were active under different plasma processing parameters. The erosion under 50 V bias was almost negligible due to the dominating surface fluorination [8, 98, 102], which mainly forms non-volatile reaction products. This reaction layer is stable against low energy sputtering, leading to a strong deceleration of the removal process and a high resistance against the plasma exposure.
Increasing the voltage to 150 V changes the surface reaction and material removal mechanism based on a mixed chemical and physical erosion. The deposition of fluorine containing species on the surface and the connected fluorination of Y_2O_3 are in equilibrium with the physically induced material removal through sputtering. This mixed erosion process leads to the observed nano-porous layer indicating the formation of a fluorine reaction layer as well as a microstructure dependent plateau-like topography. A further increase of the bias voltage up to 300 V changes the main erosion mechanism towards a physically dominated process. Additional physical erosion mechanisms are activated leading to a topography, which depends on the initial grain orientation and microstructure independent sputtering craters.
Additional to the investigation of the surface topography the influence of different bias voltages on the microstructure and chemical composition of the near-surface area was examined using TEM and TOF-SIMS. The DC self-bias voltage was varied again between 50 V, 150 V and 300 V to see its influence on the erosion behaviour and the resulting topography. First, the physical interaction and microstructural changes induced by the ion bombardment during plasma exposure were investigated by HRTEM (Fig. 5.9). When increasing the bias voltage from 50V to 300V, the depth of the influenced zone on the surface became clearly more pronounced. The

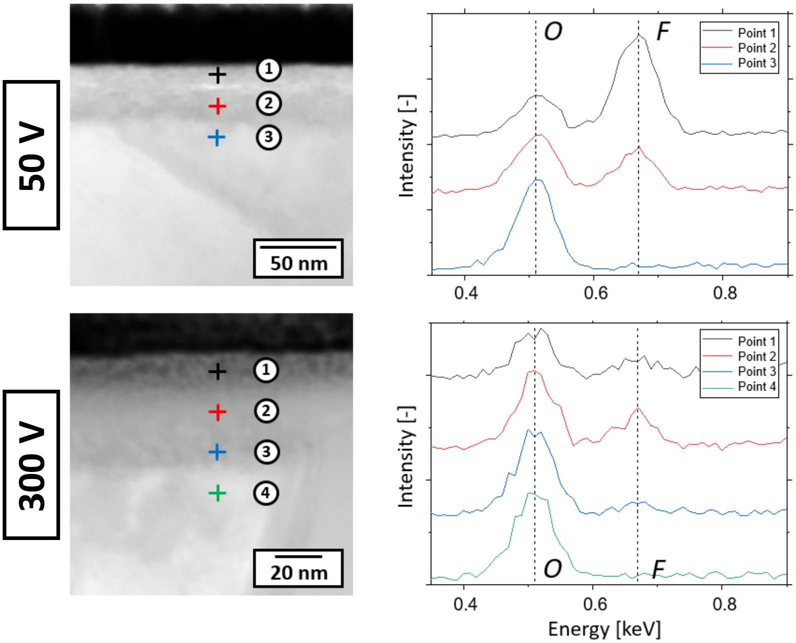

Fig. 5.10 (left) STEM-EDS images of Y_2O_3 after plasma exposure for 2 h under varying bias voltages (as indicated). (right) EDS spectra at different positions from the surface to the bulk (as indicated).

physical damage at 50 V bias voltage was almost negligible. Increasing the bias voltage to 150 V and 300 V expanded the influenced top layer from 10 to 15 nm and induced areas having an amorphous appearance. On the other hand, the crystal structure below the physically damaged layer remained unchanged. These results confirm the combined or mixed erosion mechanism that is active during the plasma exposure at high bias voltages. A chemical surface reaction is superimposed by physical damage induced by ion irradiation.

Additionally, STEM and EDS measurements were done to investigate the influence of bias voltage on the reaction layer formation and the microstructural damage. Fig. 5.10 displays STEM images of the near surface area of Y_2O_3 exposed to a bias voltage of 50 V and 300 V for 2h. A clear difference in the appearance of the affected surface layer is visible between both samples. The Y_2O_3 sample exposed to a low bias voltage of 50 V is characterized by a top layer with two distinguishable sublayers having a thickness of around 14±1 nm (top) and 12±2 nm (bottom).

The associated EDS analysis (distinct positions are marked with crosses in the STEM image) showed a clear difference in the chemical composition of the reaction layer. In the top layer, a high fluorine intensity was found, which was probably induced by fluorocarbon deposition and direct contact with the reactive species of the etching plasma. The lower layer displayed a balanced oxygen/fluorine composition, while

the spectrum below the reaction layer showed no indication of fluorine. The lower physical sputtering potential at bias voltage of 50 V has a clearly reduced effect on the reaction layer formation. Compared to the estimated layer thickness by Kim et al. (around 8 nm), the measured interaction depth is strongly increased to 35 nm in our investigations [11]. This could be induced by the higher bias voltages of 300 to 800 V used by Kim et al. which outranges the maximal bias voltage used in this work and shifting the plasma erosion in a strongly physically dominated regime.
Furthermore, STEM images of the interaction zone formed at bias voltages of 300 V display an increased interaction depth (44±3 nm). Compared to samples subjected to lower voltages (50 - 150 V), an additional top layer is observable that exhibits a porous appearance. This additional layer is characterized by dark and porous appearing domains as well as lower EDS intensities, which could be induced by inhomogeneous material removal leading to the porous and rough surface morphology displayed in Fig. 5.6 and Chapter 5.2.1. The corresponding EDS analysis showed a lower fluorine intensity in the porous top layer, which was slightly increased in the layer below it, but never reaches the characteristic distribution at lower bias voltages. This result could be caused by the increased influence of physical sputtering, which accelerated the erosion of the fluorinated top layer and increased ion damage in the underlying material, as already observed in HR-TEM imaging.
Additionally, the microstructural changes and the characteristic chemical gradient of samples subjected to high bias voltages hint on an increased surface erosion through physical ion sputtering, which led to predominant removal of fluorine containing phases from the surface coupled with a more pronounced chemical interaction with the reactive plasma atmosphere. Sputtering yield studies of Y_2O_3 and its corresponding fluoride YF_3 by Kim et al. observed a four times higher yield for the fluoride compound [12], which could have caused the depletion of fluoride phases in the top surface layer at 300 V bias voltage observed in this work.
The TEM-EDS results on samples with different bias voltages enable a deeper insight into the different stages of erosion and material loss during plasma exposure. Continuous surface and near-surface fluorination were responsible for the formation of YF_3 and YOF compounds, which are predominantly removed by Ar^+ ion sputtering. At first, chemical surface changes led to the depletion of Y_2O_3, but the subsequent material removal process is mainly controlled by the physical interaction of the surface layer with Ar^+ ions. Although the EDS analysis revealed chemical interaction to a depth of up to 35 nm for samples subjected to a bias voltage of 50 V, this interaction did not distort the lattice structure as confirmed by HR-TEM (fig. 5.9).
Complementary to TEM-EDS investigations, TOF-SIMS depth profiles were measured to deepen the understanding of chemical gradient formation under varied bias voltages. The TOF-SIMS measurements displayed in Fig. 5.11 were focused on the intensities of oxygen, fluorine and yttrium near the surface. As already observed during TEM-EDS measurements, the chemical gradients highly depend on the applied bias voltage. Low bias voltages of 50 V induced a homogenous fluorine layer (Zone II) with a thickness of around 35 nm. The chemical interaction between the reactive fluorine species and the ceramic sample dominated the plasma-material interaction at low bias voltage. This is consistent with the undamaged lattice structure which

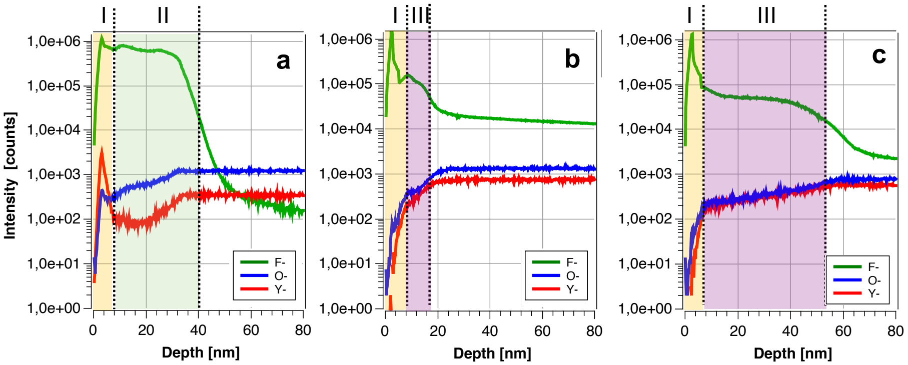

Fig. 5.11 TOF-SIMS depth profiles showing the intensities of Y-, O- and F- for Y_2O_3 exposed to bias voltages of 50 (a), 150 (b) and 300 V (c). The background colour highlights the different characteristics of fluorine intensity depending on the applied voltage (I) high fluorine surface peak. (II) high fluorine intensity layer up to a depth of 40 nm at low bias voltages. (III) significantly decreased fluorine intensity in the bulk at high bias voltages.

was observed by HRTEM (Fig. 5.9) as well as the chemical gradient measured by EDS (Fig. 5.10). While at 50 V, the attack is chemically driven, at intermediate and high bias voltages of 150 and 300 V a clear change of the fluorine gradient was observed, resulting in a third zone which is showing a stronger influence of physical sputtering (Zone III). The fluorine distribution is separated into two zones: Zone (I) had a high fluorine concentration, which is caused by the characteristic fluorocarbon layer deposited during etching [8, 102]. Zone (III) exhibited a lower fluorine concentration and a voltage dependent interaction gradient. Hereby, higher bias voltages lead to an increased interaction depth of the fluorine species. The measured oxygen intensity close to the surface behaved contrary with respect to the fluorine distribution supporting a reaction mechanism controlled by the replacement of oxygen atoms in the structure by fluorine atoms, which was already described in previous studies [8, 10, 11]. The present study of the chemical and physical interaction induced by varied bias voltages clearly confirmed these observations. The bias voltage is the main parameter defining physical interaction depth, chemical gradients as well as the surface topography and therefore has a major impact on the long-term stability of the component under plasma etching conditions.

5.2.2 Influence of plasma composition

The plasma gas composition is another important process parameter influencing the erosion behaviour of polycrystalline ceramics during plasma exposure. Only a small number of investigations consider this parameter and focus on chlorine containing etch gases [108, 167, 168]. The ratio between the chemically reactive plasma species (in this work CF_4) and the ionized plasma component (in most cases Ar) strongly determines the amount of reactive atoms and radicals as well as the amount of ionized Ar needed for sputtering. The gas composition can change the erosion mechanism

from chemically to physically controlled mode, having a large impact on the material response e.g. etching rate, particle formation and resulting surface morphology.
To investigate this in further detail, dense Y_2O_3 samples (1500 °C, 50 MPa, 10 min) were subjected to different plasma compositions using a bias voltage of 150 V and an exposure duration of 2 h. The composition (defined by volume percentage of CF_4) was varied from 5 % , 10% , 40% to 80 % CF_4 (C5, C10, C40, C80; Tab. 3.6). The corresponding Ar content was set to 95 %, 90 %, 60 %, and 20 %. The experimental procedure was adjusted to be in accordance with investigations conducted by M. Stamminger on SiO_2 and Al doped SiO_2 [117].
The influence of CF_4 volume percentage on the surface topography after plasma exposure is displayed in Fig. 5.12. The microstructure at the surface is strongly dependent on the CF_4/Ar ratio showing three types of erosion modes: (I) Fig. 5.12 (a) shows a homogeneous distribution of microstructure independent sputtering craters. A comparable surface topography was already observed in samples subjected to high bias voltages (Fig. 5.6 and Fig. 5.7) indicating a physically dominated etching attack. (II) Fig. 5.12 (b, c) exhibits a microstructure dependent surface topography which was already observed at intermediate bias voltages of 150 V, indicating a mixed erosion mechanism. (III) Fig. 5.12 (d) shows a very smooth surface indicating only a minor effect of the initial grain structure.
Comparing the surface topography by the means of SEM imaging shed light on the dominant etching mechanism. The characteristic material response of Y_2O_3 depended on the amount of physical and chemical contribution during the exposure. A high amount of Ar^+ ions or increased bias voltages induced a removal process which is dominated by physical sputtering. Material removal by ion sputtering is the rate

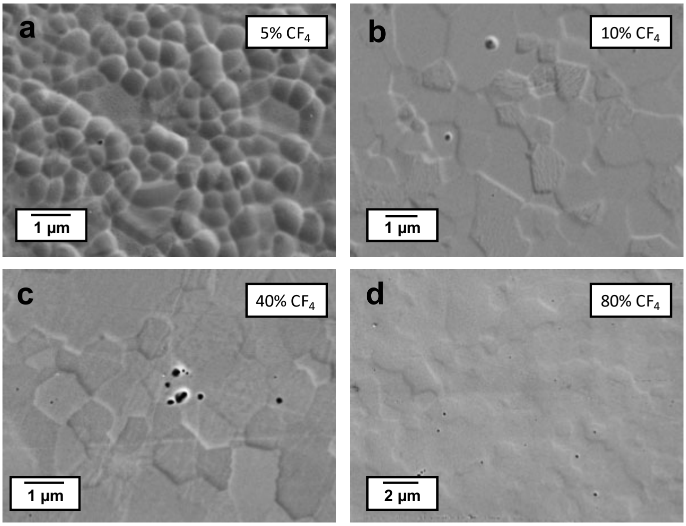

Fig. 5.12 SEM images of the surface morphology after a plasma exposure under 150 V for 2 h having a CF_4 volume percentage of (a) 5 % (b) 10% (c) 40% (d) 80 %.

controlling mechanism leading to a microstructure independent etch morphology and to high removal rates. The ongoing fluorocarbon deposition-removal process during plasma etching is shifted strongly towards a fast removal of reactive species from the surface but nevertheless inducing a certain amount of fluorination. Increasing the CF_4 percentage from 5 % to 10 % and further to 40 % shifted the competing removal processes more to a mixed chemical-physical regime where a microstructure dependent erosion mechanism became active as indicated by the formation of a surface topography representing the initial grain structure. Hereby, the deposition of the fluorocarbon layer on the surface plays a more dominant role leading to a grain orientation dependent etching mechanism, which will be discussed in more detail in the following section. Replacing large amounts of Ar in the plasma gas composition by CF_4 leads to a chemically dominated erosion. Due to the non-volatile nature of the reaction products which are formed during the chemical plasma attack and the low amount of ionized Ar in the plasma chamber the erosion rate strongly decelerated and almost no material removal was observed.

The change of the plasma interaction caused by varied gas compositions also shows a strong impact on the etching rate displayed in Fig. 5.13. A comparison with the etching rates measured on commercial quartz glass demonstrates the superior etching performance of Y_2O_3 ceramics, which showed etching rates orders of magnitude lower. The highest removal rate for Y_2O_3 was observed when physical sputtering was dominating the material removal process due to fast fluorocarbon deposition -

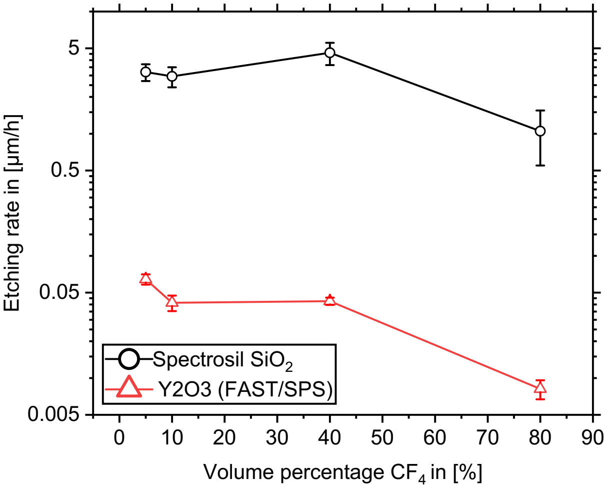

Fig. 5.13 Etching rate of Y_2O_3 and SiO_2 dependent on the plasma gas composition. The etch rate was determined on an etch step induced through masking parts of the exposed area. All samples were treated with a bias voltage of 150 V and the exposure duration was 2 h. The etch depth was determined using a confocal laser microscope for SiO_2 and an AFM for Y_2O_3.

surface reaction - material removal cycles. The etching rate decreased to intermediate values in the mixed erosion regime and only very small removal rates were measured in a chemically dominated plasma environment. These results confirm the plasma-material interaction behaviour which was already concluded from the surface morphology investigations. Hereby physical sputtering enabled the surface fluorination by breaking Y-O bonds and replacing them by Y-F bonds [8, 11]. The plasma activated surface reaction accelerates the formation of a reaction layer which is prone to removal by physical sputtering. Decreasing the amount of available Ar ions in the plasma composition reduces the sputtering yield and changes surface morphology as well as etching rates. A further decrease of the Ar ratio leads to an almost complete stop of the physical removal process due to the dominant chemical deposition and reaction kinetics leading to negligible surface damage.

For a better understanding of chemical interaction in the near surface region, the reaction layer formation was investigated by TOF-SIMS. Fig. 5.14 displays the chemical gradients at the surface focusing of the concentration of fluorine, oxygen, carbon and yttrium depending on the sputtering depth. The change of the plasma

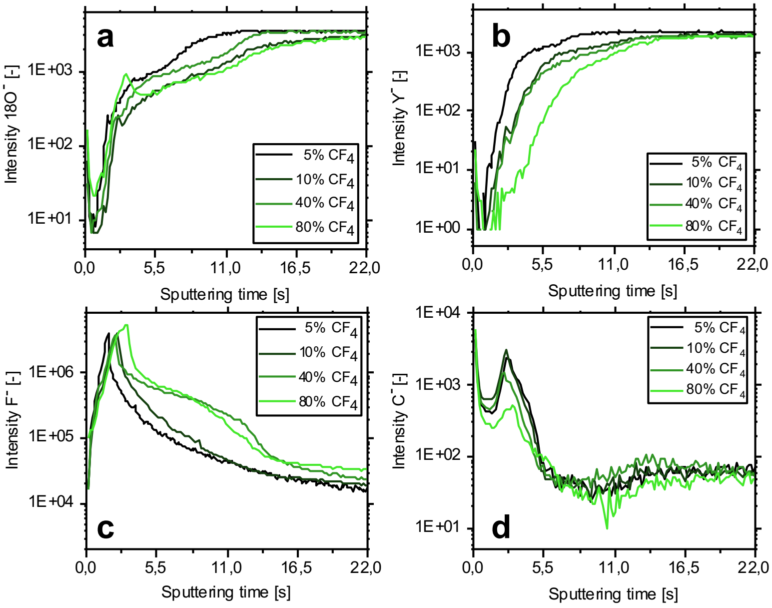

Fig. 5.14 TOF-SIMS depth profiles of all samples tested with different plasma gas compositions. Intensities of relevant elements are visualized in separated graphs showing (a) 18 O^- (b) Y^- (c) F^- and (d) C^-

gas composition to higher CF_4 concentrations led to a change of the chemical gradient formation at the surface. This was especially indicated by the fluorine distribution at the surface. Lower amounts of CF_4 in the plasma gas led to a constant and sharp decrease in intensity while high CF_4 amounts led to a two step gradient which was already observed in Fig. 5.11. The high concentration of ionized Ar in the low CF_4 regime led to a reaction process dominated by physical sputtering, directly removing fluorine reaction products from the surface and preventing a deeper chemical interaction. Comparable behaviour is indicated by the chemical gradients of oxygen and yttrium as well. These results support the presence of different clearly distinguishable etching regimes which not only influence the morphological appearance at the surface but also change the chemical interaction with the material. During a physically dominated erosion, fluorine species get removed directly due to high sputtering rate preventing the formation of a chemical fluorine gradient. Changing the plasma gas composition into the fluorine rich regime, fluorine atoms penetrate the surface way deeper forming a type III gradient (Fig. 5.11). The chemical gradients of oxygen, yttrium and carbon behave accordingly mirroring the gradients introduced by fluorine interaction.

The variation of plasma processing parameters investigated in this section enables to draw sound conclusions on the material response of polycrystalline Y_2O_3 under different plasma conditions. As discussed before the material behaviour can be categorized into three different types of characteristic microstructural responses: (P) physically dominated erosion (M) mixed erosion (C) chemically dominated erosion. Based on the parameter study, a process parameter - material response map has been sketched in Fig. 5.15. Visualizing the influence of bias voltage and gas composition on the observed plasma damage allows to derive a schematic representation of active mechanisms. The observed mixed erosion behaviour, which will be discussed in detail

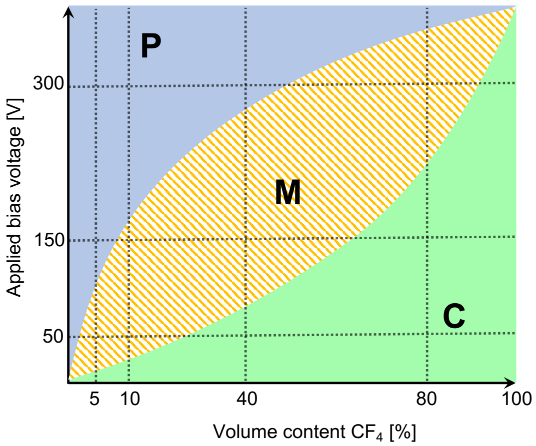

Fig. 5.15 Schematic plasma processing map displaying the active erosion mechanisms (P-physical, M-mixed, C-chemical erosion) under varying plasma parameters.

in the subsequent chapter, is located between a chemically dominated erosion leading to minor surface and material damage and a physically dominated erosion exhibiting higher material removal rates and a strong surface damage. The processing map can help to estimate the material response at a given parameter set, which is expected to be a helpful tool for lifetime predictions of Y_2O_3 components when exposed to reactive fluorine plasmas.

5.3 Influence of microstructure and crystalline orientation

Finally, the intrinsic properties of Y_2O_3 and the chemo-physical mechanism, which is active during a mixed erosion behaviour, are be discussed in detail. Furthermore, the erosion resistance of a Y_2O_3/YOF model composite was investigated to compare the erosion behaviour of both materials on the microscopic scale. This study helps to evaluate the potential of fluorine containing yttrium compounds in comparison to pure oxides.

5.3.1 Behaviour of pure Y_2O_3

Topographic phenomena induced by a mixed chemical and physical plasma exposure have been already observed on samples discussed in previous sections. In this section, the fundamental mechanisms were investigated using Y_2O_3 to understand the behaviour of the pure material and Y_2O_3/YOF composites to consider the influence of fluorination.

Therefore, the surface topography of mirror polished, almost dense samples (1500°C, 50 MPa, 10 min) was investigated before and after a plasma exposure. The bias voltage was fixed at 150 V, the duration of exposure was 2 h and the standard parameters (S150; Tab. 3.6) were applied. The re-localization method introduced in the experimental section was utilized for most of the investigations conducted in this section to establish a correlation between the microstructure before and the morphology after plasma etching. At first, SEM overview and detail images of the microstructure before and after the plasma exposure are displayed in Fig. 5.16. The polished sample (a, c) exhibited almost no topographical features except a minor amount of residual porosity which was visible in both images. The SEM configuration allowed to visualize the crystallographic orientation contrast, making the microstructure, e. g. the grain orientation differences visible before and after etching. The SEM images after the plasma exposure (b, d) revealed a microstructure dependent topography, which had a plateau-like appearance. Residual pores showed the characteristic rounding effect discussed in previous sections. This effect will not be considered further during this section. Due to the clearly visible grain orientation contrast the direct connection between grain orientation and the formed topography becomes apparent. Selected surface grains revealed a slightly increased tendency to get eroded, while others had an increased resistance against plasma erosion.

Comparable observations were reported for different metals and alloys, e. g. steel

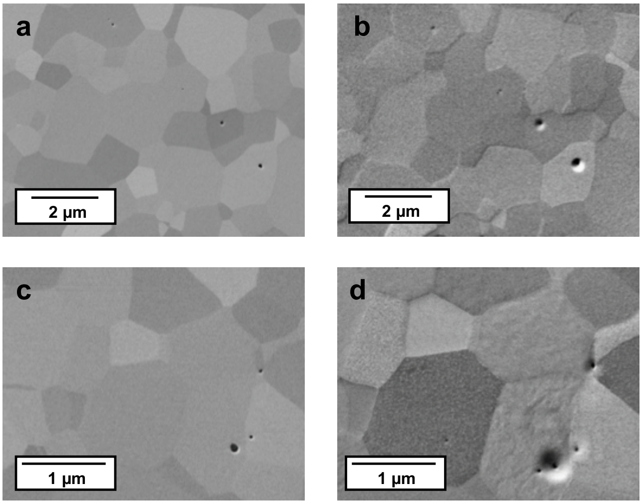

Fig. 5.16 SEM overview and detail images of the surface before (a, c) and after (b, d) plasma exposure.

[169] and tungsten [170, 171, 172], after the exposure to experimental fusion plasmas. Although the experimental set-up used in literature differed from the plasma etching conditions applied in this work, a clear orientation dependency was described for all of these metallic materials. The major differences are the applied ionic flux and the reactive species ($H^+, Ar^+, D^+ - Ar^+$) present during the exposure. In the present work, an additional influence of fluorocarbons being present during the reactive etching of Y_2O_3 had to be considered as well. Nevertheless, comparable erosion pathways could be active during the exposure of polycrystalline Y_2O_3 to reactive fluorine plasmas.

For a detailed analysis of the topographic surface features selected areas were investigated using AFM (Fig. 5.17). A correlation between the grain orientation (visible through grey scales in the SEM image) and the topographic height revealed

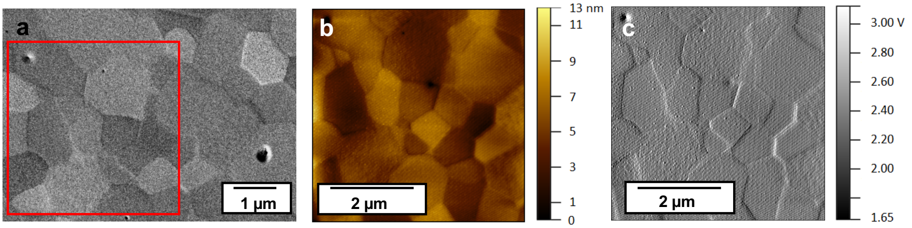

Fig. 5.17 (a) SEM image of the surface topography after plasma exposure (b) AFM topography scan of the highlighted area in (a) showing the microstructure dependent topography (c) AFM amplitude scan showing different morphologies for certain grains in the microstructure.

that the grains formed a plateau-like structure. The plasma etching induced surface topography was directly connected to the initial grain structure, an effect, reported in literature so far only for metals exposed to fusion plasmas. Accordingly, a correlation between crystalline orientation and erosion resistance seems reasonable for polycrystalline ceramics like Y_2O_3 as well. Compared to metallic compounds the observed surface relief was less pronounced, which is reasonable considering the lower sputtering yields of ceramic materials [12, 173]. Additionally, AFM line profiles were derived from the topography scan to better visualize the kind of the plateau formation. Clear height differences between single grains were visible and although not all displayed plateaus were even the significant height difference supports the hypothesis of a grain orientation dependent erosion mechanism. Additionally, the amplitude scan in Fig. 5.17 (b) shows different surface morphologies which are dependent on the grain orientation. A possible explanation of this effect could be differences in the fluorocarbon deposition and removal process, which strongly influences the subsequent degree of erosion. Therefore, a detailed discussion focusing on the morphology formation influenced by the fluorination process will be included in a later section.

For a better understanding of the relationship between crystalline orientation and the formation of the plateau-like topography, electron backscatter diffraction (EBSD) investigations were coupled with AFM measurements. A direct comparison of the surface orientation (inverse pole figure (IPF) colourization of the Z-direction) before the plasma exposure and the corresponding AFM topography is displayed in Fig.

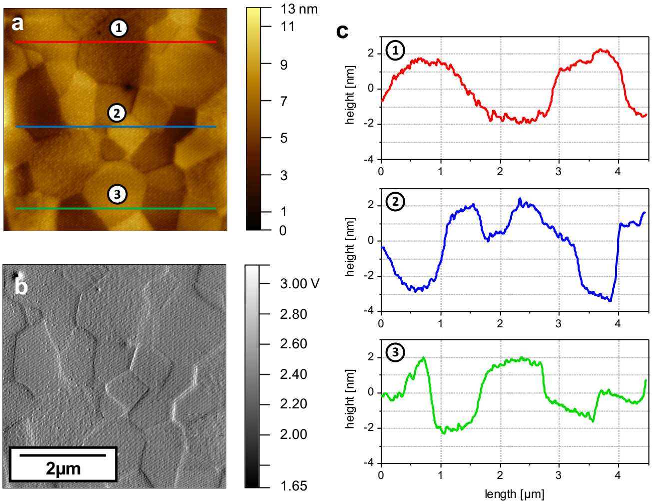

Fig. 5.18 (a) AFM topography scan of the microstructure dependent surface morphology (b) AFM amplitude scan (c) AFM line profiles extracted from the topography showing distinct height levels induced by plasma etching.

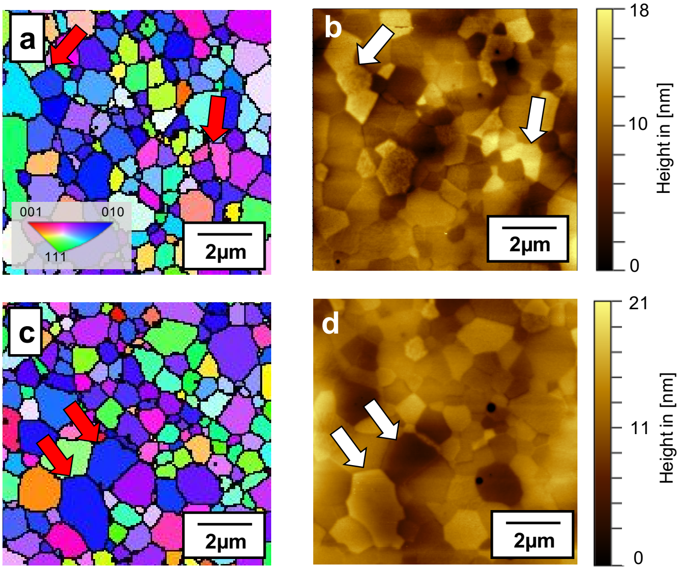

Fig. 5.19 (a, c) EBSD orientation mapping before the plasma exposure (arrows indicate grains with comparable and different orientations) (c, d) Re-localized AFM topography scans at the same position after exposure showing an orientation dependent surface structure.

5.19. As previously discussed, after plasma exposure a distinguishable microstructure dependent topography was formed. A simple comparison of grain orientations (represented through IPF colourization) and the corresponding AFM height profile did not allow a straightforward conclusion on the relationship between selected grain orientations and low or high erosion depths. The red arrows in Fig. 5.19 (a, c) mark selected grains which have a comparable grain orientation but do not necessarily show the same AFM height level and vice versa.

Due to the insufficient conclusions derivable from direct comparison, a comprehensive analysis of the EBSD data and the AFM height topography was conducted. The three Euler angles, which define the orientation of single crystallites in relation to the sample coordinate system, were directly correlated to the AFM height difference. The height difference is defined by the Z-offset of a certain grain related to the lowest grain in the AFM scan. This allows the comparison of multiple AFM scans by scaling the topography to the deepest position and correlating the topographic data to the specific grain orientation. The generated data set is visualized in Fig. 5.20 showing the AFM high difference of all investigated grains using the maximum and minimum values as error bars. Two types of visualizations were used: Fig. 5.20 (a) shows the height difference dependent on the second Euler angle ϕ, while (b) shows a scatter plot using φ_2 and ϕ as the variables, enabling the visualization of two rotation angels at once. To better distinguish between different height levels a colour key was applied in both graphs. Despite the significant amount of scatter present in the data set,

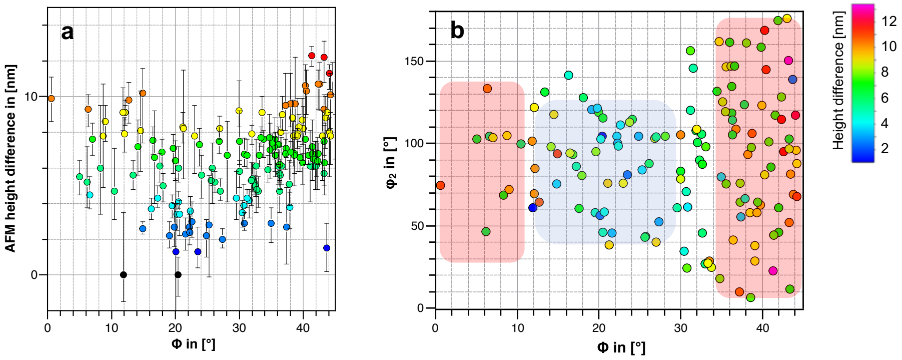

Fig. 5.20 Correlation of the AFM height difference to the Euler angles ϕ (a) and φ_2 as well as ϕ (b). φ_2 as and ϕ were derived from EBSD measurements before the plasma exposure.

grain orientations in the range of $\phi = 0 - 10°$ and $\phi = 40$ - 45° show the largest height difference, meaning a good erosion resistance. Vice versa, grain orientations with a $\phi = 15$ - 30° displayed the lowest average height difference which means an overall lower etching resistance is observed. Background colourization is used to highlight areas in which the orientations exhibiting maximum and minimum height differences. Additionally, Fig. 5.20 (b) further indicates the height difference depending on φ_2, but due to a lack of sufficient available data points, the direct dependency between φ_2 and the topography cannot be derived. The formation of the plasma induced etching topography seems to be mainly depending on the rotation along the Y-axis from $\phi = 0$ to $\phi = 45°$. In the cubic crystal structure, this rotation is related to a tilt of the [001] plane to the [011] plane (with respect to the Z-direction). This rotation leads to a change in the alignment of the lattice planes of the crystal with respect to the surface.

A comparable mechanism was described by Roosendahl et al. revealing an orientation dependency of the sputtering yield of metal single crystals [173]. In this study, metallic single crystals of Cu, Ni, and semiconductors like Ge and InSb were investigated and exhibited lower sputtering rates at angles which were highly aligned to certain crystal directions. The related physical effect has been described even earlier by Onderlinden using a so-called "channelling model" [174]. It is assumed that ions which impact on a crystalline surface contribute less to the physical sputtering of the material when they are aligned to a certain crystalline direction (called "transparent direction"). The plasma ions channel along aligned lattice planes into the bulk and contribute a smaller amount of their kinetic energy to the removal of atoms from the surface. Vice versa the penetration depth of the plasma ions is increased. In contrast, unaligned ions interact significantly stronger with the surface atoms leading to a physical removal of the first atomic layers. This effect found an application in the deposition of crystallographically oriented layers by ion beam assisted deposition (IBAD)[175]. This coating technique uses the effect of ion channelling to deposit

different crystallographic oriented metallic [176] and ceramic [177] layers.
The concept of ion channelling can be partially adapted to the plasma etching induced surface topography observed in polycrystalline Y_2O_3 explaining the appearing erosion mechanisms to some degree. Therefore, a simplified distribution of the measured dataset is displayed in Fig. 5.21. An average height distribution curve was derived by fitting the median values of the height difference which are displayed dependent on the Euler angle ϕ from 0 to 45 ° (measured data is visible in the background). Additionally, crystal structures of Y_2O_3 at angles of $\phi = 0$ °, $\phi = 15$ °, $\phi = 30$ ° and $\phi = 45$ ° were included into the graph, showing how the rotation along the y-axis is aligned with the lattice planes. Orientations with an angle of 0 ° and 45 ° show a strong crystallographic alignment which is expected to induce a higher probability of ion channelling into the bulk along these respective directions. A comparison of the angle-dependent crystal structure with the measured topographic data demonstrated that the lowest sputtering yields were predominantly measured at angles displaying a higher ion transparency.
Although the channelling theory might explain a certain fraction of the underlying physical phenomena leading to a predominant removal of grains with a high crystallographic alignment, other influencing factors like fluorocarbon deposition and surface fluorination have not been taken into account. These additional chemical influences during the plasma exposure are expected to induce further overlapping erosion mechanisms, which might be also the reason for the large scattering of the erosion data at a given grain orientation in Fig. 5.20.
Therefore, a direct comparison with a compound, which already contained fluorine

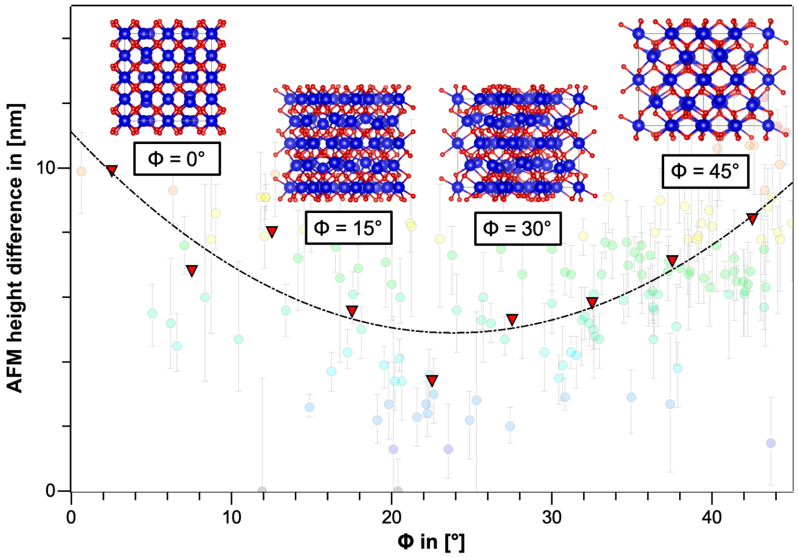

Fig. 5.21 Median values of the AFM height difference dependent on the Euler angle ϕ. Representations of the crystal structure of Y_2O_3 at different rotation angles from $\phi = 0°$ to $\phi = 45°$

in its structure (here, YOF) was plasma treated. An investigation of its erosion behaviour compared to pure Y_2O_3 helped to understand the influence of fluorination on plasma erosion and to estimate the performance of oxyfluorides in fluorine containing plasma environments.

5.3.2 Comparison of Y_2O_3 and YOF

To investigate the impact of surface fluorination on the erosion of Y_2O_3 the established re-localization technique was applied again. A model composite material was designed combining Y_2O_3 and yttrium oxyfluoride (YOF). Fluorine containing compounds like YOF were recently discussed as alternative etching resistant materials for fluorine based plasma applications. Several investigations showed a comparable or improved etch resistance of sintered YOF ceramics [13, 15, 178] or YOF coatings [16, 115, 179] compared to Y_2O_3 as a reference material system. The main difference between the two material systems is the different fluorination behaviour. In case of YOF, the lower potential of oxygen-fluorine exchange at the surface makes this material less prone to chemical degradation [13]. This behaviour is expected to reduce the risk of formation of fine particles, which is one of the most detrimental failure mechanisms during wafer processing. For investigating the potential of YOF on a fundamental level, Y_2O_3/YOF compounds with 20 w% YOF as a secondary phase were sintered by FAST/SPS (1500 °C, 50 MPa, 10 min) and subjected to a fluorine based etching plasma using the standard parameters (S150; Tab. 3.6). The investigation of composites allows a direct comparison of the erosion resistance of Y_2O_3 and YOF grains. Furthermore, the surface topography after plasma exposure enables to study the fluorine reaction behaviour of both materials in parallel and to conclude which material has the higher resistance against plasma erosion.the formed surface morphology of both compounds at the microscopic scale excluding any external effects. Furthermore, it will help to distinguish if erosion is dominated by physically driven material removal and chemically induced surface degradation.

The microstructure of Y_2O_3/YOF composites in the as-sintered state is displayed in

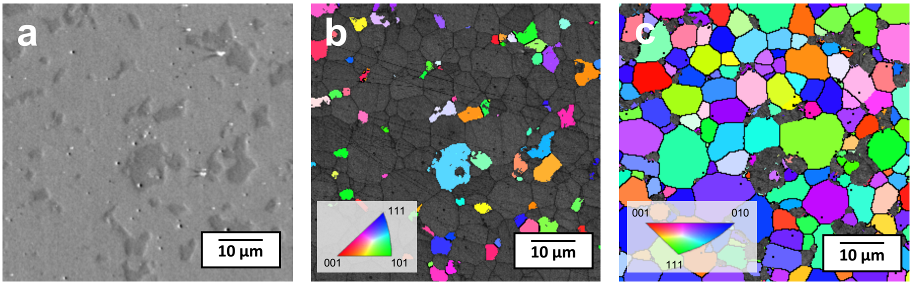

Fig. 5.22 Microstructure of Y_2O_3/YOF (80/20 w%) composites before plasma exposure. (a) SEM image of the surface. (b) EBSD mapping of the cubic YOF phase in the Z-direction (c) EBSD mapping of the cubic Y_2O_3 phase in the Z-direction. The corresponding IPF colour key is included in the image.

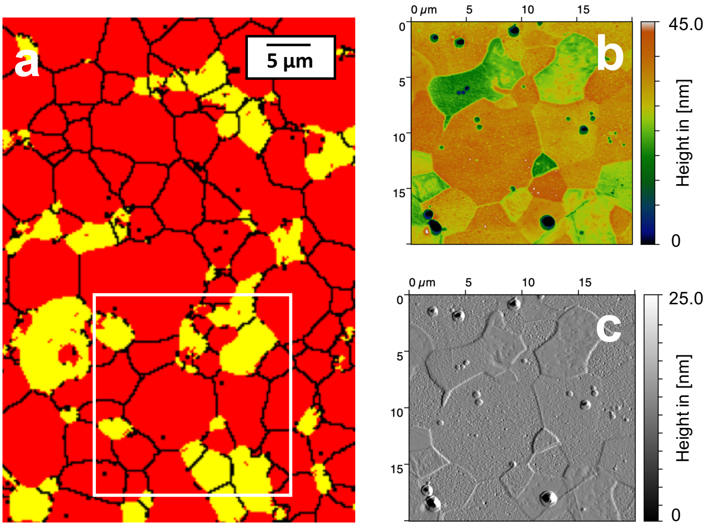

Fig. 5.23 Correlation of phase composition with surface morphology after plasma exposure. (a) EBSD phase mapping before the plasma exposure (red - Y_2O_3; yellow - YOF). (b) AFM topography scan of the surface after exposure. (c) AFM amplitude scan of the surface after exposure.

Fig. 5.22. Here, a SEM image of the surface as well as electron backscatter diffraction (EBSD) mappings of both phases are shown. The sintered composites had high relative densities and a low amount of residual porosity. Even though the powder preparation (mixing and homogenisation) was just done in a dry state using mortar and pestle, agglomeration of the secondary phase could be prevented, resulting in a homogenous distribution of YOF particles in the matrix. The orientation of surface grains in the Z-direction is displayed in Fig. 5.22 (b) and (c) indicating no preferential orientation of Y_2O_3 and YOF grains.

A first comparison of the phase distribution before plasma etching and the related surface topography after plasma exposure is given in Fig. 5.24. The microstructural re-localization after plasma exposure enables a correlation between YOF and Y_2O_3 grains with the morphology investigated by AFM. The direct comparison of YOF grains (yellow) and Y_2O_3 (red) clearly revealed the lower etch resistance of YOF. In the case of YOF, grains show a higher etching depth and inhomogeneous surface morphology. On the other hand, for Y_2O_3 grains the erosion behaviour discussed before was reproduced to a large extent. Depending on their crystallographic orientation, some grains showed a clearly improved resistance compared to YOF but other Y_2O_3 grains had comparable etching rates to YOF. In sum, the morphology of the sample surface after exposure was again dominated by the plateau-like topography which was extensively discussed in chapter 5.3.1.

To further investigate the different behaviour of Y_2O_3 and YOF, a detailed analysis of the AFM topography is given in Fig. 5.24. The derived line scans done on distinct positions (marked in red and black color in Fig. 5.24 (a)) confirmed the plateau-like

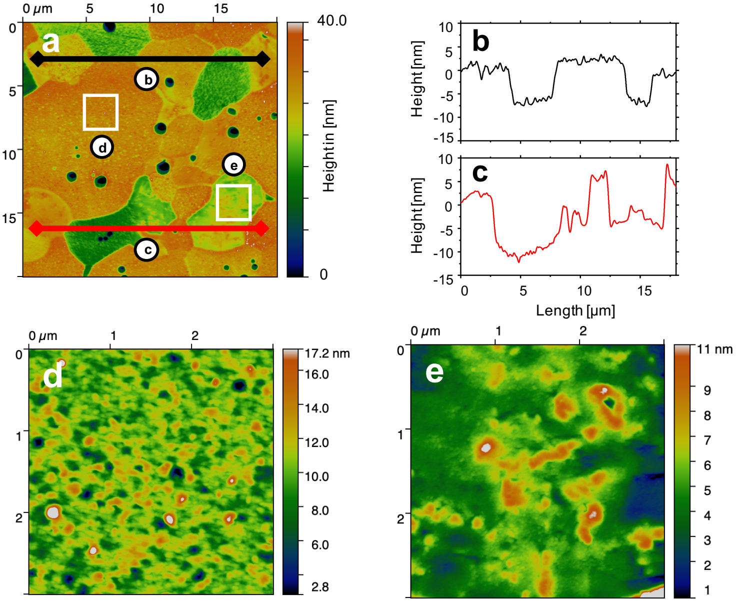

Fig. 5.24 AFM investigation of the surface morphology. (a) Overview AFM topography scan (b, c) Lines scans marked in (a). (d, e) AFM topography details of a resistant Y_2O_3 grain and a YOF grain with lower etch resistance.

topography which is present on the complete sample. The comparison between the surface morphology of a resistant Y_2O_3 grain (d) and a weaker YOF grain (e) hint on differences in the dominating etching mechanism. The nano-porous surface of the Y_2O_3 grain was characterized by a uniform and rough appearance, while the surface of YOF grain had a very inhomogeneous morphology. High local roughness peaks as well as holes were visible hinting at a non-uniform removal mechanism.

The comparison of microstructural features generated by the plasma exposure is very selective and includes only a limited amount of information due to the localized character of the investigation. Therefore, a correlation between the relative topographic height measured by AFM and the crystalline orientation was carried out. The data set representing the relative height of Y_2O_3 which was already presented in chapter 5.3.1 and will be used as a reference here, to elucidate the behaviour of YOF in fluorine based etching plasmas. Therefore, the relative topographic height h_r was calculated from several AFM scans and correlated to the crystallographic orientation represented by the Euler angels φ_1, ϕ and φ_2. The relative topographic height was determined by $h_r = {}^{h_i}/_{h_{max}}$, where h_i is the measured median height of the grain and h_{max} is the highest measured height in the corresponding AFM scan. This procedure helps to visualize and compare relative heights of Y_2O_3 and YOF derived from a multitude of AFM scans. For the comparison between both materials, a novel data set of 60 individual YOF grains was analysed and compared to the dataset related to Y_2O_3, which was already presented in Fig. 5.20. The correlation

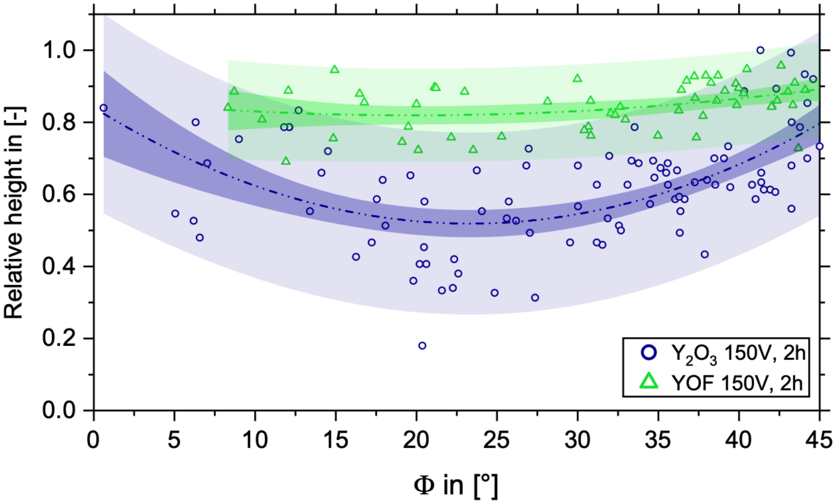

Fig. 5.25 Correlation of relative topographic AFM height after plasma exposure to the crystalline orientation represented through the Euler angle ϕ for Y_2O_3 (blue) and YOF (green).

of relative AFM heights for both materials is displayed in Fig. 5.25 using the second Euler angle ϕ, which represents a rotation of the (001) plane to (011) plane, where cubic Y_2O_3 undergoes a transition to lower ion transparency.

The correlation of topographic AFM height to the Euler angle ϕ for YOF grains does not show the characteristic orientation dependent behaviour, which was found for Y_2O_3. Even though YOF has a comparable crystal structure (cubic, $F\bar{4}3m$ [216]) and undergoes the same low ion transparency regime at angles of $\phi = 15 - 35°$, no measurable effect was observed. The investigated YOF grains exhibit relative topographic heights between 0.8 and 1.0, while the Y_2O_3 reference data set shows the characteristic height distribution with a minimum at angles around $\phi = 20 - 25°$. Despite having a comparable crystal structure, the orientation depending change of removal rate was not observed for YOF compounds. Due to the increased resistance against reaction with the deposited fluorocarbons, YOF grains are expected to be less vulnerable to chemical surface degradation. Nevertheless, the behaviour of YOF indicates that the orientation dependent surface phenomena observed for Y_2O_3 could be significantly influenced by the surface reaction mechanisms and the formation of a fluorine containing top layer. The direct comparison of Y_2O_3 and YOF grains strongly hints on a large impact of surface fluorination on the observed plateau-like topography in the case of Y_2O_3.

Therefore, SEM-EDS mappings were carried out on Y_2O_3/YOF composites after plasma exposure. The results are summarized in Fig. 5.26 showing the surface morphology as well as the EDS mappings for yttrium, oxygen and fluorine. Green arrows mark selected YOF grains in the microstructure and the related EDS mapping. While oxyfluoride grains exhibit an increased roughness and an intermediate relative etching depth, Y_2O_3 displays two types of erosion morphology: (I) Highly resistant grains exhibiting a nano-porous surface (II) Low plasma resistant grains exhibiting a smooth surface. The white arrows in the SEM image and the EDS mapping mark selected low resistant Y_2O_3 grains allowing a comparison of the chemical composition of YOF grains with Y_2O_3 grains of type (I). The analysis of the fluorine mapping revealed that selected Y_2O_3 grains of type (II) showed a very low fluorine intensity at the surface suggesting two distinguishable types of reaction pathways being active during the plasma erosion of Y_2O_3. In contrast, Y_2O_3 grains exhibiting a type (I) surface morphology reveal a higher fluorine content supporting conclusion on a different reaction mechanism. Not unexpected, the highest fluorine intensities were observed in YOF grains. The corresponding oxygen mapping (Fig. 5.26 (c)) additionally supports these observations, showing the highest oxygen intensities for yttria grains of type (II). The results confirm that the reaction layer formed during the exposure was strongly influenced by the grain orientation. This led to either a very low fluorine concentration at the surface, meaning a thin reaction layer or a high concentration which suggests a rather thick reaction layer.

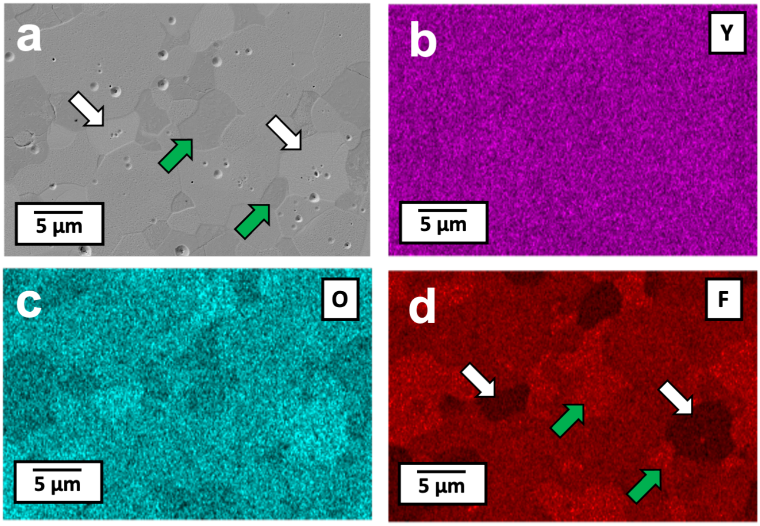

Fig. 5.26 SEM-EDS investigation of the chemical composition at the surface of Y_2O_3/YOF composites. (a) SE-SEM image showing the surface after plasma exposure. White arrows highlight Y_2O_3 grains having a smooth morphology and a low etching resistance. Green arrows mark selected YOF grains. (b) EDS Mapping showing displaying the intensity of Y. (c) EDS Mapping showing the intensity of O (d) EDS Mapping showing the intensity of F

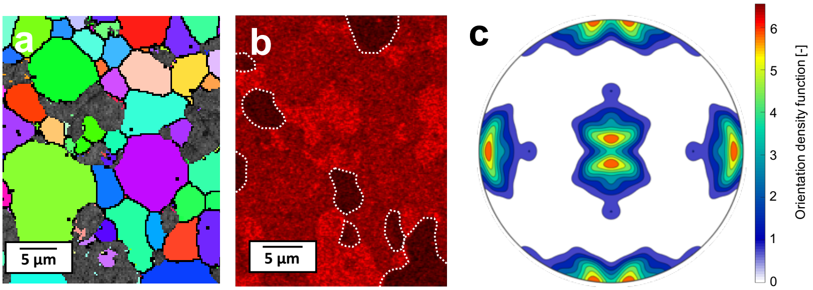

Fig. 5.27 Correlation between crystalline orientation and surface fluorination of Y_2O_3 after plasma exposure. (a) EBSD orientation mapping of Y_2O_3 grains in the Z-direction. (b) Corresponding SEM-EDS elemental mapping of F at the same position. (c) Orientation density function displayed in a spherical projection. Orientations of Y_2O_3 grains which exhibit a low surface fluorination after plasma exposure are displayed revealing a strong dependency of the surface reaction from the orientation.

To generate an increased understanding of the properties which control the fluorination mechanism in Y_2O_3, the crystalline orientation of Y_2O_3 grains showing a type (II) morphology was determined using a correlation between EBSD orientation data and EDS mappings. Re-localization of microstructural features enabled to determine the surface orientation of selected type (II) grains which was utilized to create a data set of grains with low fluorine content. Selected EBSD and EDS mappings illustrating the procedure and the orientations of grains with low fluorine intensity are displayed in Fig. 5.27. A stereographic projection is used to show the orientation density function of the data set, confirming the strong orientation dependency. Grain orientations near to the (001), (010) and (100) direction exhibited a low amount of fluorine at the surface as well as a reduced etch resistivity. At all other orientations a porous morphology and increased etch resistance was observed.

Additionally to the etch resistance and the degree of surface fluorination, the post etching morphology is highly dependent on the crystal orientation. A correlation between crystallographic properties and morphology is summarized in Fig. 5.28 showing the microstructure, crystallographic orientation and AFM topography of type (I) and type (II) grains. A clear distinction between both kinds of erosion mechanisms is possible by correlating crystallographic orientation with the surface morphology after plasma exposure. Grains having an orientation near the low index planes (001) showed a smooth surface in both SEM imaging and AFM investigation, which correlates with a low amount of fluorine at the surface. Vice versa all other crystalline directions showed a high fluorine content and a rough nano-porous surface morphology.

These observations clearly suggest a surface orientation dependent fluorocarbon layer deposition, which strongly influences the chemical degradation of the surface. The orientation of the lattice planes reaching to the surface has a direct influence on the surface energy γ_s, which controls various physical and chemical surface properties [180]. Surface energy and crystallographic order in the near-surface area are known to be main factors controlling the interaction with other gaseous, liquid or solid phases due to orientation dependent wetting and adsorption properties [180, 181]. Furthermore, chemical reactions taking place at the surface are depending strongly on the crystal orientation, which can be observed in the case of metal corrosion [182, 183, 184] or O_2 catalytic reactions on CeO_2 [185]. Furthermore, the relationship between crystalline orientation, surface energy and wettability is strongly pronounced in rare earth oxides, as reported for CeO_2 and Er_2O_3 [181]. Tam et al. compared the wetting behaviour of the three high index planes (001), (011) and (111) of CeO_2 and Er_2O_3, revealing that wetting properties behave inversely to the intrinsic surface energy. This means that the low surface energy of the most stable plane (111) leads to the highest wetting angles [181, 186]. Additionally, the (111) plane displays charge neutrality due to the arrangement of O-Ce-O atoms at the surface (Fig. 5.29 (b)), while the (001) plane has a charged surface. This is especially important for the adsorption and wetting of polar compounds like water [180, 181].

As wetting and adsorption are connected phenomena, a comparable mechanism

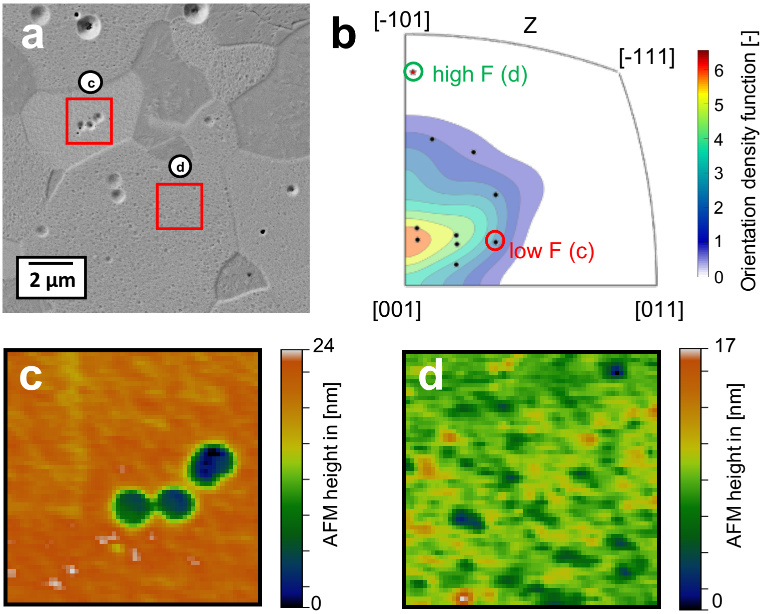

Fig. 5.28 Correlation between crystalline orientation, surface fluorination and morphology of Y_2O_3 after plasma exposure. (a) SE-SEM image of the surface after plasma exposure. Detail (c) highlights a grain with low plasma resistance and smooth morphology (Type II). Detail (d) highlights a grain with high plasma resistance and a nano-porous morphology (Type I). (b) Part of the spherical projection displayed in Fig. 5.27 showing the orientation of grains with a low amount of surface fluorination (black dots) and the orientation of a grain with high surface fluorination (red star). Red and green circles mark the orientations of the grains shown in (a). (c, d) AFM topography details.

could be the reason of the observed fluorination behaviour [180]. The chemical surface degradation during the plasma exposure strongly depends on the formation of the fluorocarbon film which is forming from fluorine containing radicals and molecules in the plasma [102, 187]. Larger fluorocarbon molecule chains are present in the reactive atmosphere of the plasma and adsorb to the surface of the ceramic substrate [188]. Hereby adsorption properties might become the controlling factor for the film formation. Assuming a comparable adsorption and wetting behaviour of Y_2O_3 and Er_2O_3, which share the same crystallographic and electronic structure, one could suggest that the film formation and the subsequent reaction with the substrate is strongly influenced by the crystalline orientation of the grain structure. Hereby, the poor wetting behaviour on surfaces near the (111) direction may lead to an inhomogeneous film formation characterized by a decreased amount of surface reactions. In contrast, the improved wettability of grains with an orientation near the (001) direction should lead to the formation of a homogenous and thin film, which facilitates an even fluorination of the yttria surface.

The continuous film deposition and material removal processes which are active during the exposure reinforce the different surface morphology formation. This led to rough nano-porous morphologies characterized by increased thickness and a high fluorine content on surfaces near the (111) orientation and thin reaction layers with low fluorine contents near (001). Due to the strong change of the removal process which is induced by the formed surface morphology, the etch rate and the material resistance are highly orientation dependent. The schematic representation of the proposed mechanism is displayed in Fig. 5.29 (c) showing the orientation dependent formation of the fluorocarbon layer which is heavily influencing the chemical degradation kinetics and therefore leading to varied etch rates and morphologies.

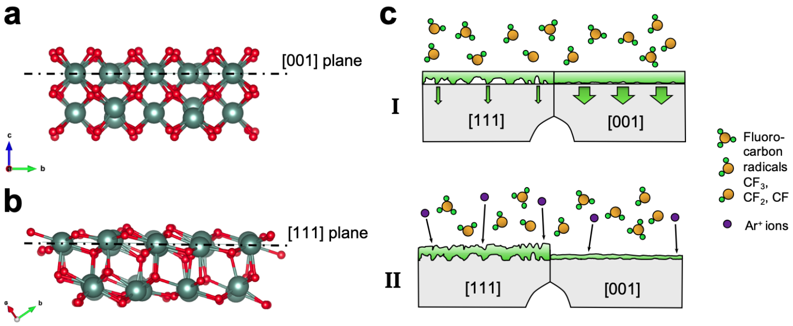

Fig. 5.29 Crystallographic structure at the surface and orientation dependent surface fluorination. (a) Crystallographic structure along the (001) plane of Y_2O_3. (b) Crystallographic structure along the (111) plane of Y_2O_3. (c) Schematic representation of the proposed orientation dependent surface fluorination mechanism. The fluorocarbon film formation is controlled by the adsorption properties of the surface (I) leading to a different chemical degradation and differing etch resistance (II).

6 Scientific and industrial implications and impact

In this thesis a broad variety of applied and fundamental results were achieved. Here, the main findings and conclusions will be discussed regarding their impact on an industrial application of Y_2O_3 ceramics as well as their scientific impact. First, the gained insights which have indications for an industrial application of FAST/SPS sintered Y_2O_3 ceramics will be discussed. Afterwards, the fundamental and application related observations made during the investigation on plasma-material interaction will be evaluated.

The direct processing of commercial Y_2O_3 powders using the FAST/SPS technology to sinter highly dense, lab-scale sized samples is of minor complexity. A larger processing window varying the temperature between 1400 and 1600 °C enabled to generate fully dense samples with diverse microstructures. A well defined combination of sintering temperature, dwell time and pressure can be used straightforward to tune the microstructure. Additionally, pre-processing of the commercial powders using planetary and roll bench milling was found to be another parameter to control the microstructure evolution during FAST/SPS.

However, scaling up the sample size to dimensions relevant for industrial applications caused new challenges, which complicate the production of homogeneous and highly dense Y_2O_3 components via FAST/SPS. For demonstrating the scaling up from lab to pilot scale, a hybrid FAST/SPS sintering facility was used and the maximal sample size was increased to 100 mm. The main challenge was an inhomogeneous temperature distribution in the tool setup caused by uneven energy dissipation in the conductive tools through Joule heating (Fig. 2.13 (c)). Major parts of the generated heat get dissipated near the rim of the sample leading to overheating at the edge of the sample while inner parts exhibited to lower temperatures. The application of CFC spacers which act as a thermal insulator inside the tool setup can decrease the heat loss at the water cooled electrodes and therefore improve the temperature distribution and efficiency of heat dissipation in the centre of the tool. It was shown that the position of CFC spacers only has a minor impact on sintering and grain growth but a complete removal leads to detrimental heat loss and prevented the realization of the sintering cycle within the parameter window mentioned before. However, experiments on pilot scale already showed that FEM simulation of current and temperature distribution are highly recommended for better controlling FAST/SPS of large ceramic parts. The preliminary FEM done in this work clearly demonstrated the large potential of this modelling approach for tool design and sintering parameter optimization.

Other challenges of the FAST/SPS technology are the single batch processing and the limited flexibility of sample design. The graphite powder bed assisted SPS technique, which was introduced for single samples by Hocquet et al. [133], was applied for sintering several complex shaped Y_2O_3 samples (here up to six) at once.

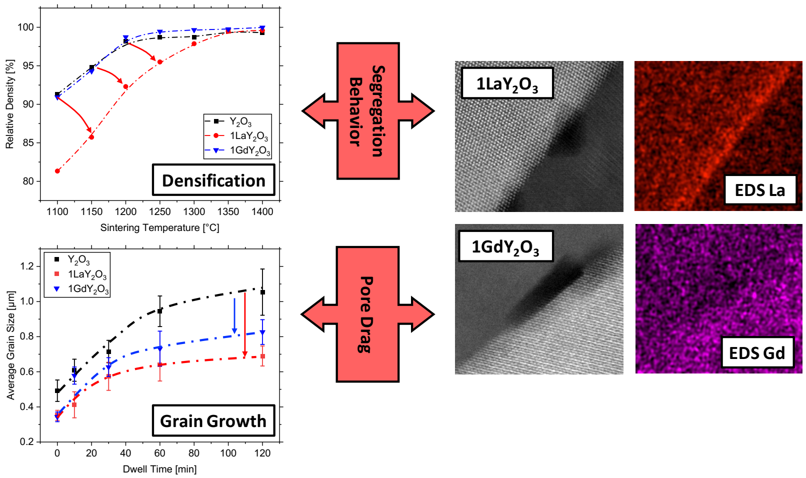

Fig. 6.1 Correlation between the densification and grain growth kinetics during FAST/SPS sintering of pure and La^{3+} and Gd^{3+} doped Y_2O_3. The corresponding high resolution HAADF images and EDS mappings show a segregation of La atoms to the interface due to its ionic size mismatch with the host lattice. Both solute drag and Zener pinning of a dopant induced interfacial nano-porosity led to a stepwise reduction of the grain boundary mobility in doped yttria.

This approach combines the possibility to increase the complexity of the sample geometry and at the same time allows to process several samples in parallel. The powder bed assisted FAST/SPS processing route could facilitate the fabrication of net-shaped components which could not be processed by FAST/SPS before. However, further optimization of the processing conditions (green body, powder bed, sintering parameters) has to be conducted to achieve sample qualities comparable to conventionally FAST/SPS sintered materials. Im sum, optimized tool design by applying CFC spacers as well as powder bed assisted FAST/SPS are promising approaches to bring FAST/SPS a step forward regarding its industrialization.

Also the sintering of Y_2O_3 has been optimized by rare earth doping. La and Gd from the lanthanide group were selected since they are tolerable elements with respect to the strict specifications of semiconductor industry. Here, it was demonstrated that both cations can be used to optimize the densification as well as to limit the grain growth in the final stage of sintering. Especially the segregation of La cations due to their ionic size mismatch can reduce the grain boundary migration rates at high temperatures by solute drag. The segregation of cations to the grain boundary was investigated using high resolution transmission electron microscopy revealing the different behaviour of La and Gd cations. A direct correlation between the chemical composition at the grain boundary and the densification and grain growth kinetics was found, revealing fundamental relationships controlling boundary migration at high temperatures (Fig. 6.1).

Results of this fundamental study can be applied to design optimized dopant strategies

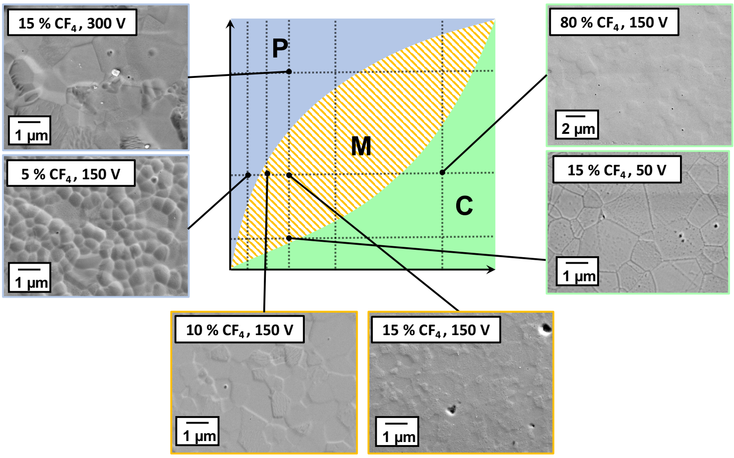

Fig. 6.2 Plasma processing map displaying the dominating erosion mechanisms for Y_2O_3 under varied plasma parameters (P-physical, M-mixed, C-chemical erosion). Additional SEM images of Y_2O_3 samples exposed to different plasma etching parameters are displayed to highlight the strong influence of the active mechanism onto the erosion behaviour as well as the formed morphology (Parameters as indicated).

for consolidating highly dense, fine grained Y_2O_3 components using FAST/SPS. Hereby, the atomic properties of the cations can be utilized to predict their influence on the sintering and grain growth kinetics enabling the development of components with improved properties in contact with reactive etching plasmas.

Another important aspect from an industrial perspective is the plasma-material interaction in fluorine based etching plasmas. Especially the thorough understanding of the impact of surface defects which are induced by insufficient densification or surface machining, is the basis to design Y_2O_3 components with optimal properties. Erosion was most pronounced at sharp edges of surface defects like residual pores, scratches and breakouts. These observations clearly reveal that even small amounts of surface defects can lead to severe erosion at certain spots of the microstructure. Reducing the amount of residual porosity and a thorough surface finishing by polishing were found to be prerequisite for components being applied in plasma etching devices. Additionally, a more general understanding of the different processing regimes was developed during this PhD study. The schematic processing map constructed by the two main parameters Ar:CF_4 ratio and DC bias voltage is repeated in Fig. 6.2 supplemented by the different characteristic surface topographies induced by the dominant erosion mechanism. The erosion behaviour of polycrystalline ceramics, which form non-volatile reaction products, can be roughly divided into three mechanisms: Physical (P), mixed (M) and chemical (C) erosion. The investigated processing regimes are specific for polycrystalline Y_2O_3 but can be transferred to other ceramic materials, which form a non-volatile reaction product. An application of this experimental framework to other ceramic compounds could be helpful to benchmark their performance during plasma exposure. The knowledge about strengths and weaknesses of the exposed material depending on the processing parameters allows to select the preferred material for specific etching conditions based on their erosion behaviour. Furthermore, investigating the material response on the basis of a profound understanding of the process regimes allows to develop novel materials by adapting the experimental strategy used in this work.

Next to applied research questions, experiments on the fundamental relationships of plasma erosion behaviour revealed the main material properties controlling the plasma erosion behaviour. Re-localization of microstructural features and a multimodal characterization allowed to connect the morphological changes induced by the plasma attack to the crystalline orientation of surface grains. For the first time, the erosion mechanisms in the mixed physicochemical regime were described and an orientation dependent chemical fluorination and removal process was found. This behaviour is comparable to orientation dependent corrosion mechanisms which have been described for different metals and alloys. The first clear description of the physicochemical erosion process of Y_2O_3 could be the starting point for a more general understanding of the erosion of polycrystalline ceramics under plasma conditions. Various material combinations are applied under these extreme conditions and only superficial descriptions of the active erosion mechanisms have been described for ceramics like Al_2O_3, YAG, SiC and AlN. The applied approach, which was developed in this work, could be transferred to various other ceramic materials to reveal general relationships or material specific behaviours. The hereby generated understanding of the erosion behaviour of ceramic materials could be helpful to lay the groundwork for further research into the erosion behaviour as well as novel applications of ceramics in plasma etching environments.

7 Conclusions and Outlook

Y_2O_3 is a highly promising material for protective components inside plasma etching devices for manufacturing processes in the semiconductor industry. However, low sinterability and high production costs have prevented an application of bulk Y_2O_3 components so far. During this work, FAST/SPS was investigated as a new processing route to sinter high quality, bulk ceramic components. Besides sintering studies, fundamental and applied questions concerning the plasma-material interaction between FAST/SPS sintered Y_2O_3 and fluorine based etching plasma were investigated.

The scientific questions in this work are divided into two main thematic complexes: Firstly, a comprehensive processing study of Y_2O_3 using field assisted sintering (FAST/SPS), secondly a fundamental study of the material-plasma interaction of Y_2O_3 based materials in contact with fluorine based etching plasmas.

The investigations on FAST/SPS of Y_2O_3 focused on application related topics concerning the direct processability of commercial powders, microstructure control by parameter optimization and challenges coupled with upscaling. Direct one-step processing of three different commercial powders in the as delivered state was possible without further powder processing steps and a parameter variation between 1400 and 1600 °C proved the excellent possibility of microstructure control through accurate choice of FAST/SPS parameters. Optional microstructure development could be further improved by ball milling the starting powders. Decreasing the initial particle size did not influence the sintering behaviour during FAST/SPS but could reduce the final average grain size compared to commercial powders. However, additional powder processing induced further chemical impurities due to abrasive wear from the milling media and crucibles. Therefore, a compromise between high chemical purity and optimized particle properties has to be found depending on the material requirements for the distinct application.

The possibilities and challenges of scaling up sample size and realizing complex sample geometries were investigated using a hybrid FAST/SPS facility and pressing tools up to 100 mm in diameter. One major issue arising during scale up was the formation of thermal gradients inside the tools. Positioning additional CFC spacers in the graphite tool, which act as internal thermal insulator, improved the temperature distribution during FAST/SPS. The influence of different spacer positions was investigated by linking microstructural characterization of the sintered samples and FEM modelling of the thermal fields. Both experimental and simulation results showed a minor effect of the CFC spacer positioning, only slightly changing the temperature gradient occurring during sintering. However, reference experiments done without the application of CFC spacers to the tool setup failed due to high thermal losses and overheating of the SPS power source, demonstrating the importance of accurate thermal management when scaling up sample sizes.

So far, limitations with respect to the processing of complex shaped samples by FAST/SPS was one of the major drawbacks impeding further industrialization. Therefore, powder bed assisted FAST/SPS was investigated to consolidate complex shaped Y_2O_3 samples. For demonstration, six gear-shaped Y_2O_3 components were sintered in parallel in a 100 mm graphite tool. The application of different graphite powder beds with coarse and fine powder morphology was found to be an important parameter to improve the densification. Even if the results are still preliminary, sintering with optimized parameters showed promising results concerning the densification and shape stability. However, further process optimization (green body, powder bed characteristics, FAST/SPS parameters) is needed to establish this technique on an industrial scale.

In addition to this applied processing study the impact of rare earth doping on sintering and grain growth during FAST/SPS of Y_2O_3 was investigated on a fundamental level. It was observed that the densification and coarsening kinetics directly correlate to the kind of doping as well as the physical structure of the grain boundary. Therefore, pure, 1mol% La and 1mol% Gd doped Y_2O_3 compounds were sintered and characterized. A clear correlation between the ionic radius of the dopant species and their segregation was observed which had significant influence on the sintering and grain growth kinetics. Segregation of La cations on the grain boundaries induced a characteristic solute drag effect slowing down the grain boundary movement during final densification, preventing detrimental pore detachment and therefore allowing continued removal of porosity. However, segregation of cations to the grain boundary also seemed to decelerate cation diffusion along the interface which is the rate controlling mechanism for densification during FAST/SPS sintering. These fundamental insights into the segregation behaviour of rare earth dopants provided a powerful tool to understand the effects of applied dopants and thereby optimizing the processing of ceramic components, qualifying them for application in plasma etching devices in semiconductor industry.

The second important topic of this work dealt with the plasma-material interaction of Y_2O_3 ceramics with fluorine based etching plasmas. Here, the fundamental characterization was divided in three parts focusing on processing induced defects, plasma parameter influence and the clarification of the intrinsic mechanisms controlling the plasma erosion of polycrystalline Y_2O_3. First, the influence of processing induced defects like residual porosity at the surface, high roughness due to insufficient sample machining and cracks were considered. The presence of sharp edges or rough surface topography were the main driving factors for accelerated material removal during the plasma exposure due to their preferred erosion. This behaviour was generally observed for all processing induced surface defects and preventing them to a large extent is an absolute must for the application of ceramic materials in plasma environments. Furthermore, a phenomenological processing map describing the material erosion behaviour dependent on the plasma parameters was developed through systematic variation of plasma gas composition and applied DC bias voltage. The material erosion can be divided into three distinctive regimes which are dominated by mainly physical or mainly chemical interaction or by a mixed mechanism. The etching rate as well as the generated surface topography were strongly influenced by the active processing regime. A physically dominated plasma erosion shows the highest etching rates as well as a strong surface damage. In this case, material removal is almost independent from the grain orientation. In the mixed processing regime the erosion is characterized by the formation of a orientation dependent surface topography. Here, a clear relationship between surface fluorination and grain orientation was found, which caused an inhomogeneous erosion of single grains and a surface topography representing the initial grain structure. In the chemically dominated processing regime, etching rates drop to a minimum due to the formation of a stable reaction layer which cannot be removed by the low amount of active Ar ions present in the plasma atmosphere. The low removal rates led to a saturation of the near surface area with yttrium oxyfluorides, almost completely stopping the erosion process.

Finally, the active erosion mechanism in the mixed processing regime was investigated by applying a straightforward re-localization technique which allows to correlate microstructural features and properties before and after the exposure. This enables to understand the observed intrinsic relationship between the grain orientation at the surface and the formation of the plateau-like topography. A physicochemical mechanism, which is foremost dominated by the orientation dependent fluorination of the surface, controls the interaction between the deposited fluorocarbons and the surface grains. Additional to the chemical interaction, the sputtering yield also shows an orientation dependency leading to higher physical sputtering rates for selected orientations. These observations were confirmed by the direct comparison of the etching behaviour of Y_2O_3 grains with stoichiometric oxyfluoride YOF grains at the microscopic scale. Therefore, a composite material consisting of Y_2O_3 and 20 w% YOF was made by FAST/SPS. Y_2O_3 grains again exhibited a grain orientaion dependent erosion, confirming the former results. In contrast, YOF is not prone to a chemical degradation caused by deposited fluorocarbons, therefore an orientation dependent mechanisms was not present, which further highlights the strong impact of surface fluorination on the erosion mechanism.

In this work, several applied and fundamental research questions were addressed dealing with the FAST/SPS processing of Y_2O_3 ceramics and their suitability for being used in plasma etching devices in the semiconductor industry. The results significantly contribute to establish bulk Y_2O_3 ceramics processed by FAST/SPS for this application. The results can be used in general for the development of plasma resistant materials and components for the next generation of plasma etching devices. However, some topics have only been touched superficially and were not addressed in a thorough manner. They are of high interest and would further extend the understanding of both sintering and plasma-material interaction of ceramic materials. Therefore, three major directions of research are recommended for future studies:

- Optimizing the processing conditions during the FAST/SPS sintering of large scale and complex shaped ceramic components: This research topic includes the combination of process control and FEM simulation as well as the development of tailored materials/starting powders which are optimized for manufacturing of large sample sizes. Additionally, powder bed assisted FAST/SPS sintering offers a large optimization potential for the production of complex shaped ceramic components.

- Applying the fundamental understanding of cation segregation to a broader spectrum of cations for tailoring the processing and material properties of Y_2O_3: Hereby, systematic change of ionic size mismatch and a transfer of this effect to cations, which also show a charge mismatch, is of high interest.

- Expanding the re-localization technique to doped Y_2O_3 and other material systems (oxides, carbides): The research strategy - successfully developed on the example of Y_2O_3 in the present work - could be transferred to other materials systems of interest for the semiconductor industry, allowing to gain an even more general understanding of the fundamental mechanisms of plasma erosion and enabling to develop strategies for further tailoring materials for etching applications.

All of these suggested research topics could open up new industrial applications for ceramics processed by FAST/SPS as well as lead to a more complete understanding of erosion and degradation mechanisms under extreme chemical and physical conditions.

Acknowledgements

Within a glimpse, three years passed and I'm looking back on the time of my doctoral thesis with great joy, being thankful for all the friends I've made, all the things I've learned and all the problems I've overcome. Achieving this would not have possible without the genuine help and support of some many people. This will be a bold approach to include all of them in one short chapter.

First, I would like to thank my doctoral supervisor Prof. Dr. Olivier Guillon for giving me the chance to pursue my doctoral research in such an ambitious project at Forschungszentrum Jülich. He gave me the freedom to follow my own ideas and provided excellent scientific support when it was needed. All of the international conferences and the scientific research stay at the National Institute for Material Science in Japan would not have been possible without his support.

Secondly, I would like to show my sincere thanks to my scientific supervisor Prof. Dr. Martin Bram, who always had an open door for all my questions, scientific ideas (good or bad), requests for feedback and everything else. Thank you for your ongoing support and all the guidance that you gave me during the last three years.

The doctoral thesis you hold in your hands would not have been possible without the sincere help and support from many colleagues from IEK-1, Forschungszentum Jülich and other universities. Therefore, I would like to thank: Dr. Doris Sebold and Beatrix Göths for their countless SEM investigations, Dr. Nino Schön and Moritz Weber for the great times behind the AFM at IEK-9 and PGI-7, you both helped me so much, Dr. Marcin Rasinski for his help with FIB-SEM and sparking a lot of ideas on plasma-material interaction, Sigrid Schwartz-Lückge and Andreas Hilgers for powder analysis, Dr. Yoo Jung Sohn for her help with XRD and discussions on stereographic projections and the confusing world of crystallography, Prof. Dr. Alexander Laptev for his FEM simulations, Prof. Dr. Jesus Gonzalez-Julian for his continued feedback on my work and great scientific discussion, Dr. Ke Ran and Prof. Dr. Joachim Mayer for their help in organizing and taking amazing STEM images of my samples, Dr. Mark Stamminger and Rahel Buschhaus for their continued help etching my samples at the RUB, Dr. Uwe Breuer for characterizing the chemical gradients in my samples using TOF-SIMS, Dr. Egbert Wessel for making EBSD scans of several of my samples and therefore enabling a deeper insight into the etching mechanism and Dr. Michael Weißmayer for his continued feedback and motivation. Without all of you my work would not be as broad and thorough as it turned out to be.

My sincere thanks also goes to all the colleagues at NIMS, which allowed me to stay in Japan for three months during the humid late summer of 2019. This experience was unforgettable and I will dwell on the memories for a long time. First, I would like to thank Dr. Koji Morita for organizing everything and making me feel so welcome at NIMS. Furthermore, I would like to thank Prof. Dr. Hidehiro Yoshida for opening his lab for my experiments and the discussions on flash sintering and Kotha Nambu for his help operating the flash furnace. Your help was highly appreciated!

Next to scientific discussions and help with various characterization techniques, I also made a lot of friends at IEK-1, which made working on my PhD thesis just like hanging out with friends. First and foremost I have to thank Dr. Tobias Kalfhaus and Dr. Fabian Grimm for establishing the breakthrough gang, ridiculously often ringing the breakthrough bell and hectolitres of coffee, which we consumed during our time. It was a blast! Secondly, huge thanks goes out to the sintering gang (Dr. João Gustavo Pereira da Silva, Dr. Tarini Mishra and Dr. Chen Cao) for scientific discussions and coffee coffee coffee. Additional thanks go to Dr. Apurv Dash and Dr. Tu Lan for the great time in our shared office and the great scientific discussions. Finally I have to thank the IEK-1 boulder and climbing squad with whom I shared tons of hours in the gym and at the crag: Dr. Christoph Vorkötter, Walter Scheld, Martin Ihrig, Jörn Faul, Jürgen Gross, Dr. Markus Wolf and Dr. Michael Küpers.
Next to all the scientific work which was a huge part of my life the last years, I'm deeply thankful for all my friends scattered around Germany. You pull me out of my mainly mono thematic life and really help me to cope with all of the struggle that working in science brings with it. I cannot name all of you here but big hugs go to: Fab, Basti, Flo, Andi (especially for designing the great cover!), Laura, Swantje, Chris, Jo, Passi, Max and all the others in Leipzig, Berlin, Stuttgart, München and Chemnitz ! <3
Special thanks and a lots of love goes to Luisa! You mean so much to me and with you everything is just better, greater and plain and simple amazing. Thank you for everything!
Zu guter Letzt geht mein unendlich großer Dank an meine Familie, die mich immer 100 % unterstützt hat, mir dauerhaften und festen Rückhalt gegeben hat, wenn ich ihn gebraucht habe, und immer für mich da ist. Ich bin meinen Eltern Wolfgang und Sabine sehr dankbar, dass ich in einer so bildungspositiven Familie aufwachsen und erwachsen werden durfte, welche nie den Zweck und Sinn von Bildung und Ausbildung hinterfragt hat und mich und meine Brüder immer in allen unseren Entscheidungen unterstützt und bekräftigt hat. Ich habe gelernt, dass so etwas keine Selbstverständlichkeit ist! Tausend Dank geht auch an meine Brüder Max, Felix und Rainer die immer für mich da sind, egal um was es geht und meine Großeltern die schon sehr früh mein Interesse an Wissenschaft gefüttert haben.

Danke für alles!

List of Figures

1.1 Historical development of the number of transistors on a microchip which is in general referred to as Moore's law. Graph adapted from [5]. 1

2.1 Crystal structure of Y_2O_3. 5
2.2 Major applications of Y_2O_3 ceramics. 6
2.3 Schematic visualization of coarsening and densification mechanisms which occur during sintering. Both processes are induced by the reduction of Gibbs free energy, which is the main driving force in solid state sintering. Adapted from [37] 7
2.4 Representation of a characteristic densification curve in a relative density - sintering time diagram and the associated stages of sintering. Adapted from [37] and [38] 8
2.5 Schematic sketch of the sintering mechanisms leading to neck formation and grain coarsening (1-3) and shrinkage (4-6) in the three particle model. (1) Surface diffusion (2) Lattice diffusion from the surface (3) Evaporation and re-condensation (4) Grain boundary diffusion (5) Lattice diffusion from the grain boundary (6) Plastic flow through dislocations. Adapted from [36]. 10
2.6 Equilibrium shape of a pore at the triple boundary of three grains. The relationship between the interfacial forces of the grain boundary and the surface-vapour interface are represented through the dihedral angle Ψ. Adapted from [36]. 11
2.7 General mechanism of grain growth. Atoms are migrating from their host lattice to a lower energy lattice position in the adjacent gain, moving the grain boundary in the opposite direction towards the curvature of the smaller grain. Graph adapted from [36]. 14
2.8 Theoretical consideration of a two dimensional cross section through a theoretical dense microstructure with $\Psi = 120°$. The curvature of the grains is determined by the number of sides leading to convex (n<6) and concave grain boundaries (n>6), which determines the local direction of boundary migration. Graph adapted from [36]. 15
2.9 Schematic sketch showing a migrating grain boundary interfering with an inclusion and the resulting forces derived from the geometric relationships of Zener pinning. Graph adapted from [36]. 18
2.10 Schematic behaviour of a solute cloud of segregated dopant atoms. (I) Symmetric concentration gradient in the stationary condition (II) Asymmetric concentration gradient of the solute cloud surrounding a migrating grain boundary. Solute drag is acting upon the moving interface reducing its overall velocity. (II) Breakaway of the solute cloud at high grain boundary velocities. Graph adapted from [36]. . . 19

2.11 Grain boundary mobility for a broad variety of doping elements with different valency. All compositions use a dopant concentration of 1 mol%. Taken from [57]. 22
2.12 Densification behaviour for a broad variety of doping elements with different valency. All compositions use a dopant concentration of 1 mol%. Taken from [66]. 23
2.13 Schematic sketch of a FAST/SPS sintering facility (a) and the material dependent current flow. Powders with a high (b) and low electronic conductivity (c) strongly influence the current flow and current density in the tool setup. (1) Uniaxial pressure via a hydraulic system (2) Water cooled steel electrode (3) Optional CFC spacer (4) Axial pyrometer (5) Graphite felt insulation (6) Sample (7) Graphite pressing die (8) Graphite pressing punch (9) Vacuum chamber (10) Electric pulse generator (11) DC power source. 24
2.14 Fluorocarbon polymer layer deposition mechanisms during the reactive plasma etching with CF_4 as the reactant. (1/4) Fluorocarbon radical deposition through adsorption. (2) Direct reaction of fluorine atoms with the polymer layer. (3) Physical sputtering of the polymer layer by accelerated ions. Graph adapted from [100]. 29
2.15 Schematic sketch describing the surface erosion mechanism of Y_2O_3 in reactive fluorine based plasmas after Miwa et al. [8]. (I) The fluorocarbon radicals and molecules present in the plasma chamber from a thin polymer layer (Fig. 2.14) (II) Plasma activation breaks Y-O bonds and allows fluorination (III) A chemical gradient is forming at the surface consisting of yttrium oxyfluorides (YO_XF_Y) which is leading to the removal of surface material. 31

3.1 FAST/SPS tool set-ups to investigate the influence of the CFC spacer position on the sintering of large scale yttria ceramics. (a) CFC spacers at all positions. (b) CFC spacers at the electrodes. (c) CFC spacer near to the sample. (d) Segmentation procedure for density and microstructure investigation. (1) Steel electrode, (2) Optical pyrometer, (3) Graphite felt insulation, (4) Sample, (5) CFC spacer. . 38
3.2 FAST/SPS tool set-ups to investigate graphite powder bed sintering of simple and complex geometries. (a) Tool setup used for preliminary sintering experiments with a pellet shaped sample geometry (b) Top view image of the arrangement of gear-shaped Y_2O_3 samples inside a 100 mm graphite tool (c) Tool setup used for the powder bed sintering of complex shaped samples. (1) Graphite felt insulation (2) Graphite pressing tool (3) Ceramic green body (4) Graphite powder bed (5) Complex shaped Y_2O_3 sample. 39
3.3 Schematic sketch of the experimental ICP plasma etching chamber at the RUB. (1) Custom made sample holder for FAST/SPS sintered Y_2O_3 samples (2) Gas inlet (3) DC self-bias (4) Protection window (5) ICP-generator (6) Vacuum pump (7) Sample cooling system. . . 42

3.4 Schematic sketch of the re-localization technique using Vickers hardness indents as markers and the applied characterization techniques before (left) and after plasma etching (right). 44
3.5 Working principle and formation of orientation dependent Kikuchi patterns in electron backscatter diffraction (EBSD). (a) Schematic sketch showing the diffraction of the electron beam by a 70 °tilted sample and the formation of Kikuchi lines on a phosphorus screen. (1) Kikuchi lines (2) Phosphor screen (3) Cone of intense electrons (4) Electron beam (5) Diffracting plane (6) tilted specimen (b) Example image of a Kikuchi pattern of Cd at 20 kV. Graph and image taken from [118]. 45
3.6 Working principle of an atomic force microscope. (a) Schematic of a AFM setup (1) Cantilever with nano-tip (2) Laser (3) Sample (4) Light microscope (5) Photodiode (6) PC control and analysis. (b) Force distance relationship acting onto the nano-sized tip. 48

4.1 Particle size distribution of commercial powders measured by laser granulometry. (a) PJ2. (b) Treibacher AG. (c) H.C. Starck Grade B. 51
4.2 SEM overview images of the powder morphology. (a) PJ2. (b) Treibacher AG. (c) H.C. Starck Grade B. 53
4.3 Bright field TEM images of a powder agglomerate displaying the primary particles. (a) PJ2. (b) Treibacher AG. (c) H.C. Starck Grade B. 53
4.4 SEM overview images of the powder morphology of PJ2 powders after milling in a planetary mill for different time durations. (a) unmilled. (b) 30 min. (c) 60 min. (d) 90 min. (e) 120 min. 54
4.5 Particle size distribution of PJ2 powders after milling in a planetary mill for different time durations measured by laser granulometry. (a) unmilled. (b) 30 min. (c) 60 min. (d) 90 min. (e) 120 min. 55
4.6 XRD diffraction pattern of PJ2 powder after milling for 30 min in a planetary mill. The inserted figure shows the diffraction pattern at low angles in higher magnification indicating the presence of impurities. 56
4.7 Sintering behaviour of milled powders investigated by dilatometry (left, 1500 °C, 1 h, 5 K/min), conventional sintering (right, 1600 °C, 2 h, 5 K/min) and FAST/SPS (right, 1300 °C, 10 min, 100 K/min, 50 MPa). 58
4.8 Development of average grain size and micro hardness as a function of the sintering temperature during the FAST/SPS sintering of different commercial Y_2O_3 powders. 59
4.9 angle=90,origin=c 60

4.10 Development of the average grain size and the microstructure of milled PJ2 powders after the FAST/SPS sintering at 1500 °C for 10 min under 50 MPa uniaxial pressure. (a) Average grain size development as a function of milling time (b-f) Corresponding SEM images showing the influence of milling on the final microstructure. All samples show a comparable relative density (see Fig. 4.7). 61

4.11 Development of the relative density along the diameter of a FAST/SPS sintered Y_2O_3 sample (1400 °C; 30 min; 30 MPa; 25 K/min) with changed tool setups. (a) CFC spacers at both positions (b) CFC spacers at the electrode (c) CFC spacers near to the sample. 63

4.12 Development of the average grain size along the diameter of a FAST/SPS sintered Y_2O_3 sample (1400 °C; 30 min; 30 MPa; 25 K/min) with changed tool setups. (a) CFC spacers at both positions (b) CFC spacers at the electrode (c) CFC spacers near the sample. 63

4.13 FEM modelling results displaying the temperature distribution inside the tool setup using different CFC spacer configurations. The thermal field is displayed at the beginning of the dwell time at 1400 °C. (a) CFC spacers at both positions (b) CFC spacers at the electrode (c) CFC spacers near the sample. 64

4.14 FEM modelling results showing the thermal distribution inside the sample using different CFC spacer configurations. The thermal field is displayed at the beginning of the dwell time at 1400 °C. (a) CFC spacers at both positions (b) CFC spacers at the electrode (c) CFC spacers near the sample. 65

4.15 Parameter study on FAST/SPS of Y_2O_3 green bodies in a graphite powder bed. (a) Relative density of sintered samples depending on uniaxial pressure (20 - 50 MPa) and sintering temperature (1400 - 1600 °C) (b) Visual appearance of samples after sintering in a powder bed. (top) 20 MPa (bottom) 50 MPa (c-h) SEM images of the microstructure using a uniaxial pressures of 20 MPa (top) and 50 MPa (bottom). . 66

4.16 Sintering of complex shaped Y_2O_3 components using graphite powder bed sintering. (a) Relative density of the sintered bodies measured by Archimedes principle. (b) Visual appearance of the gear-shaped Y_2O_3 samples before and after powder bed sintering. (c) Sample positions investigated by SEM. 67

4.17 SEM investigation of the microstructure at different positions along the diameter of the complex shape (Fig. 4.16 (c)). 69

4.18 (left) Development of the relative density as a function of the sintering temperature during FAST/SPS processing of doped and undoped Y_2O_3. (right) Development of the average grain size during FAST/SPS densification. The dwell time of 10 min and the applied pressure of 50 MPa are constant for all experiments. Lines are added to guide the eye. 71

4.19 Development of average grain size as a function of the relative density during FAST/SPS. The dwell time of 10 min and the applied pressure of 50 MPa were constant in all experiments. Lines are added to guide the eye. 72
4.20 Grain growth behaviour of pure and doped Y_2O_3 during FAST/SPS sintering at 1400 °C. (left) Development of the average grain size dependent on the dwell time at 1400 °C. Lines are added to guide the eye. (right) Linear fitting of the grain growth assuming $n = 2$. The grain growth constant K is derived from the slope of the linear fit. . . 73
4.21 Grain growth of pre-densified pure and La doped Y_2O_3 in air. (left) SEM images of the microstructure before and after thermal annealing at 1500 °C for 10h. (right) grain growth constant K for temperatures from 1400 °C to 1600 °C displayed in an Arrhenius plot. 74
4.22 Overview HAADF-STEM images showing grain boundaries in (a) pure Y_2O_3 (b) 1 mol% LaY_2O_3 (c) 1 mol% GdY_2O_3 sintered by FAST/SPS (1400 °C; 50 MPa; 120 min, 100K/min). Structural defects at the grain boundary are marked by arrows. 74
4.23 High resolution HAADF-STEM images of pure Y_2O_3 sintered by FAST/SPS. (a) Clean grain boundary showing no structural defects or amorphous interfacial films. (b-c) Overview and detail STEM-EDS mappings showing the elemental distribution of Yttrium and Oxygen at the interface. 75
4.24 High resolution HAADF-STEM images of La and Gd doped Y_2O_3 sintered by FAST/SPS. (a) HAADF image of a grain boundary in 1 mol% LaY_2O_3 showing no structural changes and intergranular films at the grain boundary. (b) EDS mapping displaying the chemical composition at the interface in 1 mol% LaY_2O_3. (c) HAADF image of a grain boundary in 1 mol% GdY_2O_3. (d) EDS mapping displaying the chemical composition at the interface in 1 mol% GdY_2O_3. (e) EDS line scan taken from the HAADF image in (b) highlighting La segregation at the grain boundary (e) EDS line scan taken from the HAADF image in (d) highlighting even Gd distribution across the grain boundary. 76
4.25 STEM-EDS investigation on a nano pore in 1 mol% GdY_2O_3. (a) HAADF image showing a nano pore at the grain boundary in 1 mol% GdY_2O_3. Areas of interest are highlighted with different colours. The EDS spectra are extracted at the nano pore (b), a clean grain boundary (c) and the adjacent gains (d, e). 77
4.26 Literature overview of the grain growth factor K displayed in an Arrhenius plot. Related values of K derived from this work are marked with stars. 80

5.1 Schematic graph of different processing induced surface defects. (1) fine ground surface finish (2) coarse ground surface finish (3) insufficient densification with a low relative density around 90.0 % (4) sufficient densification with a high relative density over 99.0 % (5) Surface crack induced during machining or mishandling of the component (in this work a hardness indenter is used to induce cracks). 83
5.2 SEM overview and detail images before and after exposure to a fluorine based etching plasma at a bias voltage of 150 V for 2h. All samples were sintered at 1500 °C, 50 MPa for 10 min and mirror polished (a), fine ground (d) and coarse ground (g). (b,e,h) shows the samples with different surface morphologies after plasma exposure. (c, f, i) shows related microstructure details in higher magnification. 84
5.3 SEM images of a dense sample (1500 °C, 50 MPa, 10 min) before (a) and after plasma exposure (b), as well as an insufficiently densified samples (1150 °C, 50 MPa, 10min) before (c) and after (d) plasma exposure. 85
5.4 (a) AFM topography scan of the surface of a dense sample after plasma exposure. Graphical detail highlights the position of line profiles in a spherical pore. (b) AFM line profiles through a spherical pore highlighting the main material removal process at sharp edges during the plasma exposure. 86
5.5 SEM overview and detail images of a indentation induced cracks before (a, b) and after (c, d) plasma exposure under 150 V bias for 2 h. . . 87
5.6 SEM images of the surface morphology after a plasma exposure for 2 h under a bias voltage of (a) 50 V (b) 150 V (c) 300V. 89
5.7 AFM scans of the surface morphology in topographic and amplitude mode after a plasma exposure for 2 h under a bias voltage of (a, b) 50 V. (c, d) 150 V. (e, f) 300V. 90
5.8 Detailed AFM analysis of the surface morphology after a plasma exposure for 2 h under a bias voltage of 300V in topographic (a) and amplitude mode (b). Colored lines in (a) mark the position of the AFM line profiles. Arrows in (b) highlight the position of microstructure independent sputtering craters. (c) AFM line profiles extracted from topography scan. 90
5.9 HRTEM images of Y_2O_3 after plasma exposure for 2 h under varied bias voltages of 50 V (a), 150 V (b) and 300 V (c). Included markers illustrate the increasing physical interaction depth from the surface. 91
5.10 (left) STEM-EDS images of Y_2O_3 after plasma exposure for 2 h under varying bias voltages (as indicated). (right) EDS spectra at different positions from the surface to the bulk (as indicated). 92

5.11 TOF-SIMS depth profiles showing the intensities of Y-, O- and F- for Y_2O_3 exposed to bias voltages of 50 (a), 150 (b) and 300 V (c). The background colour highlights the different characteristics of fluorine intensity depending on the applied voltage (I) high fluorine surface peak. (II) high fluorine intensity layer up to a depth of 40 nm at low bias voltages. (III) significantly decreased fluorine intensity in the bulk at high bias voltages. 94
5.12 SEM images of the surface morphology after a plasma exposure under 150 V for 2 h having a CF_4 volume percentage of (a) 5 % (b) 10% (c) 40% (d) 80 %. 95
5.13 Etching rate of Y_2O_3 and SiO_2 dependent on the plasma gas composition. The etch rate was determined on an etch step induced through masking parts of the exposed area. All samples were treated with a bias voltage of 150 V and the exposure duration was 2 h. The etch depth was determined using a confocal laser microscope for SiO_2 and an AFM for Y_2O_3. 96
5.14 TOF-SIMS depth profiles of all samples tested with different plasma gas compositions. Intensities of relevant elements are visualized in separated graphs showing (a) 18 O^- (b) Y^- (c) F^- and (d) C^- 97
5.15 Schematic plasma processing map displaying the active erosion mechanisms (P-physical, M-mixed, C-chemical erosion) under varying plasma parameters. 98
5.16 SEM overview and detail images of the surface before (a, c) and after (b, d) plasma exposure. 100
5.17 (a) SEM image of the surface topography after plasma exposure (b) AFM topography scan of the highlighted area in (a) showing the microstructure dependent topography (c) AFM amplitude scan showing different morphologies for certain grains in the microstructure. 100
5.18 (a) AFM topography scan of the microstructure dependent surface morphology (b) AFM amplitude scan (c) AFM line profiles extracted from the topography showing distinct height levels induced by plasma etching. 101
5.19 (a, c) EBSD orientation mapping before the plasma exposure (arrows indicate grains with comparable and different orientations) (c, d) Relocalized AFM topography scans at the same position after exposure showing an orientation dependent surface structure. 102
5.20 Correlation of the AFM height difference to the Euler angles ϕ (a) and φ_2 as well as ϕ (b). φ_2 as and ϕ were derived from EBSD measurements before the plasma exposure. 103
5.21 Median values of the AFM height difference dependent on the Euler angle ϕ. Representations of the crystal structure of Y_2O_3 at different rotation angles from $\phi = 0°$ to $\phi = 45°$ 104

5.22 Microstructure of Y_2O_3/YOF (80/20 w%) composites before plasma exposure. (a) SEM image of the surface. (b) EBSD mapping of the cubic YOF phase in the Z-direction (c) EBSD mapping of the cubic Y_2O_3 phase in the Z-direction. The corresponding IPF colour key is included in the image. 105
5.23 Correlation of phase composition with surface morphology after plasma exposure. (a) EBSD phase mapping before the plasma exposure (red - Y_2O_3; yellow - YOF). (b) AFM topography scan of the surface after exposure. (c) AFM amplitude scan of the surface after exposure. . . . 106
5.24 AFM investigation of the surface morphology. (a) Overview AFM topography scan (b, c) Lines scans marked in (a). (d, e) AFM topography details of a resistant Y_2O_3 grain and a YOF grain with lower etch resistance. 107
5.25 Correlation of relative topographic AFM height after plasma exposure to the crystalline orientation represented through the Euler angle ϕ for Y_2O_3 (blue) and YOF (green). 108
5.26 SEM-EDS investigation of the chemical composition at the surface of Y_2O_3/YOF composites. (a) SE-SEM image showing the surface after plasma exposure. White arrows highlight Y_2O_3 grains having a smooth morphology and a low etching resistance. Green arrows mark selected YOF grains. (b) EDS Mapping showing displaying the intensity of Y. (c) EDS Mapping showing the intensity of O (d) EDS Mapping showing the intensity of F 109
5.27 Correlation between crystalline orientation and surface fluorination of Y_2O_3 after plasma exposure. (a) EBSD orientation mapping of Y_2O_3 grains in the Z-direction. (b) Corresponding SEM-EDS elemental mapping of F at the same position. (c) Orientation density function displayed in a spherical projection. Orientations of Y_2O_3 grains which exhibit a low surface fluorination after plasma exposure are displayed revealing a strong dependency of the surface reaction from the orientation. 110
5.28 Correlation between crystalline orientation, surface fluorination and morphology of Y_2O_3 after plasma exposure. (a) SE-SEM image of the surface after plasma exposure. Detail (c) highlights a grain with low plasma resistance and smooth morphology (Type II). Detail (d) highlights a grain with high plasma resistance and a nano-porous morphology (Type I). (b) Part of the spherical projection displayed in Fig. 5.27 showing the orientation of grains with a low amount of surface fluorination (black dots) and the orientation of a grain with high surface fluorination (red star). Red and green circles mark the orientations of the grains shown in (a). (c, d) AFM topography details. 111

5.29 Crystallographic structure at the surface and orientation dependent surface fluorination. (a) Crystallographic structure along the (001) plane of Y_2O_3. (b) Crystallographic structure along the (111) plane of Y_2O_3. (c) Schematic representation of the proposed orientation dependent surface fluorination mechanism. The fluorocarbon film formation is controlled by the adsorption properties of the surface (I) leading to a different chemical degradation and differing etch resistance (II). 112

6.1 Correlation between the densification and grain growth kinetics during FAST/SPS sintering of pure and La^{3+} and Gd^{3+} doped Y_2O_3. The corresponding high resolution HAADF images and EDS mappings show a segregation of La atoms to the interface due to its ionic size mismatch with the host lattice. Both solute drag and Zener pinning of a dopant induced interfacial nano-porosity led to a stepwise reduction of the grain boundary mobility in doped yttria. 114

6.2 Plasma processing map displaying the dominating erosion mechanisms for Y_2O_3 under varied plasma parameters (P-physical, M-mixed, C-chemical erosion). Additional SEM images of Y_2O_3 samples exposed to different plasma etching parameters are displayed to highlight the strong influence of the active mechanism onto the erosion behaviour as well as the formed morphology (Parameters as indicated). 115

List of Tables

2.1 Parameters influencing the sintering process and the microstructure evolution. Adapted from [37]. 9
2.2 Mechanisms of densification during hot pressing and corresponding exponents for the hot pressing model by Coble which is derived from creep equations. Adapted from [36] 13
2.3 Overview on the FAST/SPS sintering parameters applied in various studies with pure Y_2O_3 powders. 27

3.1 Overview of the starting powders used in this work. 35
3.2 Overview on the processing parameters used in the milling study . . . 36
3.3 FAST/SPS parameters of commercial Y_2O_3 powders. 37
3.4 Overview on the sintering parameters applied during the investigation of densification and grain growth of rare earth doped Y_2O_3. 40
3.5 Ceramographic preparation procedure for Y_2O_3 ceramics. 41
3.6 Plasma etching parameters applied in this study to investigate the fundamental behaviour (S), the influence of bias voltage (B) and the influence of plasma gas composition (C.) 42
3.7 Overview about all investigated plasma etched samples including the applied sintering procedure, plasma etching parameters and applied characterization techniques. (r) in brackets indicates that the relocalization technique was applied to enable a correlation between sample microstructure before and after exposure. 43

4.1 Particle size and the specific surface area of the starting powders measured by laser granulometry and BET. 52
4.2 Chemical impurities of the commercial powders investigated by inductively coupled plasma mass spectroscopy (ICP - MS). All values are displayed in mg/kg and the mean value (MV) and standard deviation (SD) are calculated from three separated measurements. 52
4.3 Chemical impurities of milled PJ2 powders investigated by ICP-MS. A low energy milling process (roll bench milling (RB)) was included for comparison. All values are displayed in mg/kg and the mean value (MV) and standard deviation (SD) are calculated from three separated measurements. 57

Bibliography

[1] Moore, Gordon: Cramming more components onto integrated circuits. In: *Electronics* 38 (1965), Nr. 8

[2] Rastogi, Vinayak ; Ventzek, Peter L. ; Ranjan, Alok: Plasma etch challenges for next-generation semiconductor manufacturing. 2017. – Report

[3] Donnelly, Vincent M. ; Kornblit, Avinoam: Plasma etching: Yesterday, today, and tomorrow. In: *Journal of Vacuum Science & Technology A* 31 (2013), Nr. 5, S. 050825. – ISSN 0734–2101

[4] IEEE: International Roadmap for Devices and Systems 2020. 2020. – Report

[5] S., L.: The economist explains: The end of Moore's law. In: *The Economist* (2015)

[6] Nojiri, Kazuo: *Dry etching technology for semiconductors.* Springer, 2015. – ISBN 3319102958

[7] Leech, Patrick W.: Reactive ion etching of quartz and silica-based glasses in CF_4/CHF_3 plasmas. In: *Vacuum* 55 (1999), Nr. 3, S. 191–196. – ISSN 0042–207X

[8] Miwa, Kazuhiro ; Takada, Noriharu ; Sasaki, Koichi: Fluorination mechanisms of Al_2O_3 and Y_2O_3 surfaces irradiated by high-density CF_4-O_2 and SF_6-O_2 plasmas. In: *Journal of Vacuum Science & Technology A: Vacuum, Surfaces, and Films* 27 (2009), Nr. 4, S. 831–835. – ISSN 0734–2101 1520–8559

[9] Kim, Dae-Min ; Oh, Yoon-Suk ; Kim, Seongwon ; Kim, Hyung-Tae ; Lim, Dae-Soon ; Lee, Sung-Min: The erosion behaviors of Y_2O_3 and YF_3 coatings under fluorocarbon plasma. In: *Thin Solid Films* 519 (2011), Nr. 20, S. 6698–6702. – ISSN 0040–6090

[10] Kim, Young-Chan ; Kim, Chang-Il: Etching mechanism of Y_2O_3 thin films in high density Cl_2-Ar plasma. In: *Journal of Vacuum Science & Technology A: Vacuum, Surfaces, and Films* 19 (2001), Nr. 5, S. 2676–2679. – ISSN 0734–2101 1520–8559

[11] Kim, Dae-Min ; Lee, Sang-Ho ; Alexander, William B. ; Kim, Kyeong-Beom ; Oh, Yoon-Suk ; Lee, Sung-Min: X-Ray Photoelectron Spectroscopy Study on the Interaction of Yttrium-Aluminum Oxide with Fluorine-Based Plasma. In: *Journal of the American Ceramic Society* 94 (2011), Nr. 10, S. 3455–3459. – ISSN 00027820

[12] Kim, Dae-Min ; Jang, Mi-Ran ; Oh, Yoon-Suk ; Kim, Seongwon ; Lee, Sung-Min ; Lee, Sang-Ho: Relative sputtering rates of oxides and fluorides of aluminum and yttrium. In: *Surface and Coatings Technology* 309 (2017), S. 694–697. – ISSN 0257–8972

[13] Tsunoura, Toru ; Yoshida, Katsumi ; Yano, Toyohiko ; Kishi, Yukio: Fabrication, characterization, and fluorine-plasma exposure behavior of dense yttrium oxyfluoride ceramics. In: *Japanese Journal of Applied Physics* 56 (2017), Nr. 6S2, S. 06HC02. – ISSN 0021–4922 1347–4065

[14] MA, Tianyu ; LIST, Tyler ; DONNELLY, Vincent M.: Y_2O_3 wall interactions in Cl_2 etching and NF_3 cleaning plasmas. In: *Journal of Vacuum Science & Technology A: Vacuum, Surfaces, and Films* 35 (2017), Nr. 3, S. 031303. – ISSN 0734–2101

[15] MIYASHITA, Kenji ; TSUNOURA, Toru ; YOSHIDA, Katsumi ; YANO, Toyohiko ; KISHI, Yukio: Fluorine and oxygen plasma exposure behavior of yttrium oxyfluoride ceramics. In: *Japanese Journal of Applied Physics* 58 (2019), may, Nr. SE, S. SEEC01

[16] LEE, Seungjun ; LEE, Jaehoo ; KIM, Woongsik ; HWANG, Nong-Moon: Plasma Etching Behavior of YOF Coating Deposited by Suspension Plasma Spraying in Inductively Coupled CHF_3/Ar Plasma. In: *Coatings* 10 (2020), Nr. 11

[17] ASHIZAWA, Hiroaki ; YOSHIDA, Katsumi: Effect of the microstructures of yttria ceramics on their plasma corrosion behavior. In: *Ceramics International* (2019). – ISSN 0272–8842

[18] GUILLON, Olivier ; GONZALEZ-JULIAN, Jesus ; DARGATZ, Benjamin ; KESSEL, Tobias ; SCHIERNING, Gabi ; RÄTHEL, Jan ; HERRMANN, Mathias: Field-assisted sintering technology/spark plasma sintering: mechanisms, materials, and technology developments. In: *Advanced Engineering Materials* 16 (2014), Nr. 7, S. 830–849. – ISSN 1527–2648

[19] CHAIM, Rachman ; SHLAYER, Amit ; ESTOURNES, Claude: Densification of nanocrystalline Y_2O_3 ceramic powder by spark plasma sintering. In: *Journal of the European Ceramic Society* 29 (2009), Nr. 1, S. 91–98

[20] YOSHIDA, Hidehiro ; MORITA, Koji ; KIM, Byung-Nam ; HIRAGA, Keijiro ; KODO, Masayasu ; SOGA, Kohei ; YAMAMOTO, Takahisa: Densification of Nanocrystalline Yttria by Low Temperature Spark Plasma Sintering. In: *Journal of the American Ceramic Society* 91 (2008), Nr. 5, S. 1707–1710. – ISSN 0002–7820 1551–2916

[21] AN, Liqiong ; ITO, Akihiko ; GOTO, Takashi: Transparent yttria produced by spark plasma sintering at moderate temperature and pressure profiles. In: *Journal of the European Ceramic Society* 32 (2012), Nr. 5, S. 1035–1040. – ISSN 09552219

[22] GABORIAUD, RJ ; PAUMIER, F ; LACROIX, Bertrand: Disorder–order phase transformation in a fluorite-related oxide thin film: In-situ X-ray diffraction and modelling of the residual stress effects. In: *Thin Solid Films* 601 (2016), S. 84–88

[23] CHEN, Pei L. ; CHEN, I W.: Sintering of fine oxide powders: I, microstructural evolution. In: *Journal of the American Ceramic Society* 79 (1996), Nr. 12, S. 3129–3141. – ISSN 1551–2916

[24] FORNASIERO, L ; MIX, E ; PETERS, V ; PETERMANN, K ; HUBER, G: Czochralski growth and laser parameters of RE^{3+}-doped Y_2O_3 and Sc_2O_3. In: *Ceramics international* 26 (2000), Nr. 6, S. 589–592. – ISSN 0272–8842

[25] KLEIN, Philipp H. ; CROFT, William J.: Thermal Conductivity, Diffusivity, and Expansion of Y_2O_3, $Y_3Al_5O_{12}$, and LaF_3 in the Range 77–300 K. In: *Journal of Applied Physics* 38 (1967), Nr. 4, S. 1603–1607. – ISSN 0021–8979

[26] Wilfong, Roy L.: *Thermal Expansion of the Oxides of Yttrium, Cerium, Samarium, Europium, and Dysprosium.* Bd. 6180. US Department of the Interior, Bureau of Mines, 1963

[27] Wei, George C.: Extrinsic OH^- Absorption in Transparent Polycrystalline Lanthana Doped Yttria. In: *Journal of the American Ceramic Society* 71 (1988), Nr. 1, S. C20 – C23. – ISSN 0002–7820

[28] Wei, GC: Transparent ceramic lamp envelope materials. In: *Journal of Physics D: Applied Physics* 38 (2005), Nr. 17, S. 3057. – ISSN 0022–3727

[29] Kuang, JP ; Harding, RA ; Campbell, J: A study of refractories as crucible and mould materials for melting and casting γ-TiAl alloys. In: *International journal of cast metals research* 13 (2001), Nr. 5, S. 277–292. – ISSN 1364–0461

[30] Micheli, Adolph L. ; Dungan, Dennis F. ; Mantese, Joseph V.: High density yttria for practical ceramic applications. In: *Journal of the American Ceramic Society* 75 (1992), Nr. 3, S. 709–711. – ISSN 0002–7820

[31] Suzuki, Ken-ichiro ; Nishikawa, Koji ; Watakabe, Siro: Stability of yttria for titanium alloy precision casting mold. In: *Materials transactions, JIM* 38 (1997), Nr. 1, S. 54–62. – ISSN 0916–1821

[32] Majima, Kazuhiko ; Niimi, Norikazu ; Watanabe, Masanobu ; Katsuyama, Shigeru ; Nagai, Hiroshi: Effect of LiF addition on the preparation and transparency of vacuum hot pressed Y_2O_3. In: *Materials Transactions, JIM* 35 (1994), Nr. 9, S. 645–650. – ISSN 0916–1821

[33] Kochawattana, Sujarinee ; Stevenson, Adam ; Lee, Sang-Ho ; Ramirez, Mariola ; Gopalan, Venkatraman ; Dumm, John ; Castillo, Vida K. ; Quarles, Gregory J. ; Messing, Gary L.: Sintering and grain growth in SiO doped Nd:YAG. In: *Journal of the European Ceramic Society* 28 (2008), Nr. 7, S. 1527–1534. – ISSN 0955–2219

[34] Tsukuda, Y: Application of yttria as a refractory material. In: *Journal of the Canadian Ceramic Society* 52 (1983), S. 14–17. – ISSN 0068–8444

[35] Iwasawa, Junichi ; Nishimizu, Ryoichi ; Tokita, Masahiro ; Kiyohara, Masakatsu ; Uematsu, Keizo: Plasma-Resistant Dense Yttrium Oxide Film Prepared by Aerosol Deposition Process. In: *Journal of the American Ceramic Society* 90 (2007), Nr. 8, S. 2327–2332. – ISSN 0002–7820 1551–2916

[36] Rahaman, Mohamed N.: *Ceramic processing and sintering.* CRC press, 2003. – ISBN 0824709888

[37] Kang, Suk-Joong L.: *Sintering: densification, grain growth and microstructure.* Butterworth-Heinemann, 2004. – ISBN 0080493076

[38] Van Nguyen, Chung ; Sistla, Sree K. ; Van Kempen, Stanley ; Giang, Ngoc A. ; Bezold, Alexander ; Broeckmann, Christoph ; Lange, Friederike: A comparative study of different sintering models for Al_2O_3. In: *Journal of the Ceramic Society of Japan* 124 (2016), Nr. 4, S. 301–312. – ISSN 1882–0743

[39] Coble, R. L.: A Model for Boundary Diffusion Controlled Creep in Polycrystalline Materials. In: *Journal of Applied Physics* 34 (1963), Nr. 6, S. 1679–1682

[40] Coble, Robert L.: Diffusion Models for Hot Pressing with Surface Energy and Pressure Effects as Driving Forces. In: *Journal of Applied Physics* 41 (1970), Nr. 12, S. 4798–4807

[41] Herring, Conyers: Diffusional viscosity of a polycrystalline solid. In: *Journal of applied physics* 21 (1950), Nr. 5, S. 437–445

[42] Langer, Jochen ; Hoffmann, Michael J. ; Guillon, Olivier: Direct comparison between hot pressing and electric field-assisted sintering of submicron alumina. In: *Acta Materialia* 57 (2009), Nr. 18, S. 5454–5465. – ISSN 13596454

[43] Langer, Jochen ; Hoffmann, Michael J. ; Guillon, Olivier: Electric Field-Assisted Sintering in Comparison with the Hot Pressing of Yttria-Stabilized Zirconia. In: *Journal of the American Ceramic Society* 94 (2011), Nr. 1, S. 24–31. – ISSN 00027820

[44] Seidel, Jürgen ; Claussen, Nils ; Rödel, Jürgen: Reliability of alumina ceramics: effect of grain size. In: *Journal of the European Ceramic Society* 15 (1995), Nr. 5, S. 395–404

[45] Rice, Roy W. ; Freiman, Stephen W. ; Becher, Paul F.: Grain-size dependence of fracture energy in ceramics: I, experiment. In: *Journal of the American ceramic society* 64 (1981), Nr. 6, S. 345–350

[46] Naqash, Sahir ; Sebold, Doris ; Tietz, Frank ; Guillon, Olivier: Microstructure–conductivity relationship of $Na_3Zr_2(SiO_4)_2(PO_4)$ ceramics. In: *Journal of the American Ceramic Society* 102 (2019), Nr. 3, S. 1057–1070

[47] Sutorik, Anthony C. ; Green, Matthew D. ; Cooper, Christopher ; Wolfenstine, Jeffrey ; Gilde, Gary: The comparative influences of structural ordering, grain size, Li-content, and bulk density on the Li^+-conductivity of $Li_0 \cdot {}_{29}La_0 \cdot {}_{57}TiO_3$. In: *Journal of Materials Science* 47 (2012), Nr. 19, S. 6992–7002

[48] Kinoshita, Kyoichi ; Yamaji, Akihiko: Grain-size effects on dielectric properties in barium titanate ceramics. In: *Journal of applied physics* 47 (1976), Nr. 1, S. 371–373

[49] Burke, JE ; Turnbull, D: Recrystallization and grain growth. In: *Progress in metal physics* 3 (1952), S. 220–292

[50] Cahn, John W.: The impurity-drag effect in grain boundary motion. In: *Acta metallurgica* 10 (1962), Nr. 9, S. 789–798. – ISSN 0001–6160

[51] Jorgensen, PJ ; Anderson, RC: Grain boundary segregation and final stage sintering of Y_2O_3. In: *Journal of the American Ceramic Society* 50 (1967), Nr. 11, S. 553–558. – ISSN 1551–2916

[52] Rhodes, W. H.: Controlled Transient Solid Second-Phase Sintering of Yttria. In: *Journal of the American Ceramic Society* 64 (1981), Nr. 1, S. 13–19. – ISSN 0002–7820

[53] Katayama, K. ; Õsawa, H. ; Akiba, T. ; Urabe, K. ; Yanagida, H.: Sintering of yttrias with addition of divalent metal oxide and water vapour pressure dependence of their electrical conductivity. In: *Journal of Materials Science* 25 (1990), Nr. 2, S. 1503–1508. – ISSN 1573–4803

[54] Katayama, K. ; Osawa, H. ; Akiba, T. ; Yanagida, H.: Sintering and electrical properties of CaO-doped Y2O3. In: *Journal of the European Ceramic Society* 6 (1990), Nr. 1, S. 39–45. – ISSN 0955–2219

[55] Baumard, J. F. ; Vesteghem, Hervé ; Gasgnier, G. ; Boncoeur, M. ; Bougoin, M.: Densification of Yttria Ceramics. In: *Advanced Materials Research* 1-2 (1994), S. 47–54. – ISSN 1662–8985

[56] Gasgnier, G. ; Baumard, J. F. ; Boncoeur, M. ; Bougoin, M.: Enhanced densification of yttria by addition of titanium oxide. In: *Journal of the European Ceramic Society* 13 (1994), Nr. 1, S. 67–72. – ISSN 0955–2219

[57] Chen, Pei L. ; Chen, I W.: Grain boundary mobility in Y_2O_3: defect mechanism and dopant effects. In: *Journal of the American Ceramic Society* 79 (1996), Nr. 7, S. 1801–1809. – ISSN 1551–2916

[58] Chen, Pei-Lin ; Chen, I-Wei: Role of Defect Interaction in Boundary Mobility and Cation Diffusivity of CeO_2. In: *Journal of the American Ceramic Society* 77 (1994), Nr. 9, S. 2289–2297. – ISSN 0002–7820

[59] Chen, Pei L. ; Chen, I W.: Grain Growth in CeO_2: Dopant Effects, Defect Mechanism, and Solute Drag. In: *Journal of the American Ceramic Society* 79 (1996), Nr. 7, S. 1793–1800. – ISSN 0002–7820

[60] Busker, Gerdjan ; Chroneos, Alex ; Grimes, Robin W. ; Chen, I W.: Solution mechanisms for dopant oxides in yttria. In: *Journal of the American Ceramic Society* 82 (1999), Nr. 6, S. 1553–1559. – ISSN 1551–2916

[61] Chen, I-Wei: Grain Boundary Kinetics in Oxide Ceramics with the Cubic Fluorite Crystal Structure and its Derivatives. In: *Interface Science* 8 (2000), Nr. 2, S. 147–156. – ISSN 1573–2746

[62] Chen, I-Wei ; Wang, X-H: Sintering dense nanocrystalline ceramics without final-stage grain growth. In: *Nature* 404 (2000), Nr. 6774, S. 168–171. – ISSN 0028–0836

[63] Wang, Xiao H. ; Chen, Pei L. ; Chen, I W.: Two Step Sintering of Ceramics with Constant Grain Size I - Y_2O_3. In: *Journal of the American Ceramic society* 89 (2006), Nr. 2, S. 431–437. – ISSN 1551–2916

[64] Kodo, Masayasu ; Soga, Kohei ; Yoshida, Hidehiro ; Yamamoto, Takahisa: Low temperature sintering of polycrystalline yttria by transition metal ion doping. In: *Journal of the Ceramic Society of Japan* 117 (2009), Nr. 1366, S. 765–768. – ISSN 1882–0743

[65] Kodo, Masayasu ; Soga, Kohei ; Yoshida, Hidehiro ; Yamamoto, Takahisa: Doping effect of divalent cations on sintering of polycrystalline yttria. In: *Journal of the European Ceramic Society* 30 (2010), Nr. 13, S. 2741–2747. – ISSN 09552219

[66] Yoshida, Hidehiro ; Kodo, Masayasu ; Soga, Kohei ; Yamamoto, Takahisa: Doping effect on sinterability of polycrystalline yttria: From the viewpoint of cation diffusivity. In: *Journal of the European Ceramic Society* 32 (2012), Nr. 12, S. 3103–3114. – ISSN 09552219

[67] Huang, Yihua ; Jiang, Dongliang ; Zhang, Jingxian ; Lin, Qingling: Precipitation synthesis and sintering of lanthanum doped yttria transparent ceramics. In: *Optical Materials* 31 (2009), Nr. 10, S. 1448–1453. – ISSN 0925–3467

[68] Zhang, Jian ; An, Liqiong ; Liu, Min ; Shimai, Shunzo ; Wang, Shiwei: Sintering of Yb^{3+}:Y_2O_3 transparent ceramics in hydrogen atmosphere. In: *Journal of the European Ceramic Society* 29 (2009), Nr. 2, S. 305–309. – ISSN 0955–2219

[69] Podowitz, Stephen R. ; Gaumé, Romain ; Feigelson, Robert S.: Effect of Europium Concentration on Densification of Transparent Eu:Y_2O_3 Scintillator Ceramics Using Hot Pressing. In: *Journal of the American Ceramic Society* 93 (2010), Nr. 1, S. 82–88. – ISSN 0002–7820

[70] Zhang, Fei ; Vanmeensel, Kim ; Batuk, Maria ; Hadermann, Joke ; Inokoshi, Masanao ; Van Meerbeek, Bart ; Naert, Ignace ; Vleugels, Jef: Highly-translucent, strong and aging-resistant 3Y-TZP ceramics for dental restoration by grain boundary segregation. In: *Acta biomaterialia* 16 (2015), S. 215–222. – ISSN 1742–7061

[71] Hou, Xiaorui ; Zhou, Shengming ; Li, Wenjie ; Li, Yukun: Study on the effect and mechanism of zirconia on the sinterability of yttria transparent ceramic. In: *Journal of the European Ceramic Society* 30 (2010), Nr. 15, S. 3125–3129. – ISSN 0955–2219

[72] Jin, Lingling ; Zhou, Guohong ; Shimai, Shunzo ; Zhang, Jian ; Wang, Shiwei: ZrO_2-doped Y_2O_3 transparent ceramics via slip casting and vacuum sintering. In: *Journal of the European Ceramic Society* 30 (2010), Nr. 10, S. 2139–2143. – ISSN 0955–2219

[73] Ikesue, Akio ; Kamata, Kiichiro ; Yoshida, Kunio: Synthesis of Transparent Nd-doped HfO_2-Y_2O_3 Ceramics Using HIP. In: *Journal of the American Ceramic Society* 79 (1996), Nr. 2, S. 359–364. – ISSN 0002–7820

[74] Wang, Nengli ; Zhang, Xiyan ; Jiang, Haotian ; Dong, Tingting ; Yang, Di: Fabrication of $Er^{3+}/Yb^{3}+$ co-doped Y_2O_3 transparent ceramics by solid-state reaction method and its up-conversion luminescence. In: *Materials Chemistry and Physics* 135 (2012), Nr. 2, S. 709–713. – ISSN 0254–0584

[75] Yi, Qing ; Zhou, Shengming ; Teng, Hao ; Lin, Hui ; Hou, Xiaorui ; Jia, Tingting: Structural and optical properties of Tm:Y_2O_3 transparent ceramic with La_2O_3, ZrO_2 as composite sintering aid. In: *Journal of the European Ceramic Society* 32 (2012), Nr. 2, S. 381–388. – ISSN 0955–2219

[76] Ning, Kaijie ; Wang, Jun ; Luo, Dewei ; Zhang, Jian ; Dong, Zhi L. ; Kong, Ling B. ; Tang, Ding Y.: New double-sintering aid for fabrication of highly transparent ytterbium-doped yttria ceramics. In: *Journal of the European Ceramic Society* 36 (2016), Nr. 1, S. 253–256. – ISSN 0955–2219

[77] Kim, Changhun ; Lee, Doyun ; Lee, Jung-A. ; Lee, Joon-Hyung ; Heo, Young-Woo ; Kim, Jeong-Joo: Effect of ZnO and TiO_2 doping on the sintering behavior of Y_2O_3 ceramics. In: *Ceramics International* 45 (2019), Nr. 10, S. 13315–13318. – ISSN 0272–8842

[78] Yoshida, Hidehiro ; Morita, Koji ; Kim, Byung-Nam ; Soga, Kohei ; Yamamoto, Takahisa: Production of transparent yttrium oxide ceramics by the combination of low temperature spark plasma sintering and zinc cation-doping. In: *Journal of the European Ceramic Society* (2017). – ISSN 0955–2219

[79] Furuse, Hiroaki ; Nakasawa, Shunsuke ; Yoshida, Hidehiro ; Morita, Koji ; Suzuki, Tohru S. ; Kim, Byung-Nam ; Sakka, Yoshio ; Hiraga, Keijiro: Transparent ultrafine Yb^{3+}:Y_2O_3 laser ceramics fabricated by spark plasma sintering. In: *Journal of the American Ceramic Society* 101 (2018), Nr. 2, S. 694–702. – ISSN 0002–7820

[80] Munir, Z. A. ; Anselmi-Tamburini, U. ; Ohyanagi, M.: The effect of electric field and pressure on the synthesis and consolidation of materials: A review of the spark plasma sintering method. In: *Journal of Materials Science* 41 (2006), Nr. 3, S. 763–777. – ISSN 0022–2461 1573–4803

[81] Ihrig, Martin ; Finsterbusch, Martin ; Tsai, Chih-Long ; Laptev, Alexander M. ; Tu, Chia-hao ; Bram, Martin ; Sohn, Yoo J. ; Ye, Ruijie ; Sevinc, Serkan ; Lin, Shih-kang u. a.: Low temperature sintering of fully inorganic all-solid-state batteries–Impact of interfaces on full cell performance. In: *Journal of Power Sources* 482 (2021), S. 228905

[82] Zhang, Haibin ; Kim, Byung-Nam ; Morita, Koji ; Yoshida, Hidehiro ; Hiraga, Keijiro ; Sakka, Yoshio ; Ballato, J.: Fabrication of Transparent Yttria by High-Pressure Spark Plasma Sintering. In: *Journal of the American Ceramic Society* 94 (2011), Nr. 10, S. 3206–3210. – ISSN 00027820

[83] Dash, Apurv ; Kim, Byung-Nam ; Klimke, Jens ; Vleugels, Jef: Transparent tetragonal-cubic zirconia composite ceramics densified by spark plasma sintering and hot isostatic pressing. In: *Journal of the European Ceramic Society* 39 (2019), Nr. 4, S. 1428–1435

[84] Räthel, Jan ; Herrmann, Mathias ; Beckert, Wieland: Temperature distribution for electrically conductive and non-conductive materials during Field Assisted Sintering (FAST). In: *Journal of the European Ceramic Society* 29 (2009), Nr. 8, S. 1419–1425. `http://dx.doi.org/10.1016/j.jeurceramsoc.2008.09.015`. – DOI 10.1016/j.jeurceramsoc.2008.09.015. – ISSN 09552219

[85] Laptev, Alexander M. ; Bram, Martin ; Vanmeensel, Kim ; Gonzalez-Julian, Jesus ; Guillon, Olivier: Enhancing efficiency of field assisted sintering by advanced thermal insulation. In: *Journal of Materials Processing Technology* 262 (2018), S. 326–339. – ISSN 0924–0136

[86] Vanmeensel, K. ; Laptev, A. ; Hennicke, J. ; Vleugels, J. ; Vanderbiest, O.: Modelling of the temperature distribution during field assisted sintering. In: *Acta Materialia* 53 (2005), Nr. 16, S. 4379–4388. – ISSN 13596454

[87] Giuntini, Diletta ; Raethel, Jan ; Herrmann, Mathias ; Michaelis, Alexander ; Olevsky, Eugene A.: Advancement of tooling for spark plasma sintering. In: *Journal of the American Ceramic Society* 98 (2015), Nr. 11, S. 3529–3537

[88] Giuntini, Diletta ; Raethel, Jan ; Herrmann, Mathias ; Michaelis, Alexander ; Haines, Christopher D. ; Olevsky, Eugene A.: Spark plasma sintering novel tooling design: temperature uniformization during consolidation of silicon nitride powder. In: *Journal of the Ceramic Society of Japan* 124 (2016), Nr. 4, S. 403–414

[89] Chaim, Rachman: Densification mechanisms in spark plasma sintering of nanocrystalline ceramics. In: *Materials Science and Engineering: A* 443 (2007), Nr. 1-2, S. 25–32. – ISSN 09215093

[90] Rheinheimer, Wolfgang ; Fülling, Manuel ; Hoffmann, Michael J.: Grain growth in weak electric fields in strontium titanate: grain growth acceleration by defect redistribution. In: *Journal of the European Ceramic Society* 36 (2016), Nr. 11, S. 2773–2780

[91] Rheinheimer, Wolfgang ; Schoof, Ephraim ; Selzer, Michael ; Nestler, Britta ; Hoffmann, Michael J.: Non-Arrhenius grain growth in strontium titanate: Quantification of bimodal grain growth. In: *Acta Materialia* 174 (2019), S. 105–115. – ISSN 1359–6454

[92] Sistla, Sree K. ; Mishra, Tarini P. ; Deng, Yuanbin ; Kaletsch, Anke ; Bram, Martin ; Broeckmann, Christoph: Polarity-induced grain growth of gadolinium-doped ceria under field-assisted sintering technology/spark plasma sintering (FAST/SPS) conditions. In: *Journal of the American Ceramic Society* (2021)

[93] Yoshida, Hidehiro ; Morita, Koji ; Kim, Byung-Nam ; Hiraga, Keijiro ; Yamanaka, Kohei ; Soga, Kohei ; Yamamoto, Takahisa: Low-Temperature Spark Plasma Sintering of Yttria Ceramics with Ultrafine Grain Size. In: *Journal of the American Ceramic Society* 94 (2011), Nr. 10, S. 3301–3307. – ISSN 00027820

[94] Marder, Rachel ; Chaim, Rachman ; Estournès, Claude: Grain growth stagnation in fully dense nanocrystalline Y_2O_3 by spark plasma sintering. In: *Materials Science and Engineering: A* 527 (2010), Nr. 6, S. 1577–1585. – ISSN 09215093

[95] Ahmadi, Bahador ; Reza, Shoja R. ; Ahsanzadeh-Vadeqani, Mehdi ; Barekat, Masoud: Mechanical and optical properties of spark plasma sintered transparent Y_2O_3 ceramics. In: *Ceramics International* 42 (2016), Nr. 15, S. 17081–17088. – ISSN 02728842

[96] Shoja Razavi, Reza ; Ahsanzadeh-Vadeqani, Mehdi ; Barekat, Masoud ; Naderi, Mehdi ; Hashemi, Sayed H. ; Mishra, Ajay K.: Effect of sintering temperature on microstructural and optical properties of transparent yttria ceramics fabricated by spark plasma sintering. In: *Ceramics International* 42 (2016), Nr. 6, S. 7819–7823. – ISSN 02728842

[97] Cardinaud, Christophe: Fluorine-based plasmas: Main features and application in micro-and nanotechnology and in surface treatment. In: *Comptes Rendus Chimie* 21 (2018), Nr. 8, S. 723–739. – ISSN 1631–0748

[98] Oehrlein, GS ; Zhang, Y ; Vender, D ; Haverlag, M: Fluorocarbon high density plasmas: I. Fluorocarbon film deposition and etching using CF_4 and CHF_3. In: *Journal of Vacuum Science & Technology A: Vacuum, Surfaces, and Films* 12 (1994), Nr. 2, S. 323–332. – ISSN 0734–2101

[99] Oehrlein, GS ; Zhang, Y ; Vender, D ; Joubert, O: Fluorocarbon high density plasmas. II. Silicon dioxide and silicon etching using CF_4 and CHF_3. In: *Journal of Vacuum Science & Technology A* 12 (1994), Nr. 2, S. 333–344. – ISSN 0734–2101

[100] Inayoshi, Muneto ; Ito, Masafumi ; Hori, Masaru ; Goto, Toshio ; Hiramatsu, Mineo: Surface reaction of CF_2 radicals for fluorocarbon film formation in SiO_2/Si selective etching process. In: *Journal of Vacuum Science & Technology A* 16 (1998), Nr. 1, S. 233–238

[101] Zhang, Da ; Kushner, Mark J.: Mechanisms for CF_2 radical generation and loss on surfaces in fluorocarbon plasmas. In: *Journal of Vacuum Science & Technology A* 18 (2000), Nr. 6, S. 2661–2668. – ISSN 0734–2101

[102] Ling, Li ; Hua, X. ; Zheng, L. ; Oehrlein, G. S. ; Hudson, E. A. ; Jiang, P.: Studies of fluorocarbon film deposition and its correlation with etched trench sidewall angle by employing a gap structure using C_4F_8-Ar and CF_4-H_2 based capacitively coupled plasmas. In: *Journal of Vacuum Science & Technology B* 26 (2008), Nr. 1, S. 11–22

[103] Mogab, CJ ; Adams, AC ; Flamm, DL: Plasma etching of Si and SiO_2—the effect of oxygen additions to CF_4 plasmas. In: *Journal of applied physics* 49 (1978), Nr. 7, S. 3796–3803. – ISSN 0021–8979

[104] Oehrlein, Gottlieb S. ; Williams, Holly L.: Silicon etching mechanisms in a CF_4/H_2 glow discharge. In: *Journal of applied physics* 62 (1987), Nr. 2, S. 662–672

[105] Butterbaugh, JW ; Gray, DC ; Sawin, HH: Plasma surface interactions in fluorocarbon etching of silicon dioxide. In: *Journal of Vacuum Science & Technology B* 9 (1991), Nr. 3, S. 1461–1470. – ISSN 1071–1023

[106] Jung, Jae-Hyun ; Hahn, Byung-Dong ; Yoon, Woon-Ha ; Park, Dong-Soo ; Choi, Jong-Jin ; Ryu, Jungho ; Kim, Jong-Woo ; Ahn, Cheolwoo ; Song, Kie-Moon: Halogen plasma erosion resistance of rare earth oxide films deposited on plasma sprayed alumina coating by aerosol deposition. In: *Journal of the European Ceramic Society* 32 (2012), Nr. 10, S. 2451–2457. – ISSN 0955–2219

[107] Ashizawa, Hiroaki ; Kiyohara, Masakatsu: Plasma Exposure Behavior of Yttrium Oxide Film Formed by Aerosol Deposition Method. In: *IEEE Transactions on Semiconductor Manufacturing* 30 (2017), Nr. 4, S. 357–361. – ISSN 0894–6507

[108] Cao, Yu-Chao ; Zhao, Lei ; Luo, Jin ; Wang, Ke ; Zhang, Bo-Ping ; Yokota, Hiroki ; Ito, Yoshiyasu ; Li, Jing-Feng: Plasma etching behavior of Y_2O_3 ceramics: Comparative study with Al_2O_3. In: *Applied Surface Science* 366 (2016), S. 304–309. – ISSN 0169–4332

[109] Lin, Tzu-Ken ; Wang, Wei-Kai ; Huang, Shih-Yung ; Tasi, Chi-Tsung ; Wuu, Dong-Sing: Comparison of Erosion Behavior and Particle Contamination in Mass-Production CF_4/O_2 Plasma Chambers Using Y_2O_3 and YF_3 Protective Coatings. In: *Nanomaterials* 7 (2017), Nr. 7, S. 183

[110] Kitamura, Junya ; Tang, Zhaolin ; Mizuno, Hiroaki ; Sato, Kazuto ; Burgess, Alan: Structural, Mechanical and Erosion Properties of Yttrium Oxide Coatings by Axial Suspension Plasma Spraying for Electronics Applications. In: *Journal of Thermal Spray Technology* 20 (2011), Nr. 1, S. 170–185. – ISSN 1544–1016

[111] Zhao, Dong ; Wang, ChuanYang ; Chen, Yao ; Wang, YongGuang: Phase composition, structural, and plasma erosion properties of ceramic coating prepared by suspension plasma spraying. In: *International Journal of Applied Ceramic Technology* 15 (2018), Nr. 6, S. 1388–1396. – ISSN 1546–542X

[112] Kim, Chan S. ; Kim, Myong J. ; Cho, Hyun ; Park, Tae-Eon ; Yun, Young-Hoon: Fabrication and plasma resistance of Y_2O_3 ceramics. In: *Ceramics International* 41 (2015), Nr. 10, S. 12757–12762. – ISSN 0272–8842

[113] Kim, Dae-Min ; Kim, Kyeong-Beom ; Yoon, So-Young ; Oh, Yoon-Suk ; Kim, Hyung-Tae ; Lee, Sung-Min: Effects of artificial pores and purity on the erosion behaviors of polycrystalline Al_2O_3 ceramics under fluorine plasma. In: *Journal of the Ceramic Society of Japan* 117 (2009), Nr. 1368, S. 863–867. – ISSN 1882–0743

[114] Choi, Kwan-Young ; Oh, Yoon-Suk ; Kim, Seongwon ; Lee, Sung-Min: High erosion resistant Y_2O_3–carbon electroconductive composite under the fluorocarbon plasma. In: *Ceramics International* 39 (2013), Nr. 2, S. 1209–1214. – ISSN 02728842

[115] Shiba, Yoshinobu ; Teramoto, Akinobu ; Goto, Tetsuya ; Kishi, Yukio ; Shirai, Yasuyuki ; Sugawa, Shigetoshi: Stable yttrium oxyfluoride used in plasma process chamber. In: *Journal of Vacuum Science & Technology A* 35 (2017), Nr. 2, S. 021405. – ISSN 0734–2101

[116] Seeck, Oliver H. ; Murphy, Bridget: *X-ray Diffraction: Modern Experimental Techniques*. CRC Press, 2015

[117] Stamminger, Mark: *Fluorocarbon plasma erosion of silica glass doped with aluminum*, Ruhr-Universität Bochum, Universitätsbibliothek, doctoralthesis, 2020. `http://dx.doi.org/10.13154/294-6890`. – DOI 10.13154/294–6890

[118] Schwartz, Adam J. ; Kumar, Mukul ; Adams, Brent L. ; Field, David P.: *Electron backscatter diffraction in materials science*. Bd. 2. Springer, 2009

[119] Egerton, RF: *Physical Principles of Electron Microscopy: An Introduction to TEM, SEM, and AEM*. Springer, 2016

[120] Fultz, Brent ; Howe, James M.: *Transmission electron microscopy and diffractometry of materials*. Springer Science & Business Media, 2012

[121] Voigtländer, Bert: *Atomic Force Microscopy*. Springer, 2019

[122] Vickerman, John C. ; Briggs, David: *Tof-SIMS: materials analysis by mass spectrometry*. im publications, 2013

[123] König, Markus ; Höhn, Sören ; Hoffmann, Rudolf ; Suffner, Jens ; Lauterbach, Stefan ; Weiler, Ludwig ; Guillon, Olivier ; Rödel, Jürgen: Sintering of hierarchically structured ZnO. In: *Journal of Materials Research* 25 (2011), Nr. 11, S. 2125–2134. – ISSN 0884–2914 2044–5326

[124] Salmang, Hermann ; Scholze, Horst ; Telle, Rainer: *Keramik*. Springer, 2007. – ISBN 3540632735

[125] Tokita, Masao: The Potential of Spark Plasma Sintering (SPS) Method for the Fabrication on an Industrial Scale of Functionally Graded Materials. In: *12th INTERNATIONAL CERAMICS CONGRESS PART B* Bd. 63, Trans Tech Publications Ltd, 1 2011 (Advances in Science and Technology), S. 322–331

[126] Weston, N. S. ; Derguti, F. ; Tudball, A. ; Jackson, M.: Spark plasma sintering of commercial and development titanium alloy powders. In: *Journal of Materials Science* 50 (2015), Nr. 14, S. 4860–4878. – ISSN 1573–4803

[127] Boulnat, X. ; Fabregue, D. ; Perez, M. ; Urvoy, S. ; Hamon, D. ; Carlan, Y. de: Assessment of consolidation of oxide dispersion strengthened ferritic steels by spark plasma sintering: from laboratory scale to industrial products. In: *Powder Metallurgy* 57 (2014), Nr. 3, S. 204–211

[128] Achenani, Youssef ; Saâdaoui, Malika ; Cheddadi, Abdelkhalek ; Bonnefont, Guillaume ; Fantozzi, Gilbert: Finite element modeling of spark plasma sintering: Application to the reduction of temperature inhomogeneities, case of alumina. In: *Materials & Design* 116 (2017), S. 504–514. – ISSN 0264–1275

[129] Manière, Charles ; Durand, Lise ; Weibel, Alicia ; Chevallier, Geoffroy ; Estournès, Claude: A sacrificial material approach for spark plasma sintering of complex shapes. In: *Scripta Materialia* 124 (2016), S. 126–128. – ISSN 1359–6462

[130] Manière, Charles ; Nigito, Emmanuel ; Durand, Lise ; Weibel, Alicia ; Beynet, Yannick ; Estournes, Claude: Spark plasma sintering and complex shapes: The deformed interfaces approach. In: *Powder Technology* 320 (2017), S. 340–345. – ISSN 0032–5910

[131] Arnaud, Claire ; Manière, Charles ; Chevallier, Geoffroy ; Estournès, Claude ; Mainguy, Ronan ; Lecouturier, Florence ; Mesguich, David ; Weibel, Alicia ; Durand, Lise ; Laurent, Christophe: Dog-bone copper specimens prepared by one-step spark plasma sintering. In: *Journal of materials science* 50 (2015), Nr. 22, S. 7364–7373. – ISSN 0022–2461

[132] Wei, Xialu ; Izhvanov, Oleg ; Back, Christina ; Haines, Christopher ; Martin, Darold ; Vecchio, Kenneth ; Olevsky, Eugene: Spark plasma sintering of structure tailored ultrahigh temperature components - First step to complex net shaping. In: *Journal of the American Ceramic Society* 102 (2019), Nr. 2, S. 548–558. – ISSN 0002–7820

[133] HOCQUET, S. ; DUPONT, V. ; CAMBIER, F. ; LUDEWIG, F. ; VANDEWALLE, N.: Densification of complex shape ceramics parts by SPS. In: *Journal of the European Ceramic Society* 40 (2020), Nr. 7, S. 2586–2596. – ISSN 0955–2219

[134] SORDELET, Daniel J. ; AKINC, Mufit: Sintering of monosized, spherical yttria powders. In: *Journal of the American Ceramic Society* 71 (1988), Nr. 12, S. 1148–1153

[135] WYNBLATT, P. ; ROHRER, G. S. ; PAPILLON, F.: Grain boundary segregation in oxide ceramics. In: *Journal of the European Ceramic Society* 23 (2003), Nr. 15, S. 2841–2848. – ISSN 0955–2219

[136] YAN, M. F. ; CANNON, R. M. ; BOWEN, H. K.: Space-charge, Elastic Field, and Dipole Contributions To Equilibrium Solute Segregation At Interfaces. In: *Journal of Applied Physics* 54 (1983), Nr. 2, S. 764–778. `http://dx.doi.org/10.1063/1.332035`. – DOI 10.1063/1.332035

[137] KIM, Dongha ; BLIEM, Roland ; HESS, Franziska ; GALLET, Jean-Jacques ; YILDIZ, Bilge: Electrochemical Polarization Dependence of the Elastic and Electrostatic Driving Forces to Aliovalent Dopant Segregation on $LaMnO_3$. In: *J. Am. Chem. Soc.* 142 (2020), Nr. 7, S. 3548–3563

[138] GREGORI, G. ; MERKLE, R. ; MAIER, J.: Ion conduction and redistribution at grain boundaries in oxide systems. In: *Progress In Materials Science* 89 (2017), S. 252–305

[139] LEE, Wonyoung ; HAN, Jeong W. ; CHEN, Yan ; CAI, Zhuhua ; YILDIZ, Bilge: Cation Size Mismatch and Charge Interactions Drive Dopant Segregation at the Surfaces of Manganite Perovskites. In: *J. Am. Chem. Soc.* 135 (2013), Nr. 21, S. 7909–7925

[140] DESU, Seshu B. ; PAYNE, David A.: Interfacial Segregation in Perovskites: I, Theory. In: *Journal of the American Ceramic Society* 73 (1990), Nr. 11, S. 3391–3397

[141] RAABE, D. ; HERBIG, M. ; SANDLÖBES, S. ; LI, Y. ; TYTKO, D. ; KUZMINA, M. ; PONGE, D. ; CHOI, P. P.: Grain boundary segregation engineering in metallic alloys: A pathway to the design of interfaces. In: *Current Opinion in Solid State and Materials Science* 18 (2014), Nr. 4, S. 253–261

[142] TOMÁNEK, D. ; ALIGIA, A. A. ; BALSEIRO, C. A.: Calculation of elastic strain and electronic effects on surface segregation. In: *Phys. Rev. B* 32 (1985), Nr. 8, S. 5051–5056

[143] HWANG, Shyh-Lung ; CHEN, I. W.: Grain Size Control of Tetragonal Zirconia Polycrystals Using the Space Charge Concept. In: *Journal of the American Ceramic Society* 73 (1990), Nr. 11, S. 3269–3277. – ISSN 0002–7820

[144] BOULCH, F. ; DJURADO, E. ; DESSEMOND, L.: Dopant Segregation and Space Charge Effect in Nanostructured Tetragonal Zirconia. In: *Journal of The Electrochemical Society* 151 (2004), Nr. 8, S. A1210

[145] FABRICHNAYA, O ; WANG, Ch ; ZINKEVICH, M ; ALDINGER, F ; LEVI, CG: Phase equilibria and thermodynamic properties of the ZrO_2-$GdO_{1\cdot5}$-$YO_{1\cdot5}$ system. In: *Journal of phase equilibria and diffusion* 26 (2005), Nr. 6, S. 591–604. – ISSN 1547–7037

[146] Fabrichnaya, O. ; Zinkevich, M. ; Aldinger, F.: Thermodynamic modelling in the ZrO_2–La_2O_3–Y_2O_3–Al_2O_3 system. In: *International Journal of Materials Research* 98 (2007), Nr. 9, S. 838–846. – ISSN 1862–5282

[147] Vikrant, K. S. N. ; Rheinheimer, Wolfgang ; Garcia, R. E.: Electrochemical drag effect on grain boundary motion in ionic ceramics. In: *npj Computational Materials* 6 (2020), Nr. 1, S. 165–

[148] Boutz, M. M. R. ; Winnubst, A. J. A. ; Burggraaf, A. J.: Yttria-ceria stabilized tetragonal zirconia polycrystals: Sintering, grain growth and grain boundary segregation. In: *Journal of the European Ceramic Society* 13 (1994), Nr. 2, S. 89–102

[149] Vikrant, K. S. N. ; Rheinheimer, Wolfgang ; Sternlicht, Hadas ; Bäurer, Michael ; Garcia, R. E.: Electrochemically-driven abnormal grain growth in ionic ceramics. In: *Acta Materialia* 200 (2020), S. 727–734

[150] Rahaman, M. N. ; Manalert, R.: Grain boundary mobility of $BaTiO_3$ doped with aliovalent cations. In: *Journal of the European Ceramic Society* 18 (1998), Nr. 8, S. 1063–1071

[151] Koju, R. K. ; Mishin, Y.: Atomistic study of grain-boundary segregation and grain-boundary diffusion in Al-Mg alloys. In: *Acta Materialia* 201 (2020), S. 596–603

[152] Esin, Vladimir A. ; Souhar, Youssef: Solvent grain boundary diffusion in binary solid solutions: a new approach to evaluate solute grain boundary segregation. In: *Philosophical Magazine* 94 (2014), Nr. 35, S. 4066–4079

[153] Divinski, Sergiy V. ; Reglitz, Gerrit ; Wilde, Gerhard: Grain boundary self-diffusion in polycrystalline nickel of different purity levels. In: *Acta Materialia* 58 (2010), Nr. 2, S. 386–395

[154] Herzig, Christian ; Divinski, Sergiy V.: Grain Boundary Diffusion in Metals: Recent Developments. In: *Materials Transactions* 44 (2003), Nr. 1, S. 14–27

[155] Bernardini, J. ; Gas, P. ; Hondros, Ernest D. ; Seah, M. P. ; Nicholson, Robin B.: The role of solute segregation in grain boundary diffusion. In: *Proceedings of the Royal Society of London. A. Mathematical and Physical Sciences* 379 (1982), Nr. 1776, S. 159–178

[156] Cho, Junghyun ; Rickman, Jeffrey M. ; Chan, Helen M. ; Harmer, Martin P.: Modeling of Grain-Boundary Segregation Behavior in Aluminum Oxide. In: *Journal of the American Ceramic Society* 83 (2000), Nr. 2, S. 344–352

[157] Sakaguchi, Isao ; Srikanth, Varanasi ; Ikegami, Takayasu ; Haneda, Hajime: Grain Boundary Diffusion of Oxygen in Alumina Ceramics. In: *Journal of the American Ceramic Society* 78 (1995), Nr. 9, S. 2557–2559

[158] Morita, Koji ; Kim, Byung-Nam ; Yoshida, Hidehiro ; Hiraga, Keijiro ; Sakka, Yoshio: Distribution of carbon contamination in oxide ceramics occurring during spark-plasma-sintering (SPS) processing: II-Effect of SPS and loading temperatures. In: *Journal of the European Ceramic Society* 38 (2018), Nr. 6, S. 2596–2604

[159] Bennison, SJ ; Harmer, MP: Swelling of Hot-Pressed Al_2O_3. In: *Journal of the American Ceramic Society* 68 (1985), Nr. 11, S. 591–597

[160] Morita, Koji ; Kim, Byung-Nam ; Yoshida, Hidehiro ; Hiraga, Keijiro ; Sakka, Yoshio: Distribution of carbon contamination in MgAl2O4 spinel occurring during spark-plasma-sintering (SPS) processing: I–effect of heating rate and post-annealing. In: *Journal of the European Ceramic Society* 38 (2018), Nr. 6, S. 2588–2595

[161] Morita, K ; Kim, B-N ; Hiraga, K ; Yoshida, H: Fabrication of transparent $MgAl_2O_4$ spinel polycrystal by spark plasma sintering processing. In: *Scripta Materialia* 58 (2008), Nr. 12, S. 1114–1117

[162] Hötzer, J. ; Rehn, V. ; Rheinheimer, W. ; Hoffmann, M. J. ; Nestler, B.: Phase-field study of pore-grain boundary interaction. In: *Journal of the Ceramic Society of Japan* 124 (2016), Nr. 4, S. 329–339

[163] Rehn, Veronika ; Hötzer, Johannes ; Rheinheimer, Wolfgang ; Seiz, Marco ; Serr, Christopher ; Nestler, Britta: Phase-field study of grain growth in porous polycrystals. In: *Acta Materialia* 174 (2019), S. 439–449

[164] Ma, Shuailei ; Harmer, Martin P.: Near-Intrinsic Grain-Boundary Mobility in Dense Yttria. In: *Journal of the American Ceramic Society* 94 (2011), Nr. 3, S. 651–655. – ISSN 0002–7820

[165] Duran, P ; Tartaj, J ; Moure, C: Sintering behaviour of Y_2O_3 powders prepared by the polymer complex solution method. In: *Ceramics international* 28 (2002), Nr. 7, S. 791–803. – ISSN 0272–8842

[166] Bernard Granger, Guillaume ; Guizard, Christian ; San Miguel, Laurie: Sintering behavior and optical properties of yttria. In: *Journal of the American Ceramic Society* 90 (2007), Nr. 9, S. 2698–2702. – ISSN 0002–7820

[167] Kim, Moonkeun ; Efremov, Alexander ; Hong, MunPyo ; Min, Nam K. ; Park, Hyung-Ho ; Baek, Kyu-Ha ; Kwon, Kwang-Ho: Effect of Gas Mixing Ratio on Etch Behavior of Y_2O_3 Thin Films in Cl_2/Ar and BCl_3/Ar Inductively Coupled Plasmas. In: *Japanese Journal of Applied Physics* 49 (2010), Nr. 8S1, S. 08JB04. – ISSN 1347–4065

[168] Kwon, Kwangho ; Kim, Youngkeun ; Efremov, Alexander ; Kim, Kwangsoo: On the dry etch mechanisms of Y_2O_3, SiO_2, and Si_3N_4 in a Cl_2/BCl_3 inductively coupled plasma. In: *Journal of the Korean Physical Society* 58 (2011), Nr. 3, S. 467–471

[169] Balden, M. ; Bardamid, A. F. ; Belyaeva, A. I. ; Slatin, K. A. ; Davis, J. W. ; Haasz, A. A. ; Poon, M. ; Konovalov, V. G. ; Ryzhkov, I. V. ; Shapoval, A. N. ; Voitsenya, V. S.: Surface roughening and grain orientation dependence of the erosion of polycrystalline stainless steel by hydrogen irradiation. In: *Journal of Nuclear Materials* 329-333 (2004), S. 1515–1519. – ISSN 0022–3115

[170] Rasinski, M. ; Kreter, A. ; Torikai, Y. ; Linsmeier, Ch: The microstructure of tungsten exposed to D plasma with different impurities. In: *Nuclear Materials and Energy* 12 (2017), S. 302–306. – ISSN 2352–1791

[171] Voitsenya, V. S. ; Balden, M. ; Belyaeva, A. I. ; Alimov, V. ; Tyburska-Pueschel, B. ; Galuza, A. ; Kasilov, A. ; Kolenov, I. ; Konovalov, V. ; Skoryk, O. O. ; Solodovchenko, S. I.: Effect of sputtering on self-damaged recrystallized W mirror specimens. In: *Journal of Nuclear Materials* 434 (2013), Nr. 1, S. 375–381. – ISSN 0022–3115

[172] Voitsenya, VS ; Bardamid, AF ; Donné, AJH: Experimental simulation of the behaviour of diagnostic first mirrors fabricated of different metals for ITER conditions. In: *Open Physics Journal* 3 (2016), Nr. 1

[173] In: Roosendaal, Hans E.: *Sputtering yields of single crystalline targets*. Springer, 1981, S. 219–256

[174] Onderdelinden, D.: The Influence of Channeling On Cu Single Crystal Sputtering. In: *Applied Physics Letters* 8 (1966), Nr. 8, S. 189–190. – ISSN 0003–6951

[175] Yu, Lock S. ; Harper, James M. E. ; Cuomo, Jerome J. ; Smith, David A.: Control of thin film orientation by glancing angle ion bombardment during growth. In: *Journal of Vacuum Science & Technology A* 4 (1986), Nr. 3, S. 443–447

[176] Dong, L. ; Srolovitz, D. J.: Mechanism of texture development in ion-beam-assisted deposition. In: *Applied Physics Letters* 75 (1999), Nr. 4, S. 584–586

[177] Dong, Liang ; Zepeda-Ruiz, Luis A. ; Srolovitz, David J.: Sputtering and in-plane texture control during the deposition of MgO. In: *Journal of Applied Physics* 89 (2001), Nr. 7, S. 4105–4112. – ISSN 0021–8979

[178] Goto, Tetsuya ; Shiba, Yoshinobu ; Teramoto, Akinobu ; Kishi, Yukio ; Sugawa, Shigetoshi: Plasma resistance of sintered and ion-plated yttrium oxyfluorides with various Y, O, and F composition ratios for use in plasma process chamber. In: *Journal of Vacuum Science & Technology A* 38 (2020), Nr. 4, S. 043003

[179] Ma, Tianyu ; List, Tyler ; Donnelly, Vincent M.: Comparisons of NF_3 plasma-cleaned Y_2O_3, YOF, and YF_3 chamber coatings during silicon etching in Cl_2 plasmas. In: *Journal of Vacuum Science & Technology A* 36 (2018), Nr. 3, S. 031305. – ISSN 0734–2101

[180] Kaplan, Wayne D. ; Chatain, Dominique ; Wynblatt, Paul ; Carter, W. C.: A review of wetting versus adsorption, complexions, and related phenomena: the rosetta stone of wetting. In: *Journal of Materials Science* 48 (2013), Nr. 17, S. 5681–5717. – ISSN 1573–4803

[181] Tam, Jason ; Feng, Bin ; Ikuhara, Yuichi ; Ohta, Hiromichi ; Erb, Uwe: Crystallographic orientation–surface energy–wetting property relationships of rare earth oxides. In: *Journal of Materials Chemistry A* 6 (2018), Nr. 38, S. 18384–18388. – ISSN 2050–7488

[182] Wang, Siyan ; Wang, Jianqiu: Effect of grain orientation on the corrosion behavior of polycrystalline Alloy 690. In: *Corrosion Science* 85 (2014), S. 183–192. – ISSN 0010–938X

[183] Bland, Leslie G. ; Gusieva, K. ; Scully, J. R.: Effect of Crystallographic Orientation on the Corrosion of Magnesium: Comparison of Film Forming and Bare Crystal Facets using Electrochemical Impedance and Raman Spectroscopy. In: *Electrochimica Acta* 227 (2017), S. 136–151. – ISSN 0013–4686

[184] Dong, Shiqi ; Chen, Xin ; La Plante, Erika C. ; Gussev, Maxim ; Leonard, Keith ; Sant, Gaurav: Elucidating the grain-orientation dependent corrosion rates of austenitic stainless steels. In: *Materials & Design* 191 (2020), S. 108583. – ISSN 0264–1275

[185] Yang, Chengwu ; Yu, Xiaojuan ; Heissler, Stefan ; Weidler, Peter G. ; Nefedov, Alexei ; Wang, Yuemin ; Wöll, Christof ; Kropp, Thomas ; Paier, Joachim ; Sauer, Joachim: O_2 Activation on Ceria Catalysts—The Importance of Substrate Crystallographic Orientation. In: *Angewandte Chemie International Edition* 56 (2017), Nr. 51, S. 16399–16404. – ISSN 1433–7851

[186] Yang, Zongxian ; Woo, Tom K. ; Baudin, Micael ; Hermansson, Kersti: Atomic and electronic structure of unreduced and reduced CeO_2 surfaces: A first-principles study. In: *The Journal of Chemical Physics* 120 (2004), Nr. 16, S. 7741–7749

[187] Agraharam, Sairam ; Hess, Dennis W. ; Kohl, Paul A. ; Bidstrup Allen, Sue A.: Plasma chemistry in fluorocarbon film deposition from pentafluoroethane/argon mixtures. In: *Journal of Vacuum Science & Technology A* 17 (1999), Nr. 6, S. 3265–3271

[188] Takahashi, Kazuo ; Tachibana, Kunihide: Molecular composition of films and solid particles polymerized in fluorocarbon plasmas. In: *Journal of Applied Physics* 89 (2001), Nr. 2, S. 893–899

Band / Volume 539
Distribution of trace gases with adverse effects on fuel cells
D. Klemp, R. Wegener, R. Dubus, L. Karadurmus, N. Kille, Z. Tan (2021), 160 pp
ISBN: 978-3-95806-551-2

Band / Volume 540
Cyclotron Irradiation on Tungsten & Co-relation of Thermo-Mechanical Properties to Displacement and Transmutation Damage
R. Rayaprolu (2021), xiv, 211 pp
ISBN: 978-3-95806-552-9

Band / Volume 541
Smart Energy in Haushalten:
Technologien, Geschäftsmodelle, Akzeptanz und Wirtschaftlichkeit
H. Shamon, T. Rehm, B. Helgeson, F. Große-Kreul, M. Gleue, U. Paukstadt, G. Aniello, T. Schneiders, C. Frings, A. Reichmann, A. Löschel, T. Gollhardt, W. Kuckshinrichs, K. Gruber, P. Overath, C. Baedeker, F. Chasin, K. Witte, J. Becker
(2021), VI, 142 pp
ISBN: 978-3-95806-554-3

Band / Volume 542
Deployment Status of Fuel Cells in Road Transport: 2021 Update
R. C. Samsun, L. Antoni, M. Rex, D. Stolten (2021), 37 pp
ISBN: 978-3-95806-556-7

Band / Volume 543
Processing and creep resistance of short SiC fiber
containing Ti_3SiC_2 MAX phase composites
A. Dash (2021), vii, 125 pp
ISBN: 978-3-95806-558-1

Band / Volume 544
Synthese und Charakterisierung von Geopolymeren
für die Entsorgung der Spaltprodukte ^{137}Cs und ^{90}Sr
S. K. Weigelt (2021), VI, 186 pp
ISBN: 978-3-95806-559-8

Band / Volume 545
Potential depletion of ozone in the mid-latitude lowermost stratosphere in summer under geoengineering conditions
S. Robrecht (2021), 185 pp
ISBN: 978-3-95806-563-5

Band / Volume 546
Two-phase Flow in Porous Transport Layers of Polymer Electrolyte Membrane Electrolysers
D. Borah (2021), xi, 196 pp
ISBN: 978-3-95806-564-2

Band / Volume 547
Effects of root temperature on food quality of horticultural crops
F. He (2021), V, 143 pp
ISBN: 978-3-95806-565-9

Band / Volume 548
Verhalten und Kontrolle von Schlacken des bioliq®-Vergasers
K. Mielke (2021), 162, XXXV pp
ISBN: 978-3-95806-566-6

Band / Volume 549
Gravity waves resolved in Numerical Weather Prediction products
C. Strube (2021), iii, 139 pp
ISBN: 978-3-95806-567-3

Band / Volume 550
Experimental study of the chemical degradation of biogenic volatile organic compounds by atmospheric OH radicals
M. Rolletter (2021), XIII, 199 pp
ISBN: 978-3-95806-568-0

Band / Volume 551
Infiltrated Positive Electrodes for All-Solid-State Sodium Batteries
T. Lan (2021), vi, 104 pp
ISBN: 978-3-95806-576-5

Band / Volume 552
Trajectory Analysis on the Asian Tropopause Aerosol Layer (ATAL) based on Balloon Measurements at the Foothills of the Himalayas
S. Hanumanthu (2021), xiv, 147 pp
ISBN: 978-3-95806-578-9

Band / Volume 553
Field assisted sintering of yttria ceramics for plasma etching applications
M. Kindelmann (2021), VI, 122, XXX
ISBN: 978-3-95806-579-6

Weitere ***Schriften des Verlags im Forschungszentrum Jülich*** unter
http://wwwzb1.fz-juelich.de/verlagextern1/index.asp

Energie & Umwelt / Energy & Environment
Band / Volume 553
ISBN 978-3-95806-579-6

Mitglied der Helmholtz-Gemeinschaft

JÜLICH
Forschungszentrum